

Numerical Modeling of Flow in Karst Reservoirs

BY

Md Sarim Jamal

A Dissertation Presented to the
DEANSHIP OF GRADUATE STUDIES

KING FAHD UNIVERSITY OF PETROLEUM & MINERALS

DHAHRAN, SAUDI ARABIA

In Partial Fulfillment of the
Requirements for the Degree of

DOCTOR OF PHILOSOPHY

In

PETROLEUM ENGINEERING

April, 2018

KING FAHD UNIVERSITY OF PETROLEUM & MINERALS
DHAHRAN- 31261, SAUDI ARABIA
DEANSHIP OF GRADUATE STUDIES

This thesis, written by **Md Sarim Jamal** under the direction his thesis advisor and approved by his thesis committee, has been presented and accepted by the Dean of Graduate Studies, in partial fulfillment of the requirements for the degree of **DOCTOR OF PHILOSOPHY IN PETROLEUM ENGINEERING**



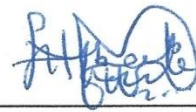
Dr. Dhafer A. Al Shehri
Department Chairman



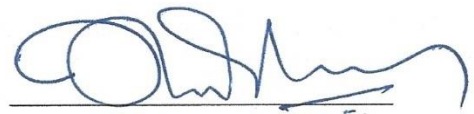
Dr. Salam A. Zummo
Dean of Graduate Studies



8/8/12
Date



Dr. Abee A. Awotunde
(Advisor)



Dr. Abdulazeez Abdulraheem
(Member)



Dr. Hasan Y. Al-Yousef
(Member)



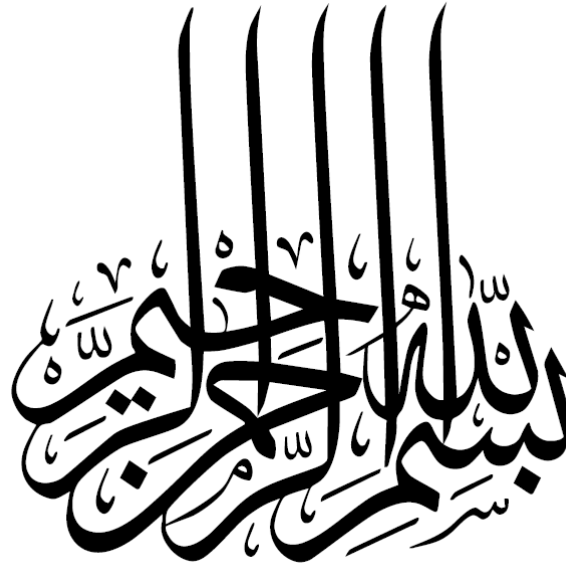
Dr. Mayez A. Al-Mouhamed
(Member)



Dr. Faisal A. Fairag
(Member)

© Md Sarim Jamal

2018



Dedicated to,

My parents, without their love, prayers and sacrifices none of this would have been possible

ACKNOWLEDGMENTS

“In the name of Allah, the most Beneficent, the most Merciful”

First and foremost, all praise is to the Almighty Allah (S.W.T.), the Greatest and the Majestic one. I would like to thank the Almighty Allah (S.W.T.) for bestowing me with His mercy and blessings, and for providing me the opportunity to complete my Ph.D. at King Fahd University of Petroleum and Minerals, Dhahran, and for providing me with the strength and determination to carry out my research ethically and to completion.

I would like to extend my gratitude to King Fahd University of Petroleum & Minerals and the Petroleum Engineering Department, College of Petroleum Engineering & Geosciences, for providing me with financial support, high-level education, first-class equipment, and resources required to carry out a Ph.D. research

Due thanks is owed to my thesis advisor Dr. Abee A. Awotunde for his motivation, and support throughout the course of my Ph.D. at KFUPM. I am extremely grateful for his invaluable guidance and suggestions, without which, this research work would not have been possible. Dr Abee is not only a great academic advisor but also an excellent life coach. I would also like to thank my thesis committee Dr. Abdulazeez Abdulraheem, Dr. Hasan Y. Al-Yousef, Dr. Mayez A. Al-Mouhamed, and Dr. Faisal A. Fairag for their guidance. My great thanks to the Chairman of the Department of Petroleum Engineering, Dr. Dhafer A. Al-Shehri, for his support. I would also like to thank Dr. Abdullah Sultan, for his constant guidance and support during my research.

I would like to thank my research partner AbdAllah Youssef for the time he spent on discussing and resolving the issues we faced initially in our research. I would also like to

acknowledge all the Petroleum Engineering faculty members with whom I took courses during the Ph.D. program.

I am very grateful to Binash Ahmad, Rizwan Khan and Abdul Qadeer for their constant moral support and encouragement during my research work. I would also like to thank Mr. Najmudeen Sibaweih, for his excellent suggestions and his constant support with different softwares I used for my research and otherwise. I would love to thank all my friends, classmates and university mates that I interacted with during my Ph.D. program.

My immense gratitude goes to my beloved parents (Dr. Md. Anwar Jamal & Dr. Shabana Parveen Mallick), my brother (Md. Asim Jamal), my fiancée (Shazia Pervez), and the rest of my family, all of whom have been a great inspiration and source of comfort for me. I thank them from the bottom of my heart for all their love, support and prayers.

Finally, I would like to thank all the people who have directly or indirectly supported me in my research work.

Md Sarim Jamal

TABLE OF CONTENTS

ACKNOWLEDGMENTS	vi
TABLE OF CONTENTS	viii
LIST OF TABLES	xii
LIST OF FIGURES	xiii
LIST OF ABBREVIATIONS	xvi
ABSTRACT	xvii
ABSTRACT (ARABIC)	xix
CHAPTER 1 Introduction	1
CHAPTER 2 Literature Review	5
2.1 Karst Reservoirs	5
2.1.1 Introduction	5
2.1.2 Karstification Process	5
2.1.3 Karst Porosity	7
2.1.4 Karst Caves	8
2.2 Mathematical Models for Fluid Flow	9
2.2.1 Navier-Stokes Equation	10
2.2.2 Darcy's Equation	12
2.3 Mathematical Model for Flow in Coupled Systems	13
2.3.1 Multiple Continuum Method	14
2.3.2 Discontinuum Model or Darcy-Stokes Model	18
2.3.3 Brinkman Equation	21
2.4 Mathematical Solution to Brinkman's Equation	26

CHAPTER 3 Problem Statement	28
3.1 Research Gap	28
3.2 Research Objectives	29
CHAPTER 4 A Finite Volume Discretization Approach to Solving Flow and Tracer Transport in Karst Reservoirs	30
4.1 Introduction	30
4.2 Mathematical Models for Flow	32
4.2.1 Mathematical Equations for Flow	32
4.2.2 Discretization of Equations of Flow	32
4.3 Mathematical Model for Tracer Transport.....	34
4.3.1 Mathematical Equations for Tracer Transport	34
4.3.2 Discretization of the Advection-Diffusion-Adsorption Equation.....	36
4.4 Example Applications, Results and Discussions	37
4.4.1 Example 1	38
4.4.2 Example 2	44
4.5 Conclusion.....	51
CHAPTER 5 Unsteady Brinkman’s Model for Flow in Karst Reservoirs	52
5.1 Introduction	52
5.2 Mathematical Model for Flow	53
5.2.1 Mathematical Equations for Unsteady Flow	54
5.2.2 Discretization of Equations of Flow	56
5.3 Mathematical Model for Tracer Transport.....	59
5.4 Example Applications, Results and Discussions	59
5.4.1 Example 1	59
5.4.2 Example 2	67
5.5 Conclusions	76

CHAPTER 6 Full Field To Sector Modelling for Efficient Simulation in Karst Reservoirs	77
6.1 Introduction	77
6.2 Mathematical Models for Flow	78
6.2.1 The Brinkman’s Model	79
6.2.2 The Darcy’s Model	79
6.2.3 Discretization of the Darcy’s Model.....	80
6.3 Mathematical Models for Tracer Transport	81
6.4 Sector Modeling Approach	81
6.5 Example Applications, Results and Discussions	84
6.5.1 Example 1	84
6.5.2 Example 2	95
6.6 Conclusion	101
CHAPTER 7 Darcy Model with Optimized Permeability Distribution (DMOPD) Technique for Efficient Simulation in Karst Reservoirs	102
7.1 Introduction	102
7.2 Optimization Strategy	104
7.2.1 Differential Evolution (DE).....	104
7.3 The Darcy Model with Optimized Permeability Distribution (DMOPD) Approach	106
7.4 Example Application, Results and Discussions	110
7.4.1 Example 1	110
7.4.2 Example 2	123
7.4.3 Example 3	130
7.5 Conclusion	137
CHAPTER 8 Modelling of Two Phase Flow in Karst Reservoirs	139
8.1 Introduction	139
8.2 Mathematical Models for Flow in Caves and Porous Media	141
8.2.1 Mathematical Equations for Two Phase Flow in Caves	141

8.2.2 Mathematical Equations for Two Phase Flow in Porous Media	144
8.3 Modified Brinkman’s Model for Two Phase Flow in Karst Reservoirs.....	144
8.4 Numerical Modelling of Two-Phase Flow Using the Darcy Model with Optimized Permeability Distribution (DMOPD) Approach.....	154
8.5 Example Application, Results and Discussions	155
8.6 Conclusion.....	162
CHAPTER 9 Conclusions and Recommendations	163
9.1 Conclusions	163
9.2 Recommendations	165
References.....	166
Vitae.....	166

LIST OF TABLES

Table 1: Aquifer Rock and Fluid Properties	39
Table 2: Comparison of tracer concentration produced using Brinkman's and Darcy's equation at the end of simulation time (T=6000)	50
Table 3: Comparison of problem sizes and simulation runtimes (Example 1).....	93
Table 4: Comparison problem sizes and simulation runtimes in Example 2.....	97
Table 5: Rough estimated permeability ratios and the corresponding permeability values for the 11 zones in Example 1	113
Table 6: Optimized permeability ratios and the corresponding permeability values for the 11 zones in Example 1	118
Table 7: Comparison of the simulation run times (Example 1).....	123
Table 8: Optimized permeability ratios and the corresponding permeability values for the 3 zones in Example 2	126
Table 9: Comparison of the simulation run times (Example 2).....	130
Table 10: Optimized permeability ratios and the corresponding permeability values for the 4 zones in Example 3	134
Table 11: Comparison of the simulation run times for first 500 timesteps (Example 3)	137
Table 12: Optimized permeability ratios and the corresponding permeability values for the 8 zones.....	159

LIST OF FIGURES

Figure 1: Topography of Karst System.....	6
Figure 2: Topography of Karst Systems	6
Figure 3: Karst Reservoirs on Multiple Scale (Popov et. al., 2009)	9
Figure 4: Discretization of Matrix Blocks (a)MINC (b) DPM (Wu & Pruess, 1988).....	15
Figure 5: Visualization of the Continuum conceptualization by Wu et. al., 2006.....	17
Figure 6: Actual velocity profile for coupled flow (Neale & Nader, 1974)	19
Figure 7: Velocity profile with the Beavers & Joseph slip boundary condition.....	20
Figure 8: Velocity Profile when using a) Darcy-Stokes model with BJS boundary condition, and b) Brinkman's Equation (single domain model)	23
Figure 9: Flow Regions in Brinkman's Flow	24
Figure 10: Schematic of the Aquifer used in Example 1. The red portion in the middle is the cave while the blue portions are porous media	39
Figure 11: Concentration maps at different values of Peclet numbers when using a) Brinkman's Equation (left column), and b) Darcy's Equation (right column)	42
Figure 12: Concentration Plots comparing Brinkman's , and Darcy's Equation at different values of Peclet number	43
Figure 13: Concentration maps with and without adsorption effects	43
Figure 14: Schematic of the Aquifer used in Example 2	47
Figure 15: Tracer concentration distribution in the aquifer at different times.....	48
Figure 16: Produced tracer Concentrations at different producers	49
Figure 17: Difference in tracer flow patterns when using Darcy's equation and Brinkman's equation	50
Figure 18: Schematic of the aquifer used in Example 1	60
Figure 19: Concentration maps obtained using a) Steady Brinkman's equation, after 10 days, b) Unsteady Brinkman's equation, after 10 days, c) Steady Brinkman's equation, after 50 days, d) Unsteady Brinkman's equation, after 50 days.....	63
Figure 20: Instantaneous tracer concentration after 10 days at location a) from the inlet, b) from the inlet	64
Figure 21: Instantaneous tracer concentration after 50 days at location a) 0.25L from the inlet, b) 0.5L from the inlet	65
Figure 22: Velocity profiles for a) Steady flow, and b) Unsteady flow at the location 0.25L within the linear aquifer	66
Figure 23: Schematic of the Synthetic Aquifer (Example 2).....	68

Figure 24: Tracer concentration obtained in the aquifer using Unsteady flow Brinkman's equation after a) 12.5 days, b) 25 days, c) 37.5 days, d) 50 days	70
Figure 25: Instantaneous Concentration Profile at Observation Well 1 after a) 12.5 days, b) 25 days, c) 37.5 days, d) 50 days	71
Figure 26: Instantaneous Concentration Profile at Observation Well 2 after a) 12.5 days, b) 25 days, c) 37.5 days, d) 50 days	72
Figure 27: Instantaneous Concentration Profile at Observation Well 3 after a) 12.5 days, b) 25 days, c) 37.5 days, d) 50 days	73
Figure 28: Instantaneous Concentration Profile at Observation Well 4 after a) 12.5 days, b) 25 days, c) 37.5 days, d) 50 days	74
Figure 29: Instantaneous Concentration Profile at Observation Well 5 after a) 12.5 days, b) 25 days, c) 37.5 days, d) 50 days	75
Figure 30: Sector extraction from full-field (a) full-field (b) extracted sectors. Note that the yellow regions indicate the caves	83
Figure 31: Schematic of the aquifer used in Example 1: (a) full-field (b) sector	86
Figure 32: Velocity plots obtained after solving Darcy's equation on the full-field (a) velocity distribution in the x-direction, (b) velocity distribution obtained in the y-direction, and (c) Quiver plot using the velocity distributions in x and y-directions	87
Figure 33: Velocity plots obtained after updating the results obtained from solving the Brinkman's equation on the sector a) velocity distribution in the x- direction, b) velocity distribution obtained in the y-direction, and c) Quiver plot using velocity distribution	88
Figure 34: Concentration maps from different modeling techniques (a) Brinkman's model (b) Darcy's model (c) sector modeling technique	89
Figure 35: Velocity profiles from different modeling techniques	90
Figure 36: Instantaneous contaminant concentrations obtained from the different modeling techniques at (a) Observation Station 1 (b) Observation Station 2	94
Figure 37: The full-field, the wells and the extracted sector (a) full-field showing the wells (b) extracted sector (Example 2)	98
Figure 38: Concentration maps at (a) 12.5 days (b) 25 days (c) 37.5 days (d) 50 days.	99
Figure 39: Instantaneous tracer concentration at different production wells (a)P1, (b)P2, (c)P3, (d)P4, (e)P5 and (f)P6	100
Figure 40: Figure showing the division of caves into different zones and the permeability assignment into those zones (a) full-field model (b) division of caves into different zones (c) magnification of a section of cave in Fig. 40b	109

Figure 41: Schematic of the aquifer used in Example 1: (a) full-field model (b) division of the caves into different zones	112
Figure 42: Concentration maps obtained from the three different models (a) Brinkman’s model (b) Darcy’s model (c) Rough Estimated permeability ratios in the 10 different.....	115
Figure 43: Velocity Profiles obtained using the three different modelling techniques ..	116
Figure 44: Graph showing the minimization of the objective function (Example 1)	118
Figure 45: Velocity Profiles obtained using the three different modelling techniques ..	119
Figure 46: Concentration maps from different modeling techniques (a) Brinkman’s model (b) Darcy’s model (c) DMOPD model	120
Figure 47: Instantaneous contaminant concentrations obtained from the different modeling techniques at (a) Observation Station 1 (b) Observation Station 2	122
Figure 48: Aquifer model used in Example 2.....	125
Figure 49: (a) Figure showing the division of the caves into three different zones (b) magnification of a section of the cave	125
Figure 50: Graph showing the minimization of the objective function (Example 2)	126
Figure 51: (a) Plot of concentration profile at the end of 50 days (b) quiver plot showing the velocity direction and magnitude within the aquifer.....	127
Figure 52: Instantaneous tracer concentration at different production wells (a)P1, (b)P2, (c)P3, (d)P4, (e)P5 and (f)P6	129
Figure 53: Aquifer model used in Example 3.....	131
Figure 54: (a) Figure showing the division of the caves into four different zones (b) magnification of a section of the cave	132
Figure 55: Graph showing the minimization of the objective function (Example 3)	134
Figure 56: (a) Plot of concentration profile at the end of 50 days (b) quiver plot showing the velocity direction and magnitude within the aquifer.....	135
Figure 57: Instantaneous tracer concentration at different production wells after 50 days (a)P1, (b)P2, (c)P3, (d)P4, and (e)P5	136
Figure 58: Reservoir Model Used.....	158
Figure 59: Division of Cave into 8 different zones.....	158
Figure 60: Graph showing the minimization of the objective function	159
Figure 61: Figure Showing the Plot of Water Saturation after a) 20 days, and b) 50 days	160
Figure 62: Plot Showing the Water Saturation a) Observation Station 1, b) Observation Station 2	161

LIST OF ABBREVIATIONS

ASTM	American Society for Testing & Materials
BJS	Beavers, Joseph & Saffman Boundary Condition
DMOPD	Darcy's Model with Optimized Permeability Distribution
DE	Differential Evolution
DPM	Dual Porosity Model
DVFN	Discrete Vug Fracture Network
ECM	Effective Continuum Model
EOR	Enhanced Oil Recovery
IMPES	Implicit Pressure Explicit Saturation
MINC	Multiple Interacting Continua
PDE	Partial Differential Equations

ABSTRACT

Full Name : Md Sarim Jamal

Thesis Title : Numerical Modeling of Flow in Karst Reservoirs

Major Field : Petroleum Engineering

Date of Degree : April, 2018.

Modelling and simulation studies of fractured carbonate reservoirs is a challenging problem in the oil and gas industry. This challenge increases furthermore in Karst reservoirs, due to the presence of geomorphological features such as fractures, vugs, and caves etc. on a micro and macro scale, which introduce complex flow regimes due to introduction of non-Darcy flow in the free flow region. This research deals with modelling flow in karst reservoirs while taking into consideration the heterogeneities introduced, due to macro scale features, such as caves. The motivation to model flow in caves lies in the fact that caves are responsible for large hydrocarbon accumulation and also acts as highly permeable conduits for flow.

In this work we will use the Brinkman's equation to model flow in karst reservoirs. The use of Brinkman's equation is motivated by the fact that it simplifies the numerical modelling by allowing the use of a single equation to model the effect of both free flow and porous regions, thus in effect reducing the error due to improper modelling of the interface between the two regions.

In this research we have attempted to perform simulation studies of flow and tracer transport in karst reservoirs using the Brinkman's equation on a field scale. Comparisons have been made to the Darcy's model and the effect of Peclet number on tracer transport have been studied.

We have also considered the effects of unsteady flow conditions in karst aquifers by assessing the addition of an unsteady flow term to the Brinkman's equation. We solved the coupled mass conservation-transport equations that models unsteady fluid transport in karst aquifers and studied the effects of unsteady flow conditions on tracer transport in two different sample aquifers and compared to the results obtained from the steady flow Brinkman's equation.

The methods available to model flow within karst reservoirs are either computationally expensive (Brinkman's model or Darcy-Stokes model) or provides inaccurate results (Darcy's model). In this research we have developed two different alternative models (Sector Modelling Approach and Darcy Model with Optimized Permeability Distribution (DMOPD) Approach), that provides excellent match with the Brinkman's model but is computationally very cheap.

Finally, we have modified the Brinkman's equation to model two phase flow within karst reservoirs. We have also used the DMOPD approach to simulate two phase flow of oil-water in karst reservoirs.

ملخص الرسالة

الاسم الكامل: مد صارم جمال

عنوان الرسالة: محاكاة تدفق السوائل في خزانات الكارست

التخصص: هندسة البترول

تاريخ الدرجة العلمية: ابريل 2018

إن محاكاة تدفق السوائل في خزانات الحجر الجيري هي مهمة صعبة بالنسبة لمجال النفط و الغاز. تزداد هذه الصعوبات في خزانات الكارست لوجود بعض الظواهر الجولوجية مثل التشققات و الفجوات و الكهوف و التي تكون بأبعاد دقيقه او كبيره و التي تؤدي الي وجود مناطق تدفق حر و بالمجمل تؤدي الي تعقيد طبيعة تدفق السوائل. يتناول هذا البحث محاكاة حركة السوائل في خزانات الكارست التي تحتوي علي ظواهر جولوجية كبيره المقياس مثل الكهوف. ان السبب الرئيسي للبحث في هذا الموضوع هو قابلية الكهوف لتخزين كميات ضخمة من الهيدروكربونات بالاضافة الي انها تسهل حركتها في باطن الارض.

في هذا البحث سوف نستخدم معادلة برينكمان لمحاكاة حركة السوائل. ان الدافع وراء استخدام هذه المعادلة هو انها تقوم بدمج حركة السوائل في كل من النسيج الصخري و مناطق التدفق الحر في معادلة واحدة و بالتالي تقليل الخطء الناتج عن محاكاة السطح المشترك بينهم. في هذا البحث حاولنا إجراء دراسات محاكاة للتدفق ونقل الشوائب في مكامن الكارست باستخدام معادلة برينكمان على نطاق ميداني. تم إجراء مقارنات مع نموذج دارسي وقد تم دراسة تأثير رقم بيكلت على نقل الشوائب.

كما قمنا ايضا بدراسة ظروف التدفق غير المستقر في مكامن الكارست المائية عن طريق اضافة جزء التدفق غير مستقر لمعادلة برينكمان. لقد قمنا بحل معادلات بقاء الكتلة للشوائب في حالة السريان غير المستقر في طبقات المياه الجوفية الكارستية ودرسنا تأثيرات ظروف التدفق غير المستقر على نقل الشوائب في نموذجين مختلفين من طبقات المياه الجوفية ومقارنتها بالنتائج التي تم الحصول عليها من معادلة برنكمان المستقرة.

معظم الطرق المتاحة لمحاكاة ظروف التدفق في خزانات الكارست تتطلب وقت كثير مثل معادلة برينكمان او معادلة دارسي ستوك او انها غير دقيقة مثل معادلة دارسي. في هذه الدراسة قمنا بتطوير نموذجين بديلين (نمذجة القطاعات و نموذج دارسي مع توزيع نفاذية محسنة DMOPD) و كلاهما يعطي نتائج متماثلة الي حد كبير مع نموذج برينكمان ولكن بوقت اقل للحسابات.

في النهاية قمنا بتعديل معادلة برنكمان لكي تكون ملائمة لنمذجة سائلين في خزانات الكارست. لقد قمنا ايضا باستخدام DMOPD لمحاكاة حركة النفط و الماء في خزانات الكارست.

CHAPTER 1

INTRODUCTION

Fractured Carbonate reservoirs are responsible for more than 60% of oil reserves and about 40% of the gas reserves (Schlumberger, 2008). Therefore, it is not surprising to know that a large amount of research is directed towards carbonate reservoirs.

One of the major topographical features in carbonates is the presence of karsts. Typically, Karst reservoirs have a high porosity and permeability and consists of vugs, fractures, caves, karrens, dolines etc. These karsts provide economical gains to the oil operator because they provide storage volume and also act as high permeability conduits for the flow of hydrocarbon. They also affect the EOR processes as they have a direct impact on the movement of the injected fluids (Trice, 2005). Apart from the importance of the Karst features to the oil and gas industry, the Karst aquifers cover 12% of the terrestrial land and provide a source of drinking water to almost a quarter of the world's population (Ford and Williams, 2007; Andreo *et al.*, 2010; Hartmann *et al.*, 2014).

Trice, 2005 has separated karst reservoirs into two types: 1) microkarst, 2) megakarst. Microkarsts are defined as consisting of vugs and fractures having openings so small that they cannot be observed by routine borehole logging tools but can only be observed through core and from nuclear magnetic resonance and borehole imaging tools. Megakarsts on other hand is a term used to define karst reservoirs consisting of large conduits and caves. In this work we will be dealing with the flow modeling of reservoir fluids in reservoirs consisting of caves.

Caves are considered as important features in karst reservoirs because through independent researches of Maoshan & Shifan (2011); Montaron et. al. (2014) and CIPR (2016) we know that most of the hydrocarbon accumulation occurs within these caves and therefore can contribute to more oil recovery. Due to the high permeability and extensive reach of caves they can also act as conduits for tracer and EOR fluid (surfactants, polymers, etc.) injection. Caves can be defined as channels which are greater than 5- 15mm in diameter.

Simulation of fractured karst reservoirs is considered a challenge in the oil and gas industry because of the presence of fractures, vugs and caves which introduce a complexity in the equations by introduction of non-darcy flow equations such as the Navier-Stokes equation for flow in the non-porous free flow region. Popov et. al. (2009) mentioned other difficulties apart from the co-existence of two different flow regions. They are:

- 1) Presence of vugs, caves and fractures can alter the effective permeability of the system
- 2) Lack of knowledge of the exact position of the interface between porous media and vugs/caves
- 3) Modelling the effects of formation damage at the interface between porous media and the free flow region

In this research work we have used the Brinkman's equation to model flow through both the porous and the free flow region. The use of Brinkman's equation is motivated by the fact that it simplifies the numerical modelling by allowing the use of a single equation to model the effect of both free flow and porous regions, thus in effect reducing the error due to improper modelling of the interface between the two regions.

A literature review discussing the features of karst reservoirs and aquifers and the numerical methods available to model flow within such features have been presented in Chapter 2.

Chapter 3, discusses the problem statement and the research objectives of this dissertation.

Chapter 4, presents the use of the Brinkman's model to solve for tracer transport in the Karst reservoir using the cell-centered finite volume method. The results of the Brinkman's model are then compared to the Darcy's model. The effect of Peclet number on tracer transport is also studied.

Chapter 5, studies the effect on tracer transport due to the unsteady flow conditions in an aquifer using the unsteady flow Brinkman's equation. Unsteady flow Brinkman's model was obtained by adding the unsteady flow term present in the Navier-Stokes equation to the Brinkman's equation. The results obtained from the unsteady flow Brinkman's are compared to the results obtained from the steady flow Brinkman's model.

Chapter 6, proposes a sector modelling approach to model fluid and contaminant transport within karst aquifers/reservoirs. The method exploits the fast computation associated with the Darcy's model and the accuracy of modeling flow in the caves associated with the Brinkman's model. Thus, the method runs much faster than the Brinkman's model without compromising the accuracy of results obtained in the caves.

Chapter 7, proposes a Darcy Model with Optimized Permeability Distribution (DMOPD) approach to model fluid transport in karst aquifers. This approach divides the free flowing regions (caves) into different zones and optimizes the permeability ratios in those zones to

mimic the velocity profile obtained using the Brinkman's model. The permeability ratio is the ratio of the permeability in that zone to the maximum permeability in the central zone.

This method provides a good match to the solution obtained using the Brinkman's model.

This method significantly speeds up the simulation run compared to the Brinkman's model.

Chapter 8, presents the mathematical formulation for the modified Brinkman's model to numerically model two-phase flow in karst reservoirs. A cell-centered finite volume discretization of the modified Brinkman's model has also been presented. The chapter also presents a method to solve two phase flow in Karst reservoirs using the Darcy Model with Optimized Permeability Distribution (DMOPD) approach.

Chapter 9, presents a concluding remark.

CHAPTER 2

LITERATURE REVIEW

2.1 Karst Reservoirs

2.1.1 Introduction

Karst represents a topography consisting of complex geological features and specific hydrogeological characteristics which are generally formed in carbonate rock reservoirs and are highly heterogeneous. They are mainly composed of limestone, dolomite, gypsum, halite and conglomerates. Carbonate karsts are highly abundant and its most representative morphological features are karrens, tectonic fractures, dolines, shafts, diagenetic fractures, poljes, caves, vugs, ponors, caverns, estavelles, intermittent springs, lost rivers, stylolite, dry river valleys, intermittently inundated poljes, underground river systems, denuded rocky hills, karst plains and collapses (Milanovic, 2005). Figure 1 and Figure 2 show the general topography of karst systems.

Karst aquifers cover 12% of the terrestrial land and provide a source of drinking water to almost a quarter of the world's population (Ford and Williams, 2007; Andreo et al., 2010; Hartmann et al., 2014).

2.1.2 Karstification Process

Karstification is the geological process which produces the unique morphological features of the karst topography, including caverns and channels, by the chemical and mechanical

action of water which has penetrated into the permeable and soluble rock masses (Jackson, 1997). The karstification process may take millions of years, but small scale caves can form within hundreds to thousands of years.

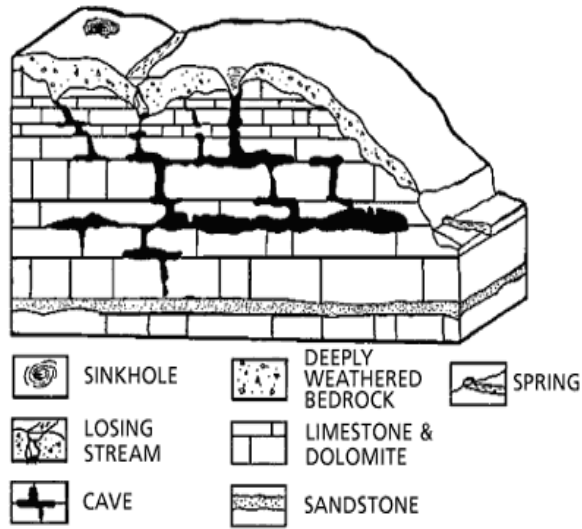


Figure 1: Topography of Karst System

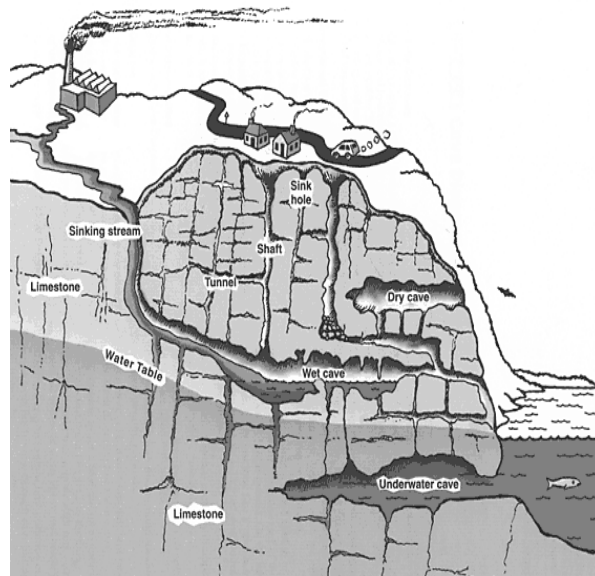


Figure 2: Topography of Karst Systems

Turbulence plays an important role in determining the effectiveness of the karstification process. It has been experimentally shown that the increase in flow velocity and consequently an increase in turbulence increases the dissolution process, a Reynolds number increase from 250 to 25,000 increased the rate of solution by approximately a factor of 3 (White, 1977).

Castany (1966) And Corbel (1959) in their research concluded that temperature is a very important factor and low temperature favoured the karstification process. In the experiments conducted by Castany it was found that 1 litre of water at 0⁰C dissolved 4-5 times more limestone than water at 30⁰C, and 6 times more than water at 40⁰C.

2.1.3 Karst Porosity

Karst porosity can be classified into two main types: Primary porosity and Secondary porosity.

Primary porosity is not very common in karsts and are syngenetic that means it is formed at the time of deposition of sediments.

Secondary porosity are generally more widely present in karsts than the primary porosity and consists of channels, sediments, joints and caverns. Vuggy porosity is a type of secondary porosity and it is due to the presence of vugs; these are voids or larger pores in rocks which are normally associated with karsting and massive dissolution (Lucia, 2007).

Vuggy Porosity can be classified into four main types (Milanovic, 2005):

1. Occasional Vugs: Less than 2% rock volume

2. Scattered Vugs: 2 to 5% of rock volume
3. Vuggy: 5 to 10% rock volume
4. Very vuggy: Greater than 10% rock volume

The presence of these vugs contribute towards higher hydrocarbon storage. These vugs can either be connected to the fracture system or are isolated. Isolated means the vugs that are not connected to the overall fracture system or are not interconnected with other vugs in the matrix rock (Kossack and Gurpinar, 2001).

2.1.4 Karst Caves

In this work the primary interest is to model the flow in caves. Caves can be defined as channels which are greater than 5- 15mm in diameter. The international Speleological Union defines caves as a natural underground opening in rock large enough for a human to enter. Caves contain underground flows that provide natural access to oil and groundwater and act as access ways for exploratory or drilled openings, they can also be used for tracer transport. Most of the hydrocarbon accumulation occur within these karst caves (Maoshan and Shifan, 2011). The largest cave system is 560 km long and is called Mammoth cave system in Kentucky, USA. The deepest is the Krubera Cave in Wester Caucasus, Russia and is 2080m deep.

Norwegian research institution Uni Research CIPR has recently claimed that cave systems are a new type of reservoirs that accommodate significant petroleum resources and are present in Middle East, China, the North Sea and USA (CIPR, 2016).

Figure 3 shows the karst reservoir at different scale. Our work deals with the modelling of flow in karst reservoir on a field scale. Therefore, this work deals with flow through caves and we will neglect the effects of vugs on the much smaller microscale.

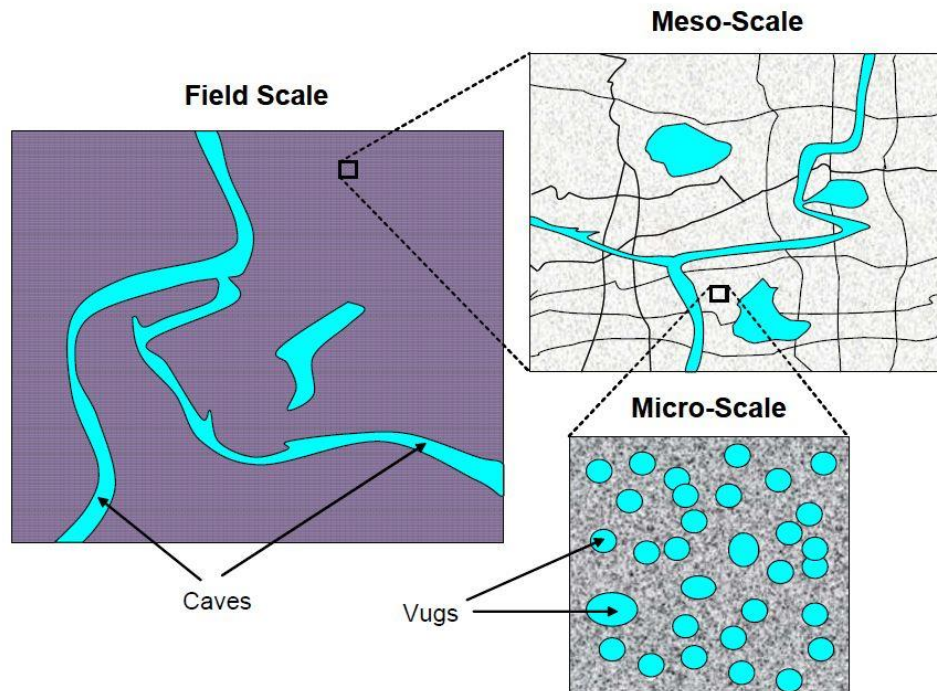


Figure 3: Karst Reservoirs on Multiple Scale (Popov et. al., 2009)

2.2 Mathematical Models for Fluid Flow

It is important to carry out simulation studies of a particular real world physical phenomenon to understand its behaviour properly on a small scale before reproducing it on a larger scale, it becomes more important in fields where actual experiments are very risky, time consuming, may have inaccessible inputs, and maybe economically expensive.

But before the simulation studies can be carried out it is imperative that a mathematical model is developed for that particular physical phenomenon. Mathematical modelling of real world scenarios make it easier to quantify, visualize, simulate and overall easier to understand.

Fluid flow dynamics is an important phenomenon that needs to be studied in the oil and gas industry. It deals with the motion of fluids inside a media. Some of the most important equations are the Hagen-Poiseulle equation, the Bernoulli's equation, the Navier-Stokes Equation and the Darcy's equation. Here we will describe in more detail the latter two as those are the equations we will be dealing with in our work.

2.2.1 Navier-Stokes Equation

Navier-Stokes equation is used to model viscous flow in free flow regions and is named after Claude-Louis Navier (Navier, 1822) and George Gabriel Stokes. It is very widely used to study various different flow problems which carries a research interest for scientists and engineers around the globe. In the oil and gas industry the Navier-Stokes equation is used to model flow in fractures, vugs, caves and pipes.

The Navier-Stokes equation consists of three momentum equation (3D flow) and is used in conjunction with a material balance equation (the continuity equation).

The continuity equation for Navier-Stokes is given by:

$$\frac{\partial \rho}{\partial t} + \nabla \cdot (\rho \vec{v}) = \frac{q_m}{V_b} \quad (2.1)$$

The Navier-Stokes equation itself is given by

$$\rho \frac{d\vec{v}}{dt} + \nabla p - \nabla \cdot \overline{\tau} = \rho g, \quad (2.2)$$

where, ρ is the density of fluid, p is the pressure, $\overline{\tau}$ is the deviatoric stress tensor, g is the acceleration due to gravity, and \vec{v} is the free flow velocity, q_m is the sink/source term in terms of mass flow rate, V_b is the block volume, and t is the time. The deviatoric stress tensor can be given as follows.

$$\overline{\tau} = 2\mu \left[\epsilon - \frac{1}{3}(\nabla \cdot \vec{v})I \right] + \lambda(\nabla \cdot \vec{v})I. \quad (2.3)$$

Where, μ is the viscosity of the fluid and λ is the second coefficient of viscosity. ϵ can be given as follows

$$\epsilon = \frac{1}{2} \left[(\nabla \vec{v}) + (\nabla \vec{v})^T \right]. \quad (2.4)$$

For incompressible flow with constant viscosity, Equation 2.2 can be rewritten as follows,

$$\rho \frac{d\vec{v}}{dt} + \nabla p - \mu \nabla^2 \vec{v} = \rho g. \quad (2.5)$$

Equation 2.5, is a vector equation as all the terms are vectors and therefore we can get three equations from it, so in total we will have to solve a system of four equations to obtain our solution.

If we now assume a steady state flow, i.e. $\frac{d\vec{v}}{dt} = 0$ we will get the Stokes Flow equation.

$$\nabla p - \mu \nabla^2 \vec{v} = \rho g . \quad (2.6)$$

All the above equations and their simplifications can be found in Bird et. al. (2002).

The boundary condition for solving such equations can be Dirichlet type with velocity given at each boundary. No slip condition is generally assumed parallel to the boundary at the boundary, i.e. the velocity is zero (Yao *et al.*, 2010).

2.2.2 Darcy's Equation

Henry Darcy, a French engineer, developed the Darcy's Law (Darcy, 1856), to describe the flow of fluids in porous media. It is one of the most widely used equations in petroleum engineering. Although the equation was developed by conducting experiments but recently it has also been found that the Darcy's equation can be found by the homogenization of the Navier-Stokes equation (Allaire, 1989).

A porous media can be defined as having a solid matrix with interconnected void. Some of the best examples are sandstone, limestone or wood. The porous media is characterized as having a porosity and permeability.

The flow in porous media can be found by using the continuity equation along with equation for Darcy's Law.

The continuity equation can be defined as

$$\frac{\partial(\phi\rho)}{\partial t} + \nabla \cdot (\rho\bar{u}) = \frac{q_m}{V_b}. \quad (2.7)$$

The above equation is similar to equation 2.1, the only difference being the density is now multiplied with the porosity because flow is no longer free flow.

The Darcy's law can be given by the following equation

$$\nabla p + \mu \bar{K}^{-1} \bar{u} = \nabla(\rho g z), \quad (2.8)$$

in the above equations, ρ is the density of fluid, μ is the viscosity of the fluid, p is the pressure, g is the acceleration due to gravity, ϕ is the porosity of the porous media, \bar{K} is the permeability tensor, and \bar{u} is the Darcy flux/velocity.

There are two different methods of solving these systems of equations. Either equation number 2.8 is rearranged and then the value of \bar{u} is substituted in equation 2.7 and then that equation is solved or we can keep both equations 2.7 and 2.8 separate and solve them.

The boundary conditions can be either Dirichlet type, with pressure specified at the boundaries or they can be Neumann type with Darcy flux/velocity specified at the boundaries.

2.3 Mathematical Model for Flow in Coupled Systems

In the previous section we dealt with mathematical models for flow through a single media, i.e. the flow is either in a porous media or through a free flow region. For flow in reservoirs this is not always the case, because a reservoir may consist of fractures, vugs and caves,

especially the carbonate reservoirs. Modelling flow through such heterogeneous reservoirs, with coexisting free flow and Darcy flow, is considered a challenge in the petroleum industry because the modelling equations as shown in the previous section are different for different sections. An added difficulty is the fact that these vugs, caves and fractures have varying size, connectivity and distribution depending on the depositional environment and the diagenetic process involved. These physical properties affect the rate and direction in which the oil moves in the reservoir (Kossack and Gurbinar, 2001). This rate of movement also depends on the type of forces that are acting on the fluids, these forces are the gravity forces, viscous forces and the diffusive forces.

It is not surprising to learn that various different researches are being conducted in this field in order to determine the best method to model flow in coupled systems because fractured karst carbonate reservoirs are located all around the world and is responsible for a large percent of the oil reserves.

In this section we will be discussing some of the major methods used to model coupled Darcy and non-Darcy flows in reservoirs.

2.3.1 Multiple Continuum Method

The Multiple Interacting Continua (MINC) method was first introduced in 1984 by Pruess & Narasimhan. It was based on the dual porosity model (DPM) made famous by Warren & Root (1962) and Odeh (1964). In this method the fractures and the matrix blocks were grouped into two separate but interacting continua. The MINC method also permits the solution for flow of multiphase fluids. It considers a fractured porous reservoir consisting

of three perpendicular sets of infinite, plane parallel fracture of equal spacing and aperture and can work on different dimensions with regular or irregular geometry. Pruess & Narasimhan verified their MINC model with the analytical solution of Warren & Root and found their solution gave a good match. This method discretizes the matrix blocks based on the distance from the fractures and thus creates a sequence of nested volume elements. By using this form of division the transient interaction between matrix and fractures were able to be treated in a more realistic fashion. The difference in discretization of a dual porosity model and an MINC can be seen in Figure 4.

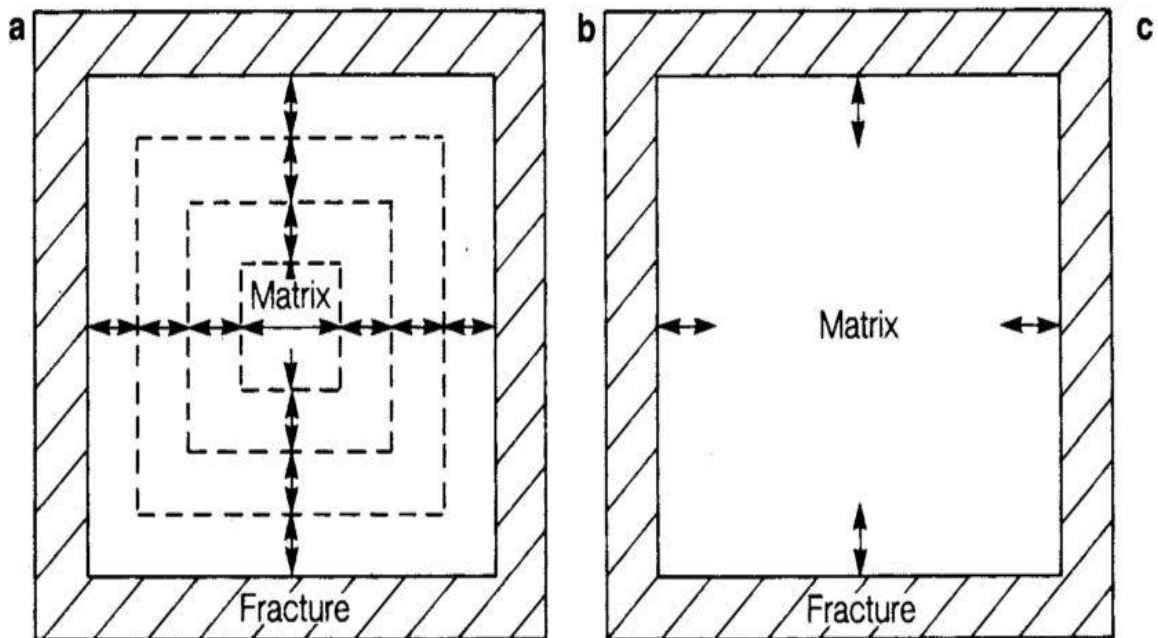


Figure 4: Discretization of Matrix Blocks (a)MINC (b) DPM (Wu & Pruess, 1988)

Wu & Pruess (1988), used the MINC method and demonstrated its utility in different petroleum engineering problems such as modelling oil-recovery problems using water imbibition and five spot water flooding in fractured reservoirs. They compared their results with the dual porosity method and the explicit method and found that the MINC method gave a better match with the actual result. They also concluded that it would be much better to use the dual porosity model for the simpler problems and the use of MINC should only be reserved for the more geologically complex problems.

Bai et. al. (1993), in their paper developed various conceptual deformation-dependent multiporosity and multipermeability models to assist in the simulation of naturally fractured reservoirs. Their work is different from the dual porosity model in such a way that it is not only porosity oriented but also considers permeability as one of the critical factors in affecting flow in reservoirs.

Kossack & Gurpinar (2001), realized that most of the simulators are dual porosity system so they used a dual porosity simulator to emulate oil production from a triple porosity system vugular system. They therefore developed composite relative permeability and capillary pressure curves in a two phase oil-water system, to incorporate the behaviour of vugs in a matrix-fracture system.

An another approach to model fracture/matrix flow is the effective continuum model (ECM), this method has an upper hand in comparison to the MINC method in that it does not require detailed fracture and matrix geometric properties and their spatial distribution. It is therefore computationally effective. This approach uses an effective porous media to approximate the fracture/matrix system. The ECM method assumes thermodynamic

equilibrium and it can be considered as one of the disadvantages of using this method, as the whole method would breakdown if thermal equilibrium is not reached or is not present.

This method has been successfully used by Pruess (1988), Wu (1996), Wu (1999)

Wu et. al. (2006), proposed a multiple-continuum method, which effectively was an expansion on the earlier introduced MINC. They conceptualized the fracture-vug-matrix system to consist of the following 1) fracture continuum 2) vug continuum 3) matrix continuum and 4) small-scale fractures. Figure 5 shows the visualization of the conceptualized continuum.

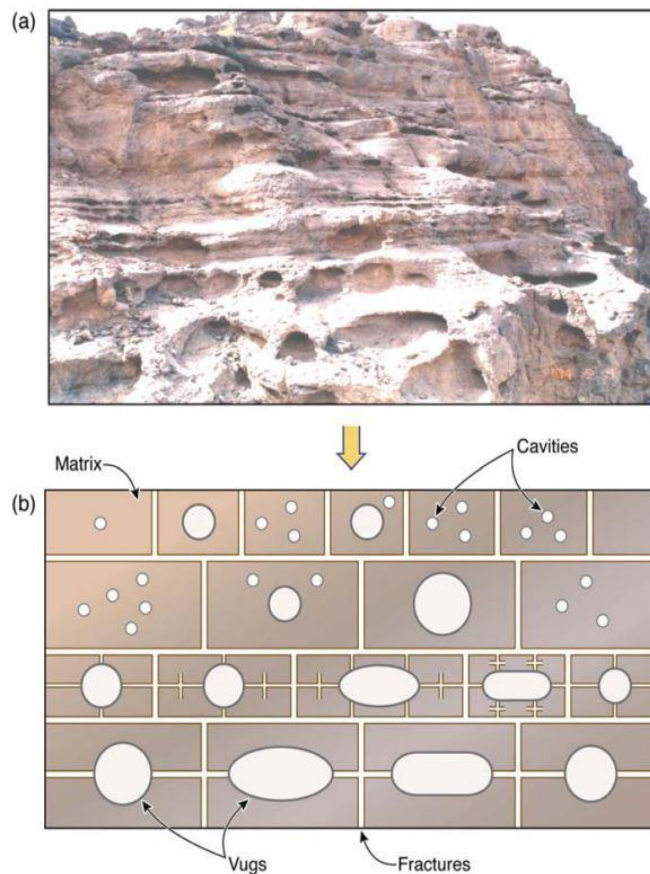


Figure 5: Visualization of the Continuum conceptualization by Wu et. al., 2006

They used an effective porous media approach to approximate the permeabilities and the porosity. They used their model to simulate single phase and multi-phase flow using a finite difference approach.

2.3.2 Discontinuum Model or Darcy-Stokes Model

Although the continuum model was simple and easy, the disadvantage of the method is that it over simplifies a very complex flow pattern consisting of Darcy velocity and free flow velocity into a straightforward mathematical and geometrical model. This may not always give the accurate result. The discontinuum model or Darcy-Stokes model attempts to remove this simplification and provides a more natural approach in representing these systems in which the complex flow patterns exist. This method models Navier-Stokes Equation in the free flow region and the Darcy's equation in the porous region. Appropriate boundary conditions are also used at the interface between the porous region and the free flow region. Various researches have been conducted on the use of Darcy-Stokes model to simulate flow in fractured reservoirs (Arbogast & Lehr, 2006; Arbogast & Brunson, 2007; Arbogast & Gomez, 2009; Peng, Du, Liang, & Qi, 2009).

It has been experimentally proved in different papers (Beavers & Joseph, 1967; Beavers, Sparrow, & Magnuson, 1970), that the effects of viscous shear in the unobstructed channel flow parallel to the surface of a porous media, penetrates the permeable surface to form a boundary layer region in the porous medium. The Darcy equation is not compatible with the existence of a boundary layer region in the porous medium because no macroscopic shear term is associated with this equation (Neale and Nader, 1974). Figure 6 shows the

actual velocity profile for a complex coupled flow in a system consisting of both free channels and porous media.

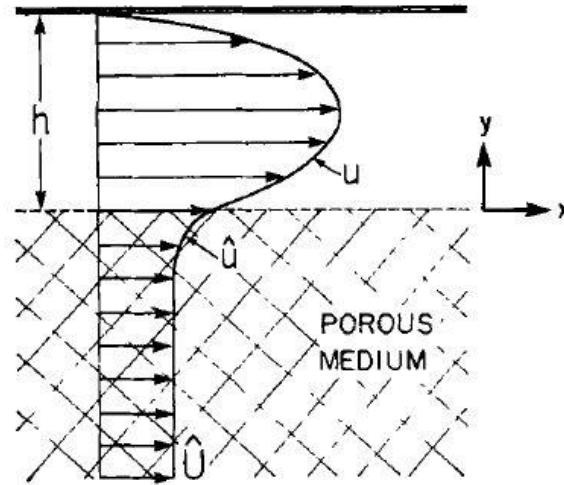


Figure 6: Actual velocity profile for coupled flow (Neale & Nader, 1974)

To model this change in velocity at the boundary, Beavers & Joseph (1967), developed a mathematical equation that introduces a fluid-slip phenomenon at the boundary.

$$v - u = \frac{\sqrt{K}}{\alpha} \frac{\partial v}{\partial y} \quad (2.9)$$

Where v is the free flow velocity; u is the Darcy velocity in the porous media; K is the permeability, and α is the dimensionless slip coefficient. Saffman (1971), justified the use of Equation 2.9 theoretically and even showed that the Darcy's velocity can be dropped altogether from the equation. Jones (1973), then further modified the equation to fit curved boundaries and non-tangential flows.

$$u \cdot \omega = \frac{\sqrt{\omega \cdot K \cdot \omega}}{\mu \alpha} (-\sigma \cdot n) \cdot \omega \quad (2.10)$$

Where ω is the unit tangential vector of boundary.

For Newtonian fluids the boundary conditions are given by

$$2\mu n \cdot \epsilon \cdot n = p_f - p_d \quad (2.11)$$

$$u \cdot \omega = -2 \frac{\sqrt{\omega \cdot K \cdot \omega}}{\mu \alpha} \epsilon \cdot n \cdot \omega \quad (2.12)$$

Equation 2.12 is called the Beavers-Joseph-Saffman (BJS) boundary condition.

Figure 7 shows the velocity profile that would be modelled by using the above mentioned boundary conditions.

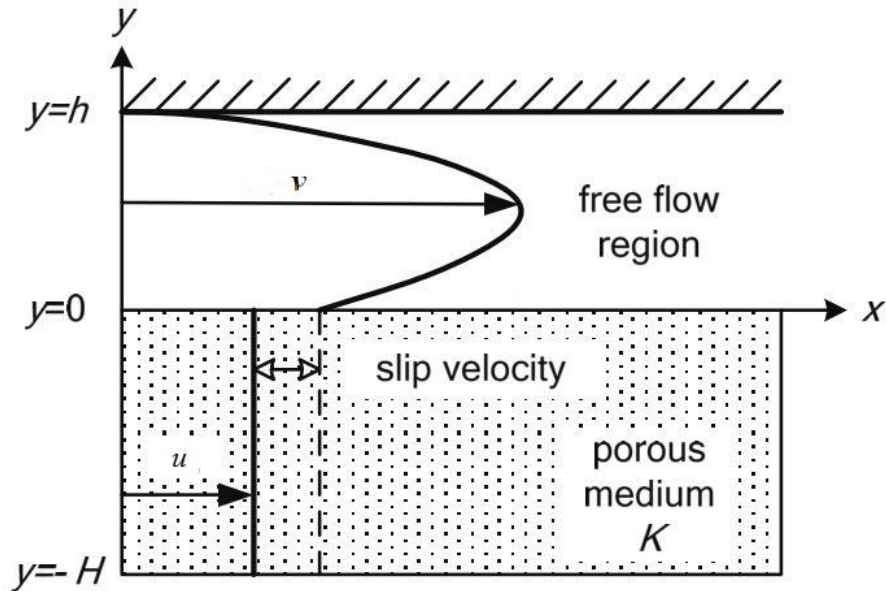


Figure 7: Velocity profile with the Beavers & Joseph slip boundary condition

Zhang et. al. (2004), studied the influence of vugs on flow and transport behavior. To do that they combined simulation studies and performed lab experiments. They used the Darcy equation throughout the pores and vugs, but conceded that the use of Darcy equation in porous media and Stokes in vugs would give much better results.

Vassilev & Yotov (2009), developed a mathematical model using Darcy-Stokes coupled model to solve not just for the velocities but also for chemical transport using a finite element method.

Yao et al. (2010), proposed a discrete fracture vug network (DVFN) model consisting of 1) macro fractures system, 2) porous rock matrix system, 3) macro vug systems. They used the Navier-Stokes equation in the vugular region and Darcy's law within the porous region, and used the BJS boundary condition to model their work.

Huang et al. (2013), calculated the effective permeability tensor of grid blocks using Darcy-Stokes coupling equations and homogenization theory. They then calculated effective relative permeability curves using analytical equations. Finally using the effective permeability and the effective relative permeability curves they used an IMPES simulator to model two phase flow in reservoirs.

2.3.3 Brinkman Equation

Motivated by the complexity of modeling flow in a coupled free flow and porous region, (Brinkman, 1949), developed a general equation that can be used to model the coupled flow. The Brinkman's equation incorporates the effect of viscous shear in the Darcy's

model. The viscous shear is basically the viscous interaction between the molecules among themselves and the media.

$$\nabla p + \mu \overline{\overline{K}}^{-1} \vec{u} - \mu_{eff} \nabla^2 \vec{u} = \rho g . \quad (2.13)$$

Equation 2.13 is called the Brinkman's equation. From the equation p is the pressure, μ is the viscosity, $\overline{\overline{K}}$ is the permeability tensor, \vec{u} is the velocity (darcy or free flow) vector, ρ is the density, g is gravity and μ_{eff} is the effective fluid viscosity. One of the greatest advantages of using the Brinkman's equation is that it can theoretically interpolate between the Stokes equation and the Darcy's equation.

If $\mu_{eff} = \mu$ and $\overline{\overline{K}} = \infty$, Equation 2.13 converts into Stokes equation, it becomes similar to Equation 2.6. Similarly, if $\mu_{eff} = 0$ and $\overline{\overline{K}} = \overline{\overline{K}} (\neq \infty)$, Equation 2.13 now converts into Darcy's equation and becomes similar to Equation 2.8.

Brinkman's equation therefore offers more advantages than directly using the Darcy-Stokes model. Firstly, the requirement of a boundary condition between the porous media and the free flow region disappears. Secondly, the BJS boundary condition models a slip velocity at the boundary which is not actually what happens in reality as can be seen in Figure 6. In actual flow the free flow velocity gradually decreases inside the porous media until it becomes equal to the Darcy velocity. Further inside the porous region the shear term in the Brinkman equation will be unmeasurably small and therefore make the equation equivalent to the Darcy's equation (Neale and Nader, 1974). Figure 8, compares the velocity profiles generated for the Darcy-Stokes model and the Brinkman's model.

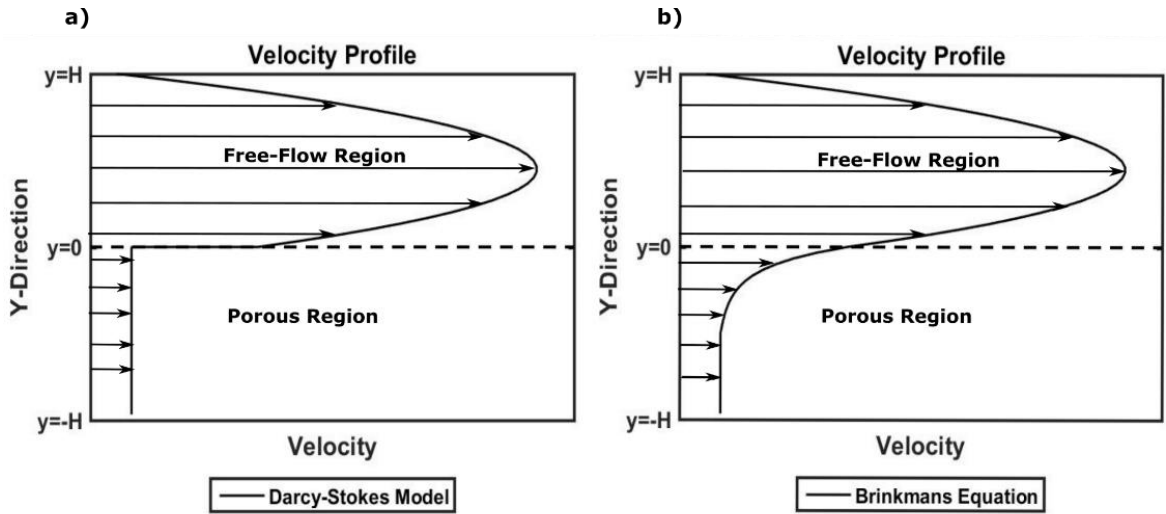


Figure 8: Velocity Profile when using a) Darcy-Stokes model with BJS boundary condition, and b) Brinkman's Equation (single domain model)

According to Durlofsky & Brady (1987), on small length scales the pressure gradient balances the laplacian of velocity and the flow is viscous but deeper in the porous media, the velocity vary very slowly, therefore in this region, the pressure gradient balances the average velocity similarly to Darcy's law.

Different combination of equation can be used to model such complex flows; 1) Navier-Stokes equation can be used in the free flow region and the Brinkman's equation can be used in the porous region, 2) Brinkman's equation can be used throughout the reservoir while keeping $\mu_{eff} = \mu$ and using an arbitrarily chosen high permeability value in the free flow region to mimic infinite permeability, 3) Divide the flow into three regions: free flow region, the Brinkman flow region and the porous flow region, Brinkman's equation can be used in all the three regions but the value set for permeability and μ_{eff} would depend on which region we are modelling.

The values set for the two parameters for different regions will be as follows:

- a) Free flow Region: $\bar{K} = \infty$ or an arbitrarily chosen high value; $\mu_{eff} = \mu$
- b) Brinkman's Flow Region: $\bar{K} = \bar{K} (\neq \infty)$; $\mu_{eff} = \mu$
- c) Darcy Flow Region: $\bar{K} = \bar{K} (\neq \infty)$; $\mu_{eff} = 0$

Figure 9 shows how this division of regions are done. The advantage of dividing into regions is the ease it brings in the computation of results. As has been mentioned before that deeper into the porous media the velocity varies very slowly when compared to the distance we could just neglect the μ_{eff} term and it would decrease the size of the matrix needed to be solved.

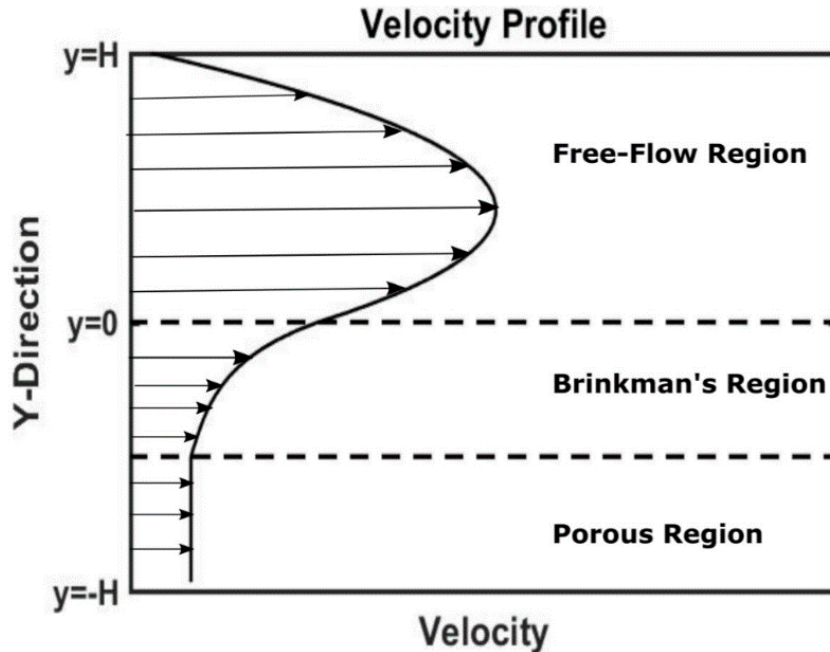


Figure 9: Flow Regions in Brinkman's Flow

Brinkman initially had fixed the μ_{eff} term to be μ , but since then a lot of researches have taken place in finding the optimum value of effective viscosity. Happel & Brenner (1981); Howells (2006), gave justification for using the viscosity value in place of effective viscosity, Adler (1979); Russel & Sangtae (1985), showed that $\frac{\mu}{\mu_{eff}} < 1$; According to the researches of Nield (2013); Koplik, (1983), the value of viscosity ratio is $\frac{\mu}{\mu_{eff}} > 1$. Durlofsky & Brady (1987), showed that the viscosity ratio depends on porosity and behaves in a non-monotonic manner. Belhaj et. al. (2003), in their paper used a value of $\mu_{eff} = \frac{\mu}{\phi}$. Popov et al. (2007), carried out sensitivity studies on different values of effective viscosity. Neale & Nader (1974), provided a practical significance of the use of Brinkman's equation in coupled parallel flows within a channel and a bounding porous media.

Popov et.al. (2007); Popov et al. (2007b); Popov et.al. (2009), successfully carried out various upscaling analysis of distributed caves and vugs and verified that the Brinkman equation can be used to model flows in vuggy, fractured karst reservoirs. Their results also prove that the Brinkman equation allow the simulation of high porosity, finite permeability fill-in regions in fractures and the equation can also be used to model the uncertainty at the interface between fractures and porous media.

Ligaarden et.al. (2010); Krotkiewski et.al. (2011) used the Brinkman' equation to model flow in carbonate Karst reservoirs. In their work they computed the effective permeability of the rock samples. They found that if the free flow region is very large and surrounded

by low permeability matrix the effective permeability can be found by just using the Stokes equation and not considering the Brinkman's equation.

Bi et. al. (2009), proposed the Brinkman's equation as a unified multi-physics model for modeling fluid flow in Karst reservoirs. The model represented flow in rock matrix, void caves and intermediate flows.

He et. al. (2015); He et. al. (2015b) modeled single phase flow in a Karst reservoir using the Brinkman's equation. They solved the proposed equation using the finite difference method, they concluded that the use of a fully implicit finite difference method to solve the Brinkman's equation is straightforward, mathematically simpler and could be easily generalized.

2.4 Mathematical Solution to Brinkman's Equation

The Brinkman's equation for a single phase flow can be solved by using a combination of Equation 2.7 and Equation 2.13.

$$\frac{\partial(\phi\rho)}{\partial t} + \nabla \cdot (\rho\vec{u}) = \frac{q_m}{V_b} \quad (2.7)$$

$$\nabla p + \mu K^{-1} \vec{u} - \mu_{eff} \nabla^2 \vec{u} = \rho g . \quad (2.13)$$

When solving for 3D flow, equation 2.13 will give three equations, one for each dimension; as Equation 2.13 is a vector. For the 3D case there will be 4 unknowns: Pressure (p), u_x , u_y , and u_z . The above equations can be solved using different numerical techniques for solution of PDE such as:

- 1) **Finite Volume Method:** Not a lot of work has been conducted on the use of FVM method to solve for the Brinkman's equation. Hu et. al. (1985) performed a finite volume discretization to solve for the Brinkman's equation for flow of an incompressible fluid on a porous media
- 2) **Finite Element Method:** Almost all the researches that have been conducted employ the finite element method for the solution of Brinkman's equation (Popov et al., 2007; Bi et al., 2009; Gulbransen, Hauge, & Lie, 2009; Popov et al., 2009; Ligaarden et al., 2010; Krotkiewski et al., 2011).
- 3) **Finite Difference Method:** He et al., (2015); He et al. (2015b) used the finite difference technique to solve the Brinkman's equation for a small section of a vuggy karst carbonate reservoirs.

In this work we will be using the Finite volume method to solve the Brinkman's equation.

CHAPTER 3

PROBLEM STATEMENT

3.1 Research Gap

As is clear from the literature review, most of the modelling studies that have been performed on flow in karst reservoirs deals with the calculation of an effective permeability to model flow, not a lot of research have been performed in modelling flow using the Brinkman's equation. The simulation studies that have already been done deals with micro and meso scale vugs and fractures. No proper studies have been done on a field case. This research aims to close this gap by performing simulation studies of flow of fluids using the Brinkman's equation on a field scale and concentrate more on large scale caves.

Most of the equations available to model flow within karst aquifers deal with steady flow conditions. This may not be accurate in aquifers where unsteady conditions exist. To the best of our knowledge no studies have been conducted to model tracer transport in a single-phase, slightly-compressible flow using unsteady Brinkman's equation in karst aquifers/reservoirs.

The methods available to model flow within karst reservoirs are either computationally expensive (Brinkman's model or Darcy-Stokes model) or provides inaccurate results (Darcy's model). There is a need to develop alternative models that provide excellent match with the Brinkman's model but are computationally cheap.

Moreover, to the best of our knowledge, no studies have yet been performed on modelling multiphase flow using the Brinkman's equation. The methods currently available to model

two phase (oil-water) flow in karst reservoirs deal with either the Darcy-Stokes model or the effective porous media approach.

3.2 Research Objectives

The main objectives of this research are

- To use Brinkman's model to simulate flow and tracer transport on a field scale within karst reservoirs and to study the effect of Peclet number on the tracer profile.
- To modify Brinkman's equation to account for unsteady flow conditions existing in the reservoir by addition of a parameter into the Brinkman's model that accounts for the unsteady flow
- To develop new, computationally cheap and accurate models of flow to numerically simulate flow and contaminant transport within karst reservoirs
- To modify the Brinkman's equation to allow the modelling of two phase flow within karst reservoirs
- To develop new, computationally cheap and accurate models of flow to numerically simulate two phase flows (oil-water) within karst reservoirs

CHAPTER 4

A FINITE VOLUME DISCRETIZATION APPROACH TO SOLVING FLOW AND TRACER TRANSPORT IN KARST RESERVOIRS

4.1 Introduction

Tracer tests provide a valuable tool in understanding the flow path of the caves and hence in properly studying the underlying karst (Borghi, Renard and Cornaton, 2016). These tests provide a basis for developing a more realistic and accurate geological model for further testing. Several real-life tracer tests to better understand the karst terrain has been performed all over the world (Cabras et al., 2008; Häuselmann et al., 2003; Smart, 1988; Staut and Auersperger, 2006; White et al., 2013). The physical processes that are responsible for flow of tracers are advection, diffusion and adsorption. Numerical studies have been conducted on modelling transport of chemicals within karst aquifers by using Darcy's equation along with the advection-diffusion equation (Morales-Juberías *et al.*, 1997; Maloszewski, Herrmann and Zuber, 1999; Kincaid, Hazlett and Davies, 2002; Rivard and Delay, 2004; Göppert and Goldscheider, 2007), this however is not very accurate as Darcy's equation does not hold true for free flow regions. Joodi et al., 2010, modelled the transport of Uranine in the Val d'Orleans aquifer in France using the Brinkman's equation in the conduits, and Darcy's equation in the porous region with a continuous pressure boundary condition between the two regions, using Finite Element

Method in COMSOL. They used a very high contrast in the conductivity between the two regions of flow. Oehlmann et al., 2015, used the Manning equation to model flow within the Karst conduits and coupled it with the Advection-Diffusion equations to model tracer transport.

In this section, we model the flow of nonreactive tracers in karst reservoirs by coupling the continuity equation, the Brinkman's equation to the Advection-Diffusion-Adsorption equation. The flow of fluid is modelled as single-phase, slightly-compressible flow in a 2D karst aquifer consisting of megakarstic geological terrains such as caves by solving the continuity equation and the Brinkman's equation simultaneously to obtain the pressure and velocity distribution in the entire reservoir. Using the computed velocity distribution, the Advection-Diffusion-Adsorption equation is then solved numerically to model the transport of the tracers through the reservoir. The cell-centered finite volume discretization approach was adopted in this work in solving the differential equations of flow and tracer transport. The transport of tracer as modelled in this work is then compared with the tracer transport obtained by using Darcy's equation in place of the Brinkman's equation. Two examples are presented to study the transport of tracers and to show the difference in results between using the Brinkman's equation and using the Darcy's equation. The first example consists of a simple linear aquifer model being flooded from one side. The aquifer consists of three regions: two porous regions on each side of a free-flow conduit (cave region). We studied the effect of Peclet number on tracer transport, and the effect it has on the mathematical flow model selection. The second example is a more complex heterogeneous geological structure consisting of more realistic caves with randomly placed water producers and injectors.

4.2 Mathematical Models for Flow

4.2.1 Mathematical Equations for Flow

Brinkman's equation for a single phase flow can be used to model flow by using a combination of Equation 2.7 and Equation 2.13.

$$\frac{\partial(\phi\rho)}{\partial t} + \nabla \cdot (\rho\vec{u}) = \frac{q_m}{V_b} \quad (2.7)$$

$$\nabla p + \mu K^{-1} \vec{u} - \mu_{\text{eff}} \nabla^2 \vec{u} = \rho g . \quad (2.13)$$

The mass flow rate can be rewritten in terms of volumetric flow rate as

$$q_m = \rho q_w \quad (4.1),$$

where, q_w is the volumetric flow rate.

4.2.2 Discretization of Equations of Flow

To discretize the equations, the perturbation is done such that the pressures are at the center of the grid blocks while the velocities are at the grid interfaces.

Equation 2.7 for slightly compressible flow, with volumetric flow rate, can be re-written as (Chen, 2007)

$$\phi\rho c_t \frac{\partial P}{\partial t} + \nabla \cdot (\rho\vec{u}) = \frac{\rho q_w}{V_b} , \quad (4.2)$$

where c_t is the total compressibility of the system. In a slightly compressible flow it is assumed that the pressure has small effects on the porosity of the rock and density of the flowing fluid.

The two-dimensional discretization of Eq. 4.2 is

$$\frac{\rho\phi c_t}{\Delta t} P_{h,i}^{n+1} - \frac{\rho}{\Delta y} u_{y_{h,i-\frac{1}{2}}}^{n+1} + \frac{\rho}{\Delta y} u_{y_{h,i+\frac{1}{2}}}^{n+1} - \frac{\rho}{\Delta x} u_{x_{h-\frac{1}{2},i}}^{n+1} + \frac{\rho}{\Delta x} u_{x_{h+\frac{1}{2},i}}^{n+1} = \frac{\rho q_w}{V_b} + \frac{\rho\phi c_t}{\Delta t} P_{h,i}^n, \quad (4.3)$$

where h and i are the indices of the grid blocks in the x and y-directions, respectively, and n is the index of the time.

The discretization of Eq. 4.3 will give two equations representing the x and y directions.

These equations are

$$\begin{aligned} \frac{1}{\Delta x} P_{h+1,i}^{n+1} - \frac{1}{\Delta x} P_{h,i}^{n+1} - \frac{\mu_{eff}}{\Delta x^2} u_{x_{h+\frac{3}{2},i}}^{n+1} - \frac{\mu_{eff}}{\Delta x^2} u_{x_{h-\frac{1}{2},i}}^{n+1} - \frac{\mu_{eff}}{\Delta y^2} u_{x_{h+\frac{1}{2},i+1}}^{n+1} - \frac{\mu_{eff}}{\Delta y^2} u_{x_{h+\frac{1}{2},i-1}}^{n+1} \\ + \left(\frac{\mu}{K_x} + \frac{2\mu_{eff}}{\Delta x^2} + \frac{2\mu_{eff}}{\Delta y^2} \right) u_{x_{h+\frac{1}{2},i}}^{n+1} = 0 \end{aligned} \quad (4.4)$$

And,

$$\begin{aligned} \frac{1}{\Delta y} P_{h,i+1}^{n+1} - \frac{1}{\Delta y} P_{h,i}^{n+1} - \frac{\mu_{eff}}{\Delta x^2} u_{y_{h+1,i+\frac{1}{2}}}^{n+1} - \frac{\mu_{eff}}{\Delta x^2} u_{y_{h-1,i+\frac{1}{2}}}^{n+1} - \frac{\mu_{eff}}{\Delta y^2} u_{y_{h,i+\frac{3}{2}}}^{n+1} - \frac{\mu_{eff}}{\Delta y^2} u_{y_{h,i-\frac{1}{2}}}^{n+1} \\ + \left(\frac{\mu}{K_y} + \frac{2\mu_{eff}}{\Delta x^2} + \frac{2\mu_{eff}}{\Delta y^2} \right) u_{y_{h,i+\frac{1}{2}}}^{n+1} = 0 \end{aligned} \quad (4.5)$$

4.3 Mathematical Model for Tracer Transport

4.3.1 Mathematical Equations for Tracer Transport

The advection-diffusion-adsorption equation is used to model the flow of tracers within a karst medium. The equation is given by:

$$\nabla \cdot (\phi \overline{D} \cdot \nabla c) - \nabla \cdot (\vec{u}c) + \dot{c}_s = \frac{\partial(\phi c)}{\partial t} + (1 - \phi) \rho_r \frac{\partial c_a}{\partial t}, \quad (4.6)$$

where, \overline{D} , is the dispersion coefficient tensor, c is the concentration of the tracer, \dot{c}_s is the sink/source term of the tracer in terms of specific mass rate, ρ_r is the density of the rock, and c_a is the adsorption of tracer on the surface of the rock (dimensionless).

The dispersion coefficient tensor when the axis is aligned to the velocity directions is given by

$$\overline{D} = \begin{pmatrix} D_x & 0 \\ 0 & D_y \end{pmatrix}$$

where, D_x and D_y , are the principal terms of the diffusion coefficient tensor. We have used the following definitions of the diffusion coefficients (Zhang and Bennett, 2002):

$$D_x = \alpha_L \frac{u_x^2}{|u|} + \alpha_T \frac{u_y^2}{|u|} + D^*, \quad (4.7)$$

And,

$$D_y = \alpha_L \frac{u_y^2}{|u|} + \alpha_T \frac{u_x^2}{|u|} + D^*, \quad (4.8)$$

where, D^* , is the molecular diffusion coefficient, and

$$|u| = \sqrt{u_x^2 + u_y^2}. \quad (4.9)$$

α_L and α_T are the longitudinal and transverse dispersivity. The equations to solve for longitudinal dispersivity are by (Neuman, 1990):

$$\alpha_L = \begin{cases} 0.0175L^{1.46} & L \leq 100 \\ 0.32L^{0.83} & L > 100 \end{cases}, \quad (4.10)$$

where L is the scale of observation.

The transverse dispersivity is fixed at 30% of the longitudinal dispersivity (ASTM, 1994).

The tracer adsorption on the surface of the rock can be described using different isotherms such as Langmuir, Freundlich, and linear. In this study, we have used a linear isotherm (Eq. 4.11) because the tracer concentration levels in most interwell tracer tests are low and linear isotherms can provide a useful model for tracer adsorption effects (Zemel, 1995). The linear isotherm is

$$c_a = K_d c, \quad (4.11)$$

where, K_d , is the adsorption coefficient.

In our work, cesium was used as a tracer because it is considered to be very effective and yields excellent results in carbonate reservoirs (Bjørnstad, Haugen and Hundere, 1994). The value of the adsorption coefficient of cesium on carbonate rocks is 13.5ml/g (Singhal and Gupta, 2010).

4.3.2 Discretization of the Advection-Diffusion-Adsorption Equation

To discretize the equations, the perturbation is done such that the concentrations are at the center of the grid blocks while the velocities are at the grid interfaces.

If we substitute Eq. 4.11 into Eq. 4.6 and assume constant porosity value we obtain

$$\frac{\partial}{\partial x} \left(\phi D_x \frac{\partial c}{\partial x} \right) + \frac{\partial}{\partial y} \left(\phi D_y \frac{\partial c}{\partial y} \right) - \frac{\partial(u_x c)}{\partial x} - \frac{\partial(u_y c)}{\partial y} + \dot{c}_s = \phi \frac{\partial c}{\partial t} + (1 - \phi) \rho_r K_d \frac{\partial c}{\partial t} \quad (4.12)$$

Using the retardation factor, R, given by

$$R = 1 + \frac{1 - \phi}{\phi} \rho_r K_d, \quad (4.13)$$

in Equation 4.12 yields

$$\frac{\partial}{\partial x} \left(\phi D_x \frac{\partial c}{\partial x} \right) + \frac{\partial}{\partial y} \left(\phi D_y \frac{\partial c}{\partial y} \right) - \frac{\partial(u_x c)}{\partial x} - \frac{\partial(u_y c)}{\partial y} + \dot{c}_s = \phi R \frac{\partial c}{\partial t}. \quad (4.14)$$

The discretized form of the advection-diffusion-adsorption equation is

$$\begin{aligned}
& \left(\frac{\phi D_y}{\Delta y^2} \right)_{h,i+\frac{1}{2}}^{n+1} c_{h,i-1}^{n+1} + \left(\frac{\phi D_x}{\Delta x^2} \right)_{h+\frac{1}{2},i}^{n+1} c_{h-1,i}^{n+1} \\
& - \left[\left(\frac{\phi D_x}{\Delta x^2} \right)_{h+\frac{1}{2},i}^{n+1} + \left(\frac{\phi D_x}{\Delta x^2} \right)_{h-\frac{1}{2},i}^{n+1} + \left(\frac{\phi D_y}{\Delta y^2} \right)_{h,i+\frac{1}{2}}^{n+1} + \left(\frac{\phi D_y}{\Delta y^2} \right)_{h,i-\frac{1}{2}}^{n+1} + \frac{\phi_{h,i} R_{h,i}}{\Delta t} \right] c_{h,i}^{n+1} \\
& + \left(\frac{\phi D_x}{\Delta x^2} \right)_{h-\frac{1}{2},i}^{n+1} c_{h+1,i}^{n+1} + \left(\frac{\phi D_y}{\Delta y^2} \right)_{h,i-\frac{1}{2}}^{n+1} c_{h,i+1}^{n+1} \\
& - \frac{u_x^{n+1}}{\Delta x} c_{h+\frac{1}{2},i}^{m+1} + \frac{u_y^{n+1}}{\Delta y} c_{h-\frac{1}{2},i}^{m+1} - \frac{u_y^{n+1}}{\Delta y} c_{h,i+\frac{1}{2}}^{m+1} + \frac{u_y^{n+1}}{\Delta y} c_{h,i-\frac{1}{2}}^{m+1} = - \frac{\phi_{h,i} R_{h,i}}{\Delta t} c_{h,i}^n - \dot{c}_s
\end{aligned} \tag{4.15}$$

In Eq. 4.14 the term, c' , is set using the upwinding technique. Eqs. 4.3, 4.4 and 4.5 are solved implicitly to obtain the values of pressure and velocities in x and y directions; and then using the predicted velocity fields, Eq. 4.15 is then solved to obtain the concentrations of tracers in the grid blocks.

4.4 Example Applications, Results and Discussions

Two examples are presented. The first example uses a simple two-dimensional aquifer model consisting of a free-flow region surrounded in the y-direction by porous regions. The examples are used to study the transport of cesium as simulated under two models. The first model, named Darcy's model in this paper, is that in which the fluid transport in both the free-flow and porous regions is modeled using Darcy's equation. The second model, named the Brinkman's model, is that in which Darcy's equation is used to model the flow in the porous region while Brinkman's equation is used to model the flow in the free-flow region.

4.4.1 Example 1

The first example consists of a two-dimensional karst aquifer model flooded with underground water carrying cesium (the tracer) at a velocity of 0.6 m/day from the left boundary. The aquifer is closed at the top and bottom edges. The aquifer dimension is $240 \times 40 \times 1\text{ m}^3$ and the total number of grids used in the problem is $20 \times 40 \times 1$. In the schematic of the aquifer presented in Figure 10, the region with 100% porosity is the free-flow region (a cave). This region is surrounded by a porous region of porosity 25%. The initial aquifer pressure is 1.38 MPa . The aquifer rock and fluid properties are listed on Table 1. In using the Darcy's model; the permeability of the free-flow region was calculated by using the Poisseuille's equation for flow between parallel plates (Zimmerman and Bodvarsson, 1994)

$$K = \frac{d^2}{12}, \quad (4.16)$$

where d is the width of the conduit. The permeability within the porous region was set to $3.95 \times 10^{-15}\text{ m}^2$. In the Brinkman's model, the permeability of the free-flow region is infinite.

The simulation time was taken as 100 days. In this example, the number of unknowns when solving the fluid flow equation is 2360 while the number of unknowns when solving the advection-diffusion-adsorption equation is 800. The initial concentration of the tracer throughout the aquifer was set to zero.

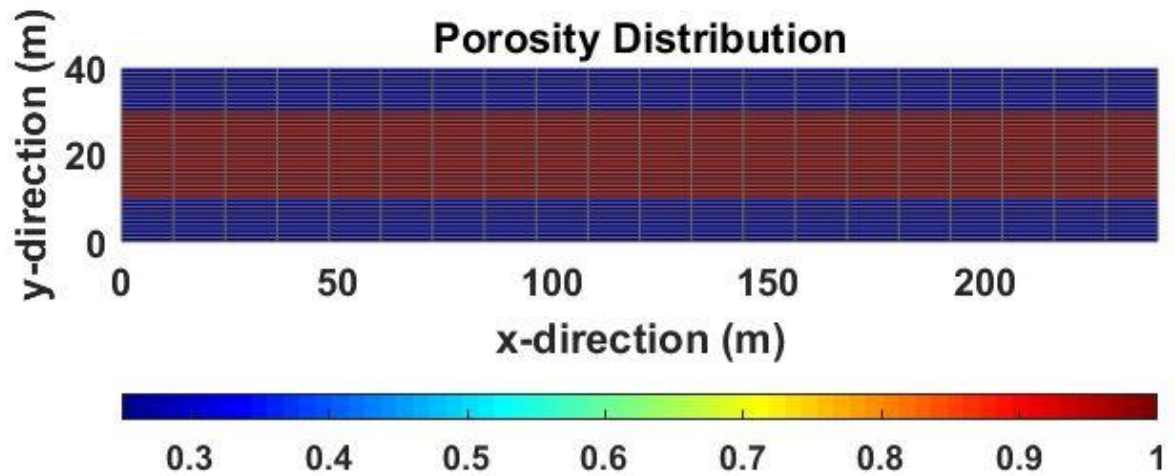


Figure 10: Schematic of the Aquifer used in Example 1. The red portion in the middle is the cave while the blue portions are porous media

Table 1: Aquifer Rock and Fluid Properties

Parameter	Value
Porosity of Porous Region	25%
Porosity of Conduit	100%
Compressibility of the Rock (MPa ⁻¹)	2.2 X 10 ⁻³
Compressibility of Water (MPa ⁻¹)	4.35 X 10 ⁻⁴
Viscosity of Water (MPa-s)	1
Formation Volume Factor of Water	1

We study the effect of Peclet number (Pe) on the flow of tracers within the aquifer. The Peclet number is given by

$$Pe = \frac{uL}{D}, \quad (4.17)$$

where u is the inlet velocity, L is the width of the conduit opening, and D , the dispersion coefficient, found by averaging D_{xx} and D_{yy} . In this example, we set $D_{xx} = D_{yy} = D$ and vary the value of D in order to change the Peclet number associated with the tracer transport. Thus, as the value of D changes, the Peclet number changes. A Peclet number of zero means advection effects are absent and a Peclet number of infinity means diffusion effects are absent. The retardation factor was set to 1, implying the absence of adsorption.

Figure 11 shows two sets of concentration profiles: one set obtained by using Darcy's equation as the transport model in the entire aquifer (porous and free-flow regions); and the other set obtained using Brinkman's equation as the transport model in cave and Darcy's equation as the transport model in the porous region. The concentration profiles are obtained for different Peclet Numbers. It can be seen from the figure that for very high Peclet numbers, the use of Brinkman's equation results in a sharp parabolic profile within the cave whereas the use of Darcy's equation leads to a flattened, piston-like flow profile within the cave. Also, the concentration front in the cave moves faster under the Brinkman's model than under the Darcy's model. However, at low Peclet Number, the speeds of the concentration fronts in the cave remain almost the same under the Darcy and Brinkman's models. Furthermore, we observe that, regardless of the value of Peclet number, the speeds of the concentration fronts in the porous region obtained by using the Brinkman's model

in the cave does not differ appreciably from the speed of the front when the Darcy's equation is used in the cave. As the Peclet number decreases, the effect of diffusion becomes increasingly prominent and the front obtained from the Brinkman's model starts to spread. When the Peclet number dropped below 100, both Brinkman's and Darcy's gave almost similar responses within the aquifer. This observation is further confirmed in Fig. 12. Figure 12 shows the variations of tracer concentration with time at grid block (10,20). The plots of tracer concentration shown on the figure are obtained using the Darcy's equation and Brinkman's equation at Peclet numbers of 10000 (Fig. 12a) and 10 (Fig. 12b), respectively. It is observed that at a higher Peclet number the difference between the concentration obtained from Brinkman's model and that obtained from Darcy's model is large. However, at a lower Peclet number both transport equations give almost similar results. Thus, the observations in this example implies that at lower values of Peclet number, Darcy's equation with very high permeability value can be used within the free-flow region when modelling tracer or contaminant transport. However, at higher Peclet numbers, Darcy's equation underestimates the tracer transport within free-flow regions such as caves.

The effect of adsorption on tracer transport was also studied. Figure 13 shows that the amount of tracer advected reduces when adsorption is present. The effect of adsorption is more prominent in the porous region and near to the walls of the cave than at the center of the cave.

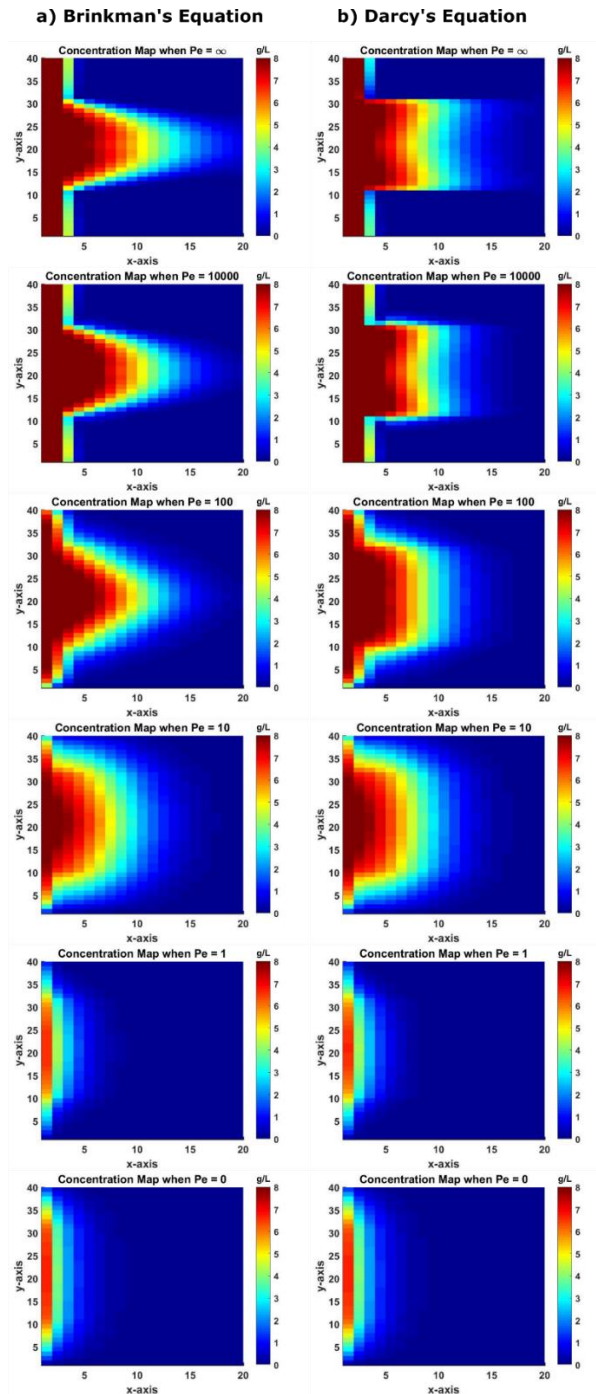


Figure 11: Concentration maps at different values of Peclet numbers when using a) Brinkman's Equation (left column), and b) Darcy's Equation (right column)

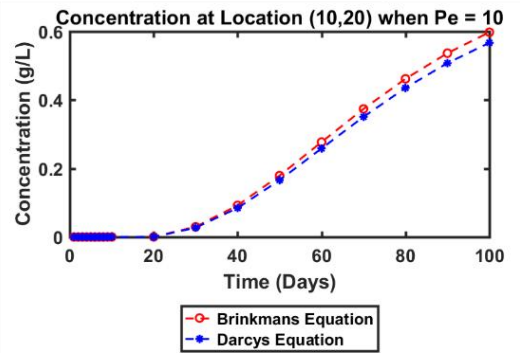
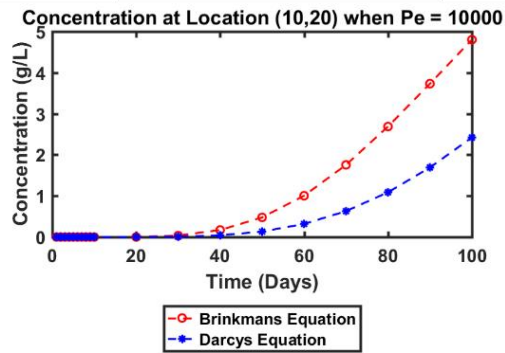


Figure 12: Concentration Plots comparing Brinkman's , and Darcy's Equation at different values of Peclet number

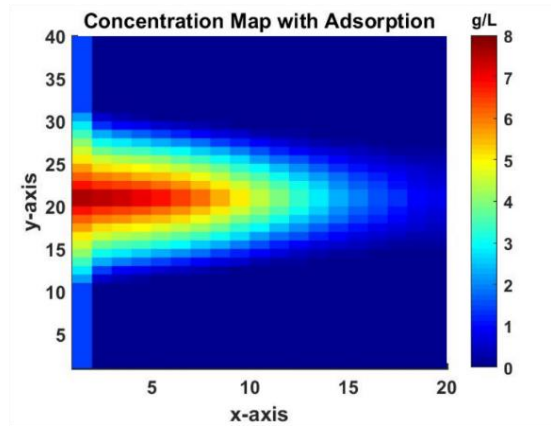
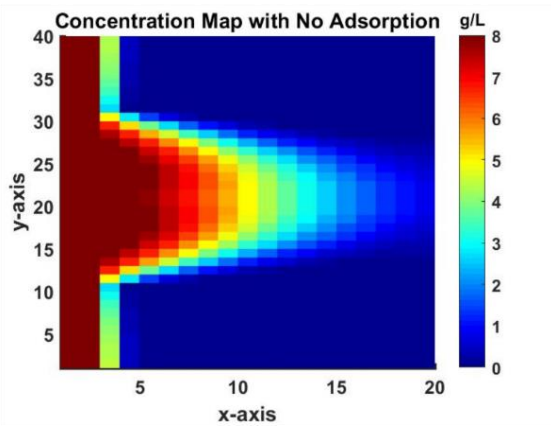


Figure 13: Concentration maps with and without adsorption effects

4.4.2 Example 2

In this example, a more realistic and complex 2D heterogeneous synthetic aquifer (Figure 14) with randomly placed 7 producers and 6 injectors, is used. Four of the seven producers and three of the six injectors are located in the caves, while three producers and three injectors are located in the porous region. The aquifer of size $609.6 \times 609.6 \times 7.62 m^3$ ($2000 \times 2000 \times 25 ft^3$) is located at a depth of 106m. The aquifer is assumed to be closed at all sides and the flow within the aquifer is due to the producers and injectors. The initial pressure of the aquifer is 1.03 MPa. The rock and fluid properties of the aquifer is same as presented in Example 1 on Table 1.

There are three main megakarsts in the aquifer, each with a $9.14m (\approx 30ft)$ wide opening. The hydraulic permeability within the free flow regions is assumed infinite in the Brinkman's model. In the Darcy's model, the permeability of the cave is $33.3m^2$ (as computed from Eq. 4.17). The porous region is heterogeneous and the hydraulic conductivity within this region is log-normally distributed with an average value of $3.95 \times 10^{-15} m^2$.

The simulation time was 6000 days, during which the producers are producing water at a rate of $23.85m^3 / day (\approx 150bbls / day)$ and the injectors are injecting at a rate of $27.82m^3 / day (\approx 175bbls / day)$. Cesium was injected at a concentration of $250g / L$ into the aquifer through the injectors for 2.4 hours after every five years.

The aquifer is meshed into 51,889 unequally sized Cartesian grids, with local refinement to the grids inside the caves and the porous regions adjacent to the caves. Refinement is carried out by breaking each grid in these regions into 2×2 grids. Because of the unequal sizing of the grids, the discretized equations presented are no longer entirely applicable because: 1) some grids are now connected to more than four grid blocks, and the number of grid connections depends on the location being considered; and, 2) the flow fluxes in the regions with grid refinement are no longer perpendicular to the grid faces. Therefore, prior to implementation of the model, the discretized equations were modified to account for these differences. A MATLAB code has been written to perform the refinement and solve the Brinkman's equation along with the advection-diffusion-adsorption equation. The dispersion coefficients were calculated using Eqs. 4.2 and 4.3.

In the Brinkman's model, the number of unknowns in the coupled continuity-transport equation is 156,201 and the number of unknowns in the Advection-Diffusion-Adsorption equation is 51,889.

Figure 15 shows the concentration distribution within the aquifer obtained from the Brinkman's model at different times. We observe that the tracer transport within the free-flow conduits is fast while the transport of the tracers within the porous medium is slow due to poor conductivity and the adsorption of the tracer on the surface of the porous media. Therefore, tracer tests can provide a better understanding of the karst terrain in places where the geology is not yet properly understood.

The simulation of tracer transport was also done using Darcy's model with a high value of permeability in the caves, and the results from this were compared to those from the

Brinkman's model. Comparisons were made using the concentrations of tracer produced at the production wells. Figure 16 shows the tracer concentration profile at the producers. Also, Table 1 shows the concentrations of the tracer at the producers at the end of the simulation run for both models. Producers P1-P4, which are in the caves, produced water with higher concentrations of tracer when Brinkman's model was used than they produced when Darcy's model was used. This is due to the faster moving concentration front in the Brinkman's model relative to the Darcy's model (already discussed in Example 1).

Figure 17 shows the difference in concentration profiles between the two models. Shades of dark red/yellow define areas where the tracer concentrations obtained from Brinkman's model are higher than those from the Darcy's model while the blue spots indicate areas where the tracer concentrations obtained from Darcy's model are higher. Close to injectors I1-I3, located within the caves, the tracer concentration obtained from the Darcy's model is higher because of the slower moving front. In the Brinkman's model, the injected tracer moves much quicker and is transported farther away from these injectors.

Producer, P6, whose main sources of tracer is the injector, I2, gives a higher concentration when the Darcy's equation is used. The reason for this is, when Brinkman's equation is used the injected tracers move much quicker towards the producer, P4, due to a higher drawdown in that direction, whereas when the Darcy's equation is used the tracer front tend to remain behind and move equally around the injector in each direction. Similar flow patterns (Figure 17) can be seen around the injectors I4-I6, which are in the porous region. It is observed that a higher tracer concentration from these wells flow towards the caves when the Brinkman's equation is used because of the higher drawdown towards the caves.

The results obtained from this example conclude that the use of Darcy's equation tends to underestimate the flow velocity and tracer transport further away from the injection source within the conduits. At the same time, it overestimates tracer concentration near the source because of the slower moving front.

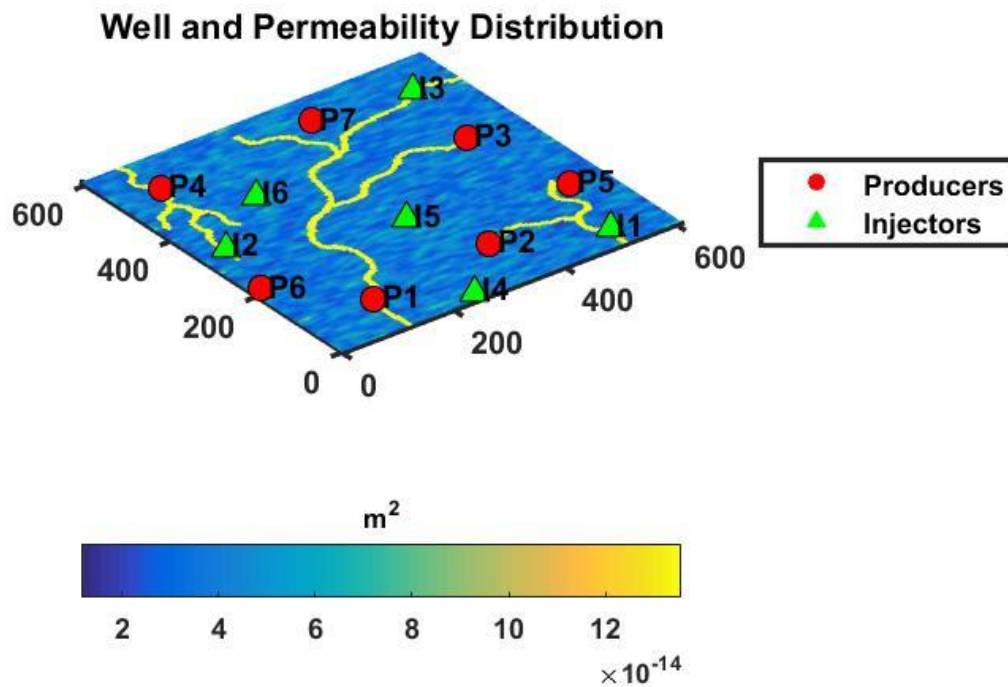


Figure 14: Schematic of the Aquifer used in Example 2

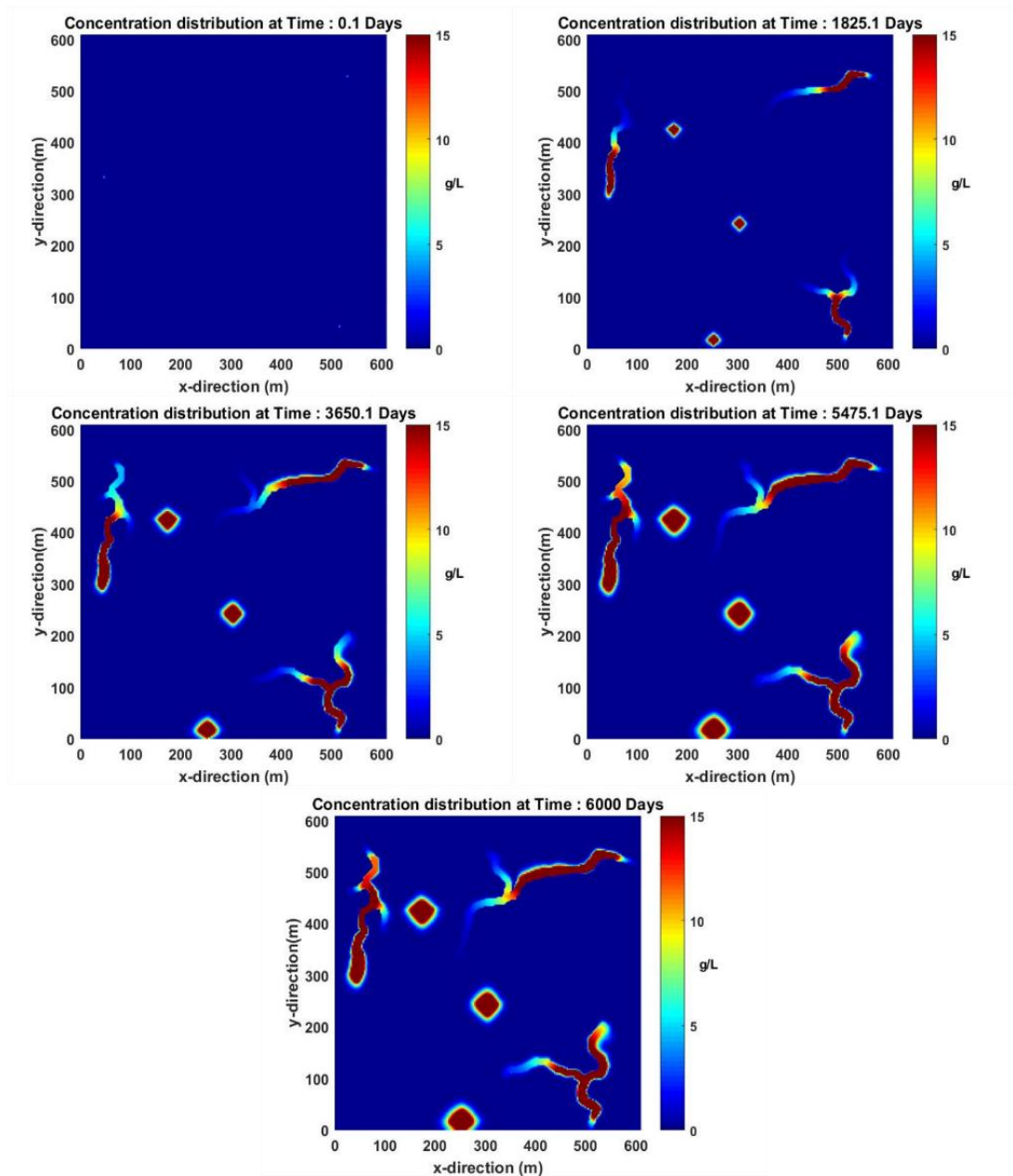


Figure 15: Tracer concentration distribution in the aquifer at different times

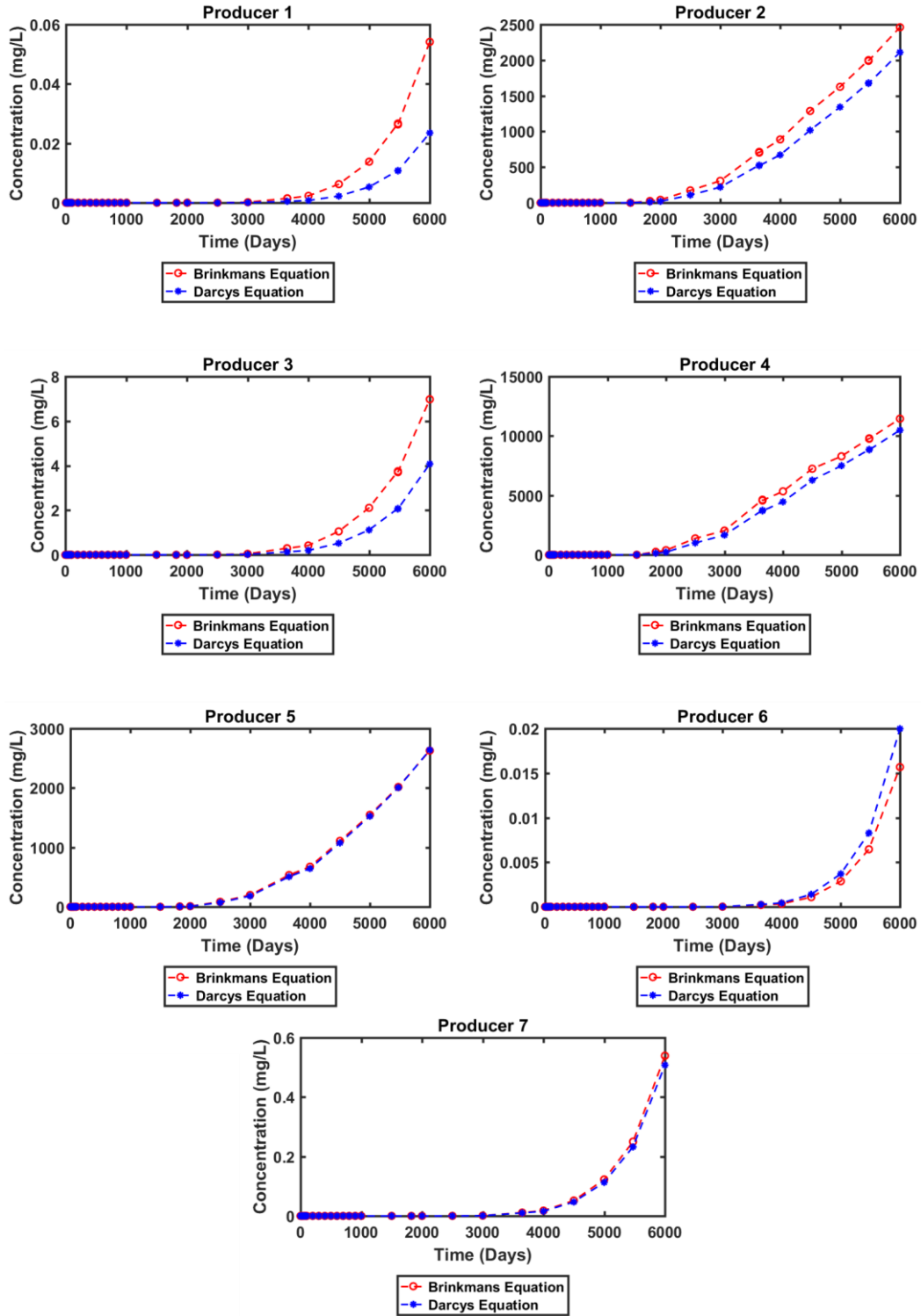


Figure 16: Produced tracer Concentrations at different producers

Table 2: Comparison of Tracer Concentration produced using Brinkman's and Darcy's equation at the end of the simulation time (T=6000 days)

Produced Concentration of Tracer at T = 6000 days (mg/L)		
Producer	Brinkman's Equation	Darcy's Equation
P1	0.054	0.024
P2	2461.680	2109.803
P3	6.978	4.077
P4	11451.633	10487.646
P5	2629.729	2639.202
P6	0.016	0.020
P7	0.539	0.508

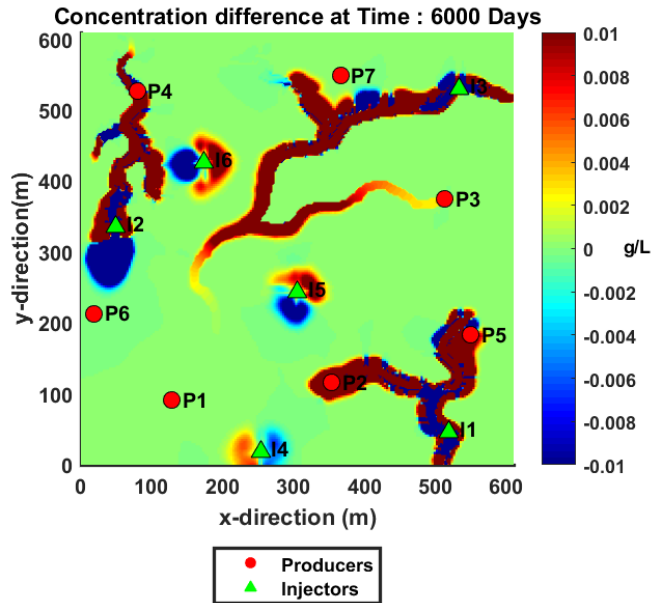


Figure 17: Difference in tracer flow patterns when using Darcy's equation and Brinkman's equation

4.5 Conclusion

We have presented the use of the cell-centered finite volume method to solve the problem of flow in Karst reservoirs. In our work, the Brinkman's equation was used to model flow in the free-flow region while the Darcy's equation was used to model flow in the porous region. We named the combination of these two the Brinkman's model and compared the results from this to the case in which Darcy's equation was used to model the flow in both the free-flow region and the porous region (Darcy model). Using the velocities obtained from these two model, we further solve the advection-diffusion-adsorption equation for tracer transport in the Karst reservoir using the cell-centered finite volume method.

Two example applications were presented. Results from these examples show that the difference between the concentration profiles obtained from Brinkman's model and those obtained from the Darcy's model could be appreciable in some cases. Specifically, Example 1 showed that at high Peclet number, the results obtained from the two models are significantly different while at low Peclet number, the difference between the two models are not significant. Also, in Example 2, faster transport of tracers in the free-flow region was observed in the Brinkman's model than in the Darcy's model.

CHAPTER 5

UNSTEADY BRINKMAN'S MODEL FOR FLOW IN KARST RESERVOIRS

5.1 Introduction

Almost all the models currently being used to model flow through karst reservoirs are steady models. This approach however might not be very accurate in modeling flow during the early times when the unsteady characteristics of the aquifer might dominate the flow profiles. The unsteady characteristics in the flow profile can be introduced because of unsteady pressure gradients which are more apparent at the early stages of flow and decays gradually with time. Unsteady flow can also be observed in cases with changing boundary conditions, such as the change in the aquifer influxes due to increase in rainfall during the monsoon seasons or the subsequent decrease of groundwater flux during periods of drought (Weeks and Sposito, 1998; Zhu *et al.*, 2014). Other reasons that could lead to the introduction of transient unsteady characteristics are recharge events, well pumping, and exposure of coastal settings to oceanic tides (Covington, Wicks and Saar, 2009; Loper and Eltayeb, 2010; Reimann *et al.*, 2011). Unsteady characteristics can also be observed in aquifers where the flow is non-isothermal. The viscous shear term in the Brinkman's equation is impacted because of the changes in viscosity due to temperature changes. Very few studies have been attempted to add the unsteady parameter to model flow within karst aquifers. Some MODFLOW based programs have been developed to couple unsteady

streamflow (Jobson and Harbaugh, 1999; LaBaugh and Rosenberry, 2008; Reimann *et al.*, 2011).

This paper models the flow of nonreactive tracers in karst aquifers consisting of megakarstic geological terrains such as caves, under unsteady flow conditions, by coupling the mass conservation equation, the unsteady Brinkman's equation and the Advection-Diffusion-Adsorption equation. To the best of our knowledge no studies have been conducted to model tracer transport in a single-phase, slightly-compressible flow using unsteady Brinkman's equation in karst aquifers. We solve the coupled differential equations of flow and tracer transport by adopting the cell-centered finite-volume discretization approach. The transport of tracer modelled in this work is then compared with the tracer transport obtained using the steady flow approach. Two examples have been solved to study the effects of unsteady flow term in the Brinkman's equation. The first example is a single linear aquifer model that is flooded with water (carrying a tracer) from one side. The aquifer consists of a free-flow conduit (cave) surrounded by two porous regions. The second example is a complex heterogenous geological structure consisting of more realistic caves.

5.2 Mathematical Model for Flow

This section describes the differential equations governing the flow of a single-phase fluid in a complex karst aquifer and the mathematical formulations used to solve those equations

5.2.1 Mathematical Equations for Unsteady Flow

Brinkman (1949) developed an equation that could model the coupled flow in an aquifer consisting of free-flow and porous regions. The Brinkman's equation given by

$$\nabla p + \mu \overline{\overline{K}}^{-1} \vec{u} - \mu_{eff} \nabla^2 \vec{u} = 0 \quad (2.13)$$

The Brinkman's equation can be modified to add the effects of change in velocity with time and therefore incorporate the unsteady characteristics of flow within the equation. Several studies have been conducted to find an efficient value of the effective viscosity parameter (Adler, 1979; Happel and Brenner, 1981; Koplik, 1983; Russel and Sangtae, 1985; Durlofsky and Brady, 1987; Belhaj *et al.*, 2003; Howells, 2006). However, in this work the value of effective viscosity has been kept as the value of viscosity which was initially suggested by Brinkman in his work. The unsteady Brinkman's equation is given by (Srinivasan and Nakshatrala, 2012; Nield and Bejan, 2013)

$$\rho \frac{d\vec{v}}{dt} + \nabla p + \mu \overline{\overline{K}}^{-1} \vec{u} - \mu_{eff} \nabla^2 \vec{u} = 0. \quad (5.1)$$

In Eq. 5.1, ρ is the density of the flowing fluid, \vec{v} is the intrinsic average velocity and is related to \vec{u} by the Dupuit-Forcheimer relationship ($\vec{u} = \phi \vec{v}$), where ϕ is the porosity (Nield and Bejan, 2013). Eq. 2 can be further expanded as:

$$\rho \left[\frac{\partial \vec{v}}{\partial t} + (\vec{v} \cdot \nabla) \vec{v} \right] + \nabla p + \mu \overline{\overline{K}}^{-1} \vec{u} - \mu_{eff} \nabla^2 \vec{u} = 0. \quad (5.2)$$

In Eq. 5.2, the term $\left(\frac{\partial \vec{v}}{\partial t}\right)$ is known as the local acceleration and it is a result of velocity changes with time at a single point. The second term, $(\vec{v} \cdot \nabla) \vec{v}$, is known as convective acceleration and it occurs due the change in velocity from one point to the other at the same time. Both these terms together take into consideration the change in velocity both in space and time (Hornberger, 2014). On applying the Dupuit-Forcheimer relationship, Eq. 5.2 can be re-written as

$$\rho \left[\frac{1}{\phi} \frac{\partial \vec{u}}{\partial t} + \frac{1}{\phi^2} (\vec{u} \cdot \nabla) \vec{u} \right] + \nabla p + \mu \overline{\overline{K}}^{-1} \vec{u} - \mu_{eff} \nabla^2 \vec{u} = 0. \quad (5.3)$$

The significance of using the unsteady Brinkman's equation is that it can theoretically interpolate between the Navier-Stokes equation and the unsteady Darcy's equation by adjusting the values of $\overline{\overline{K}}$, ϕ and μ_{eff} . When $\mu_{eff} = \mu$, $\overline{\overline{K}} = \infty$, and $\phi = 1$, Eq. 5.3 becomes Navier-Stokes equation (Navier, 1822):

$$\rho \left[\frac{\partial \vec{u}}{\partial t} + (\vec{u} \cdot \nabla) \vec{u} \right] + \nabla p - \mu \nabla^2 \vec{u} = 0, \quad (5.4)$$

which can be used to model flow in the free flow region that includes fractures and caves.

When $\mu_{eff} = 0$, $\overline{\overline{K}} = \overline{\overline{K}}$ ($\neq \infty$), and $\phi < 1$, Eq. 5.3 becomes equivalent to unsteady Darcy's equation which can be used to model flow of fluids in porous media.

$$\rho \left[\frac{1}{\phi} \frac{\partial \vec{u}}{\partial t} + \frac{1}{\phi^2} (\vec{u} \cdot \nabla) \vec{u} \right] + \nabla p + \mu \overline{\overline{K}}^{-1} \vec{u} = 0. \quad (5.5)$$

When $\mu_{eff} = \mu$, $\overline{K} < \infty$, and $\phi < 1$, Eq. 5.3 is used to model the Brinkman's region which starts just at the boundary of the two regions and extends some distance into the porous region until the effect of the viscous shear term becomes negligible. To solve for pressure and velocity of flow of a single-phase fluid, Eq. 5.3 is coupled with the mass conservation equation given by Eq. 2.2.

5.2.2 Discretization of Equations of Flow

While discretizing the equations of flow, the perturbation is done such that the pressures are at the center of the grid blocks while the velocities are at the grid interfaces. The convective acceleration terms in the unsteady Brinkman's equation introduces nonlinearity to the equation. Therefore, the discretized equations are written as residual functions and the Newton-Raphson method for solving nonlinear simultaneous equations is used to solve the problem.

The discretization for the conservation of mass (Eq. 2.2) in two-dimensions is given by

$$R_C^{\gamma+1} = \frac{\phi \rho c_t}{\Delta t} p_{h,i}^{\gamma+1} - \frac{\rho}{\Delta y} u_{y_{h,j-\frac{1}{2}}}^{\gamma+1} + \frac{\rho}{\Delta y} u_{y_{h,i+\frac{1}{2}}}^{\gamma+1} - \frac{\rho}{\Delta x} u_{x_{h-\frac{1}{2},j}}^{\gamma+1} + \frac{\rho}{\Delta x} u_{x_{h+\frac{1}{2},j}}^{\gamma+1} - \frac{\rho q_{sc}}{V_b} - \frac{\phi \rho c_t}{\Delta t} p_{h,i}^n, \quad (5.6)$$

where h and i are the indices of the grid blocks in the x and y -directions, the superscript γ is the iteration index, while the superscript n is the index of time. $R_C^{\gamma+1}$, is the residual function for the conservation of mass.

The Brinkman's equations representing the flow in x and y directions, respectively, are

$$\frac{\rho}{\phi} \frac{\partial u_x}{\partial t} + \frac{\rho}{\phi^2} u_x \frac{\partial u_x}{\partial x} + \frac{\rho}{\phi^2} u_y \frac{\partial u_x}{\partial y} + \frac{\partial p}{\partial x} + \frac{\mu}{K_x} u_y - \mu_{eff} \left(\frac{\partial^2 u_x}{\partial x^2} + \frac{\partial^2 u_x}{\partial y^2} \right) = 0, \quad (5.7)$$

and

$$\frac{\rho}{\phi} \frac{\partial u_y}{\partial t} + \frac{\rho}{\phi^2} u_x \frac{\partial u_y}{\partial x} + \frac{\rho}{\phi^2} u_y \frac{\partial u_y}{\partial y} + \frac{\partial p}{\partial y} + \frac{\mu}{K_y} u_x - \mu_{eff} \left(\frac{\partial^2 u_y}{\partial x^2} + \frac{\partial^2 u_y}{\partial y^2} \right) = 0. \quad (5.8)$$

The discretization of Eq 5.7 will give the following equation

$$\begin{aligned} R_{u_x}^{\gamma+1} = & \frac{\rho}{\phi} \left[\frac{u_{x_{h+\frac{1}{2},j}}^{\gamma+1} - u_{x_{h+\frac{1}{2},j}}^n}{\Delta t} \right] + \frac{\rho}{\phi^2} u_{x_{h+\frac{1}{2},j}}^{\gamma+1} \left[\frac{u_{x_\alpha}^{\gamma+1} - u_{x_\beta}^{\gamma+1}}{\Delta x} \right] + \frac{\rho}{\phi^2} u_{y_{h+\frac{1}{2},j}}^{\gamma+1} \left[\frac{u_{x_\theta}^{\gamma+1} - u_{x_r}^{\gamma+1}}{\Delta y} \right] + \frac{p_{h+1,i}^{\gamma+1} - p_{h,i}^{\gamma+1}}{\Delta x} + \frac{\mu}{K_x} u_{x_{h+\frac{1}{2},j}}^{\gamma+1}, \\ & - \frac{\mu_{eff}}{\Delta x^2} \left[u_{x_{h+\frac{3}{2},j}}^{\gamma+1} - 2u_{x_{h+\frac{1}{2},j}}^{\gamma+1} + u_{x_{h-\frac{1}{2},j}}^{\gamma+1} \right] - \frac{\mu_{eff}}{\Delta y^2} \left[u_{x_{h+\frac{1}{2},j+1}}^{\gamma+1} - 2u_{x_{h+\frac{1}{2},j}}^{\gamma+1} + u_{x_{h+\frac{1}{2},j-1}}^{\gamma+1} \right] = 0 \end{aligned} \quad (5.9)$$

where, $R_{u_x}^{\gamma+1}$, is the residual function for the Brinkman's equation in the x -direction. The

values of $u_{x_\alpha}^{\gamma+1}$, $u_{x_\beta}^{\gamma+1}$, $u_{x_\theta}^{\gamma+1}$, $u_{x_r}^{\gamma+1}$ are evaluated using the upwinding technique

$$u_{x_\alpha}^{\gamma+1} = \begin{cases} u_{x_{h+\frac{1}{2},j}}^{\gamma+1} & \text{if } u_{x_{h+\frac{1}{2},j}}^{\gamma+1} > 0 \\ u_{x_{h+\frac{3}{2},j}}^{\gamma+1} & \text{if } u_{x_{h+\frac{1}{2},j}}^{\gamma+1} < 0 \end{cases}, \quad (5.10)$$

$$u_{x_\beta}^{\gamma+1} = \begin{cases} u_{x_{h-\frac{1}{2},j}}^{\gamma+1} & \text{if } u_{x_{h+\frac{1}{2},j}}^{\gamma+1} > 0 \\ u_{x_{h+\frac{1}{2},j}}^{\gamma+1} & \text{if } u_{x_{h+\frac{1}{2},j}}^{\gamma+1} < 0 \end{cases},$$

And,

$$u_{x_\theta}^{\gamma+1} = \begin{cases} u_{x_{h+\frac{1}{2},j}}^{\gamma+1} & \text{if } u_{y_{h+\frac{1}{2},j}}^{\gamma+1} > 0 \\ u_{x_{h+\frac{1}{2},j+1}}^{\gamma+1} & \text{if } u_{y_{h+\frac{1}{2},j}}^{\gamma+1} < 0 \end{cases}, \quad (5.11)$$

$$u_{x_\tau}^{\gamma+1} = \begin{cases} u_{x_{h+\frac{1}{2},j-1}}^{\gamma+1} & \text{if } u_{y_{h+\frac{1}{2},j}}^{\gamma+1} > 0 \\ u_{x_{h+\frac{1}{2},j}}^{\gamma+1} & \text{if } u_{y_{h+\frac{1}{2},j}}^{\gamma+1} < 0 \end{cases}.$$

The discretization of Eq. 5.9 will give the following equation

$$R_{u_y}^{\gamma+1} = \frac{\rho}{\phi} \left[\frac{u_{y_{h,i+\frac{1}{2}}}^{\gamma+1} - u_{y_{h,i+\frac{1}{2}}}^n}{\Delta t} \right] + \frac{\rho}{\phi^2} u_{x_{h,j+\frac{1}{2}}}^{\gamma+1} \left[\frac{u_{y_\alpha}^{\gamma+1} - u_{y_\beta}^{\gamma+1}}{\Delta x} \right] + \frac{\rho}{\phi^2} u_{y_{h,j+\frac{1}{2}}}^{\gamma+1} \left[\frac{u_{y_\theta}^{\gamma+1} - u_{y_\tau}^{\gamma+1}}{\Delta y} \right] + \frac{p_{h,i+1}^{\gamma+1} - p_{h,i}^{\gamma+1}}{\Delta x} + \frac{\mu}{K_y} u_{y_{h,i+\frac{1}{2}}}^{\gamma+1}, \quad (5.12)$$

$$- \frac{\mu_{eff}}{\Delta x^2} \left[u_{y_{h+1,j+\frac{1}{2}}}^{\gamma+1} - 2u_{y_{h,j+\frac{1}{2}}}^{\gamma+1} + u_{y_{h-1,j+\frac{1}{2}}}^{\gamma+1} \right] - \frac{\mu_{eff}}{\Delta y^2} \left[u_{y_{h,j+\frac{3}{2}}}^{\gamma+1} - 2u_{y_{h,j+\frac{1}{2}}}^{\gamma+1} + u_{y_{h,j-\frac{1}{2}}}^{\gamma+1} \right] = 0$$

where $R_{u_y}^{\gamma+1}$ is the residual function for the Brinkman's equation in the y-direction. The

values of $u_{y_\alpha}^{\gamma+1}$, $u_{y_\beta}^{\gamma+1}$, $u_{y_\theta}^{\gamma+1}$, $u_{y_\tau}^{\gamma+1}$ is evaluated using the upwinding technique

$$u_{y_\alpha}^{\gamma+1} = \begin{cases} u_{y_{h,j+\frac{1}{2}}}^{\gamma+1} & \text{if } u_{x_{h,j+\frac{1}{2}}}^{\gamma+1} > 0 \\ u_{y_{h+1,j+\frac{1}{2}}}^{\gamma+1} & \text{if } u_{x_{h,j+\frac{1}{2}}}^{\gamma+1} < 0 \end{cases}, \quad (5.13)$$

$$u_{y_\beta}^{\gamma+1} = \begin{cases} u_{y_{h-1,j+\frac{1}{2}}}^{\gamma+1} & \text{if } u_{x_{h,j+\frac{1}{2}}}^{\gamma+1} > 0 \\ u_{y_{h,j+\frac{1}{2}}}^{\gamma+1} & \text{if } u_{x_{h,j+\frac{1}{2}}}^{\gamma+1} < 0 \end{cases},$$

and

$$u_{y_\theta}^{\gamma+1} = \begin{cases} u_{y_{h,i+\frac{1}{2}}}^{\gamma+1} & \text{if } u_{y_{h,i+\frac{1}{2}}}^{\gamma+1} > 0 \\ u_{y_{h,i+\frac{3}{2}}}^{\gamma+1} & \text{if } u_{y_{h,i+\frac{1}{2}}}^{\gamma+1} < 0 \end{cases}, \quad (5.14)$$

$$u_{y_\tau}^{\gamma+1} = \begin{cases} u_{y_{h,i-\frac{1}{2}}}^{\gamma+1} & \text{if } u_{y_{h,i-\frac{1}{2}}}^{\gamma+1} > 0 \\ u_{y_{h,i+\frac{1}{2}}}^{\gamma+1} & \text{if } u_{y_{h,i-\frac{1}{2}}}^{\gamma+1} < 0 \end{cases}.$$

5.3 Mathematical Model for Tracer Transport

The mathematical models for tracer transport has already been discussed in detail in Section 4.3 of this manuscript.

5.4 Example Applications, Results and Discussions

Two examples are presented to study the effects of adding the unsteady flow term to the Brinkman's equation. The first example is a simple two-dimensional linear aquifer model consisting of a single conduit (free-flow region) surrounded on both sides in y -direction by porous regions. The second example is a more complicated heterogeneous aquifer consisting of more realistic cave-like structures embedded in a porous media. The transport of a tracer (cesium) is used to quantify the effect of presence of the unsteady flow term in the Brinkman's equation.

5.4.1 Example 1

The first example is a simple two-dimensional linear aquifer model being flooded with underground water carrying a tracer (cesium) at a velocity of 0.6 m/day from the left

boundary. The aquifer length (L) is 1040m , and its width (W) is 40m . In solving this problem numerically, the aquifer was discretized into $40 \times 40 \times 1$ grids, with the thickness kept as 1m throughout the aquifer. The aquifer is closed at the top, right and bottom boundaries. In the aquifer presented in Fig. 18, the region with 100% porosity (red portion in the middle) is the conduit/cave (free-flow region). This region is surrounded by a porous region of porosity 25% (blue portions). The initial aquifer pressure was 1.38MPa . The aquifer rock and fluid properties are listed on Table 1. The numerical simulation was run for 50 days. A time-step of 0.1 day was used for up to one day, and after that a time-step of one day was used till the end of the simulation.

The number of unknowns solved in the coupled continuity-transport equation was 4720 and the number of unknowns in the Advection-Diffusion-Adsorption equation was 1600.

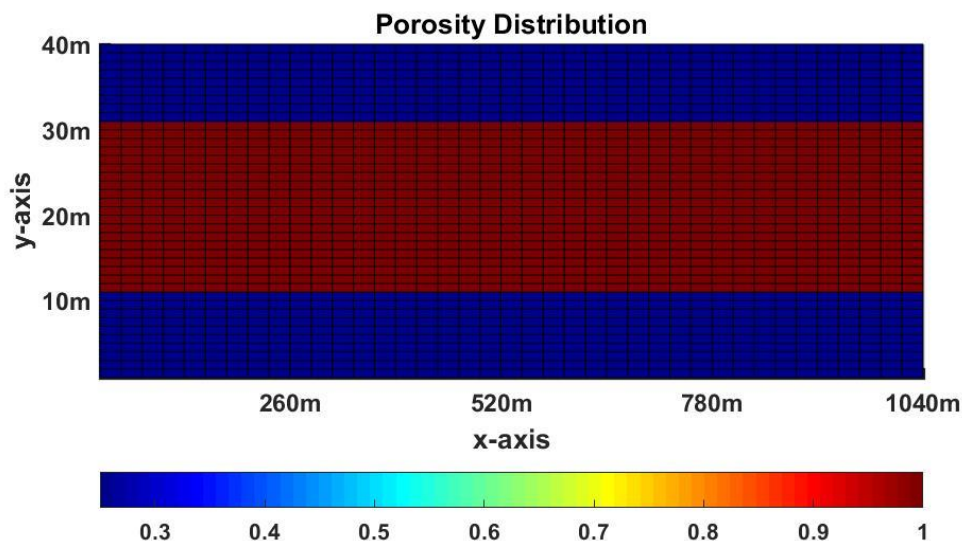


Figure 18: Schematic of the aquifer used in Example 1

Figure 19 shows the comparison of concentration profiles obtained from the steady and unsteady Brinkman's models at different timesteps. The concentration profile obtained from the steady Brinkman's model is more parabolic compared to the profile obtained from the unsteady Brinkman's model. The differences become more apparent in Figs. 20 and 21 where the instantaneous concentration of tracer obtained using both the equations at different locations within the aquifer are presented together. Figure 20 and 21 shows that when the steady flow model was used, the tracer reached the observation stations earlier than when the unsteady flow model was used. This phenomenon can be explained by observing the velocity profiles presented in Fig. 22. This figure shows the plot of velocity profile for both the steady flow and the unsteady flow conditions at a distance one-fourth of the aquifer length (i.e. at 270m from the inlet). The velocity profile from the steady flow Brinkman's model shows an expected parabolic shape in the cave. The velocity profile within the porous media is not evident here because of the very low values of velocity within the porous regions. Although, a steady flow Brinkman's model was used, a change in the velocity is observed initially when the time duration changes from 0.1 day to 1 day (Fig. 22a), this change is observed because of the slightly compressible nature of the fluid being assumed, this assumption initially provides unsteady pressure gradients across the aquifer. After this the velocity profile remains the same from then on until the end of simulation. The velocity profile for the unsteady Brinkman's equation (Fig 22b) does not show an instantaneous parabolic shape, instead at the very early stages the profile is linear. As the time proceeds the velocity profile gradually develops into a more parabolic shape, the gradual development in velocity profile leads to delay in tracer transport when compared to the steady flow. As the velocity profile within the caves develop, the

instantaneous tracer concentration at the desired locations start converging for both the equations, with the convergence quicker at $0.25L$ when compared to the location $0.5L$, because of it being closer to the source, and there being no other disturbance in the aquifer. This gradual change in the profile shape for the unsteady flow is due to the interaction of pressure gradient with viscosity. As time proceeds, the viscous forces slow the flow near the wall whereas the pressure gradient accelerates the flow uniformly in the free-flowing region (Zhu *et al.*, 2014).

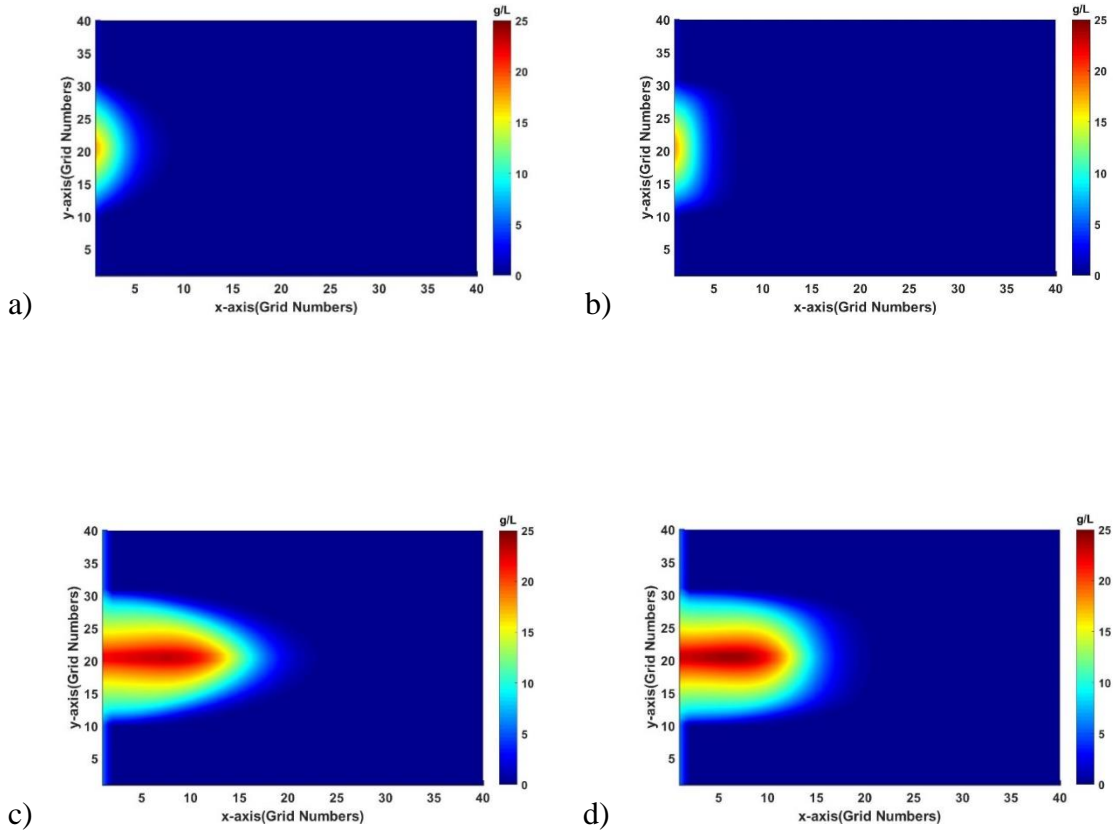
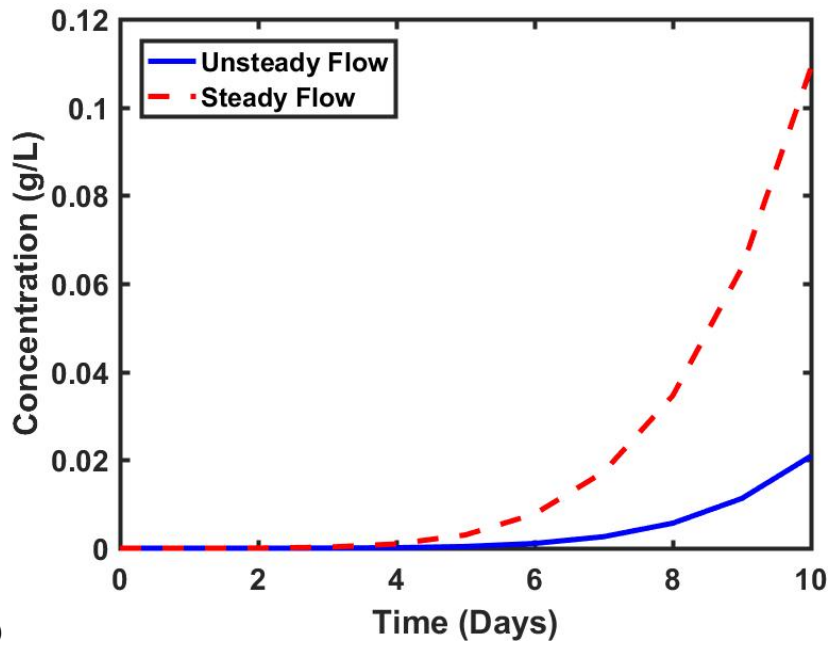
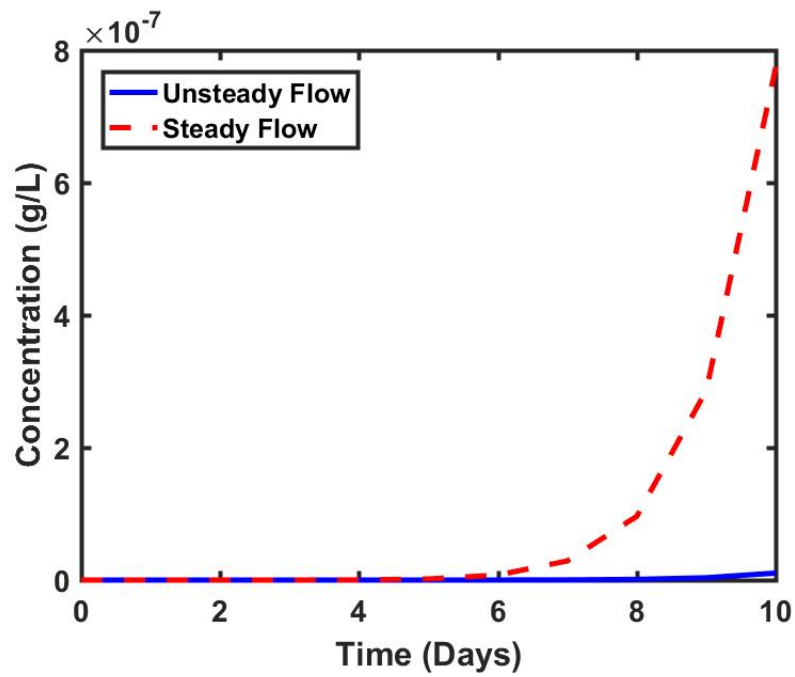


Figure 19: Concentration maps obtained using a) Steady Brinkman's equation, after 10 days, b) Unsteady Brinkman's equation, after 10 days, c) Steady Brinkman's equation, after 50 days, d) Unsteady Brinkman's equation, after 50 days

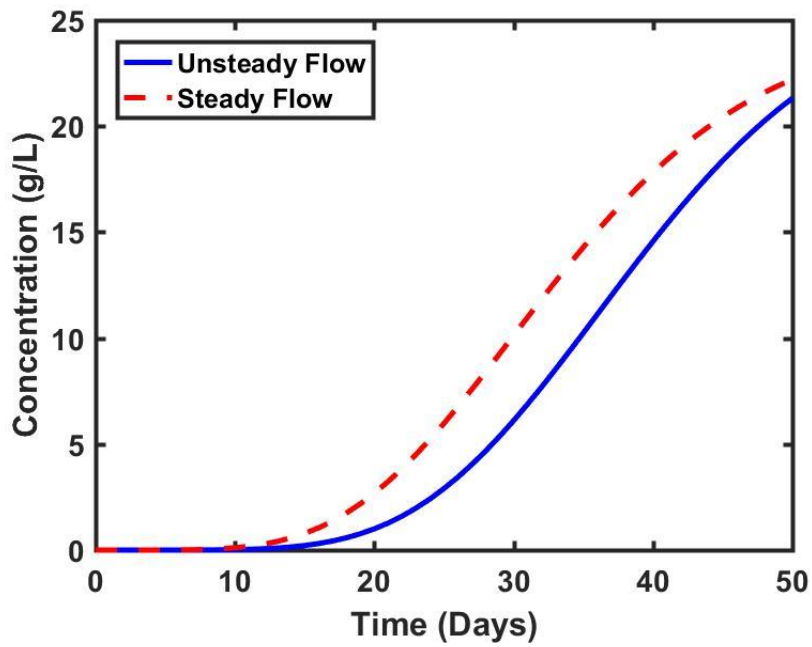


a)

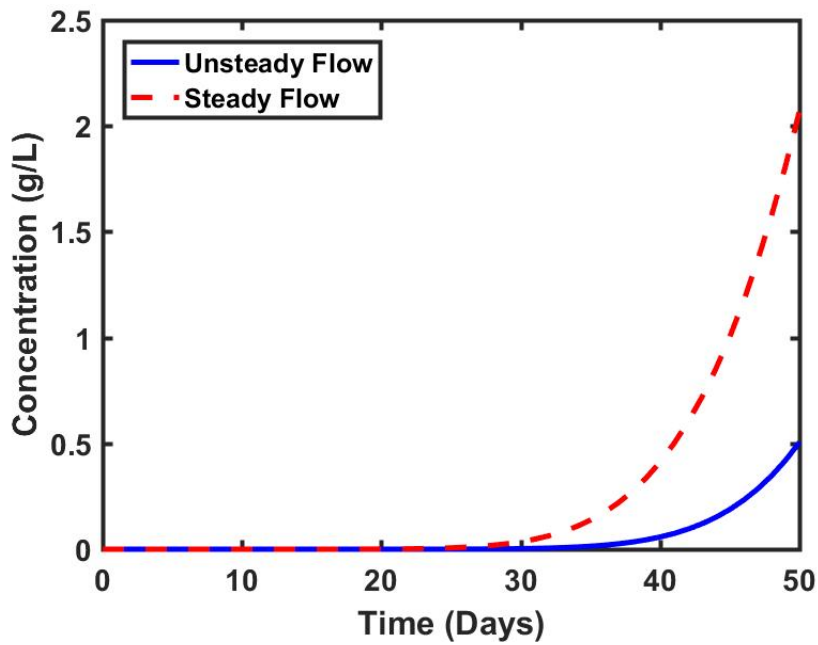


b)

Figure 20: Instantaneous tracer concentration after 10 days at location a) from the inlet, b) from the inlet

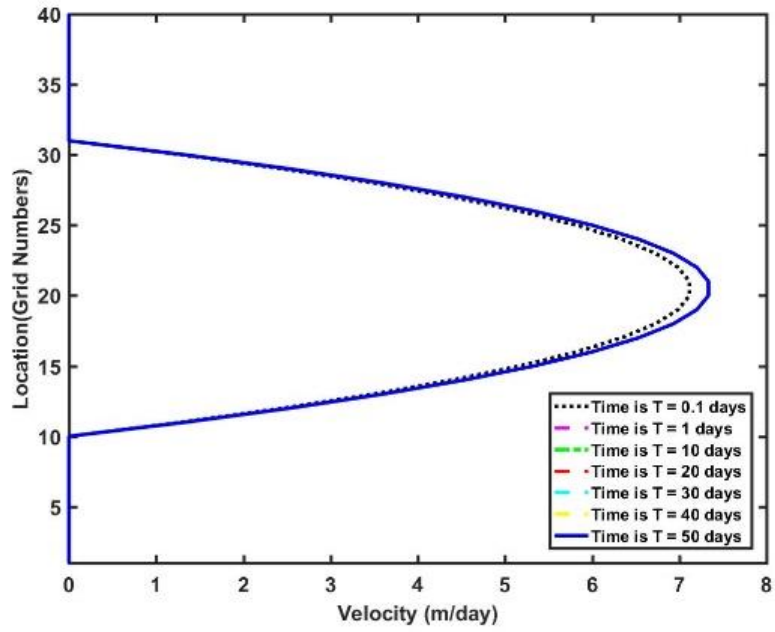


a)

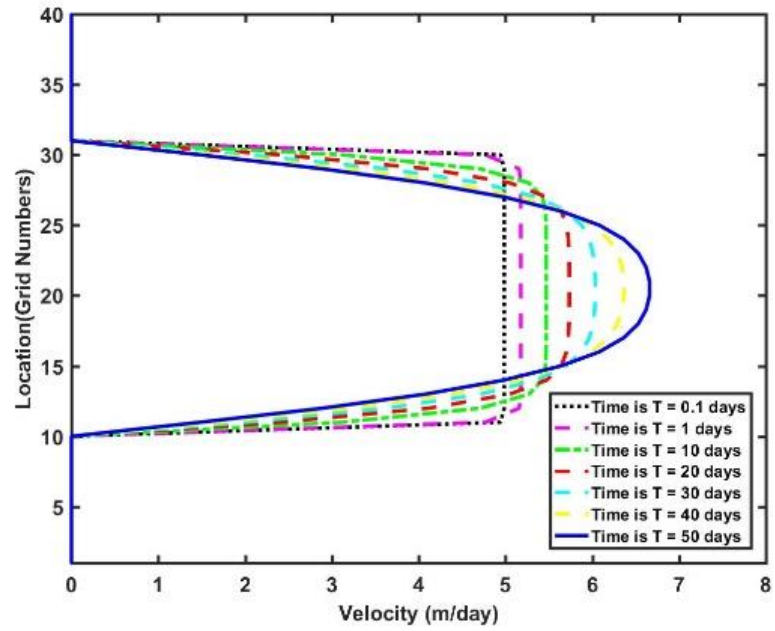


b)

Figure 21: Instantaneous tracer concentration after 50 days at location a) 0.25L from the inlet, b) 0.5L from the inlet



a)



b)

Figure 22: Velocity profiles for a) Steady flow, and b) Unsteady flow at the location 0.25L within the linear aquifer

5.4.2 Example 2

The second example is a more realistic and complex two dimensional heterogenous synthetic aquifer (Figure 23) of size $304.8 \times 304.8 \times 7.62 \text{m}^3$ ($1000 \times 1000 \times 25 \text{ft}^3$) located at a depth of 250m and is assumed to have an initial pressure of 2.41 MPa . The aquifer was meshed into $200 \times 200 \times 1$ grids and was assumed to be closed on all sides and the only flow within the aquifer is due to five injectors and six producers placed in the aquifer. Also, five observation wells were placed in the aquifer and were used to monitor the movements of the injected tracer. The rock and fluid properties are shown on Table 1. There are three main megakarstic structures as shown in Fig 23. The porous region is heterogeneous and the permeability within this region is log-normally distributed with an average value of $3.95 \times 10^{-15} \text{m}^2$.

The simulation time was 50 days, during which the producers produced water at a rate of $31.8 \text{m}^3/\text{day}$ ($\approx 200 \text{bbls}/\text{day}$) and the injectors injected tracer-laden water at a rate of $63.59 \text{m}^3/\text{day}$ ($\approx 400 \text{bbls}/\text{day}$). 169g/L of Cesium was injected from the injectors. The number of unknowns solved in the coupled continuity-transport equation is 119,600 and the number of unknowns in the Advection-Diffusion-Adsorption equation is 40,000.

Figure 24, shows the concentration distribution within the aquifer at different times when the unsteady Brinkman's equation was used. It is evident from the figure that the tracer transport within the conduits is much faster than that in the porous media. The transport in porous media is slower due to the lower permeability of porous material to flow and the adsorption of tracer on the surface of the rocks. Also, the figure shows that the tracer

injected from the well I3, which is located in the porous media, moves towards the cave due to a lower resistance to flow in the conduit. This is in spite of the fact that a producer P3 is located close to injector I3 and would exert some pull on the injected fluid.

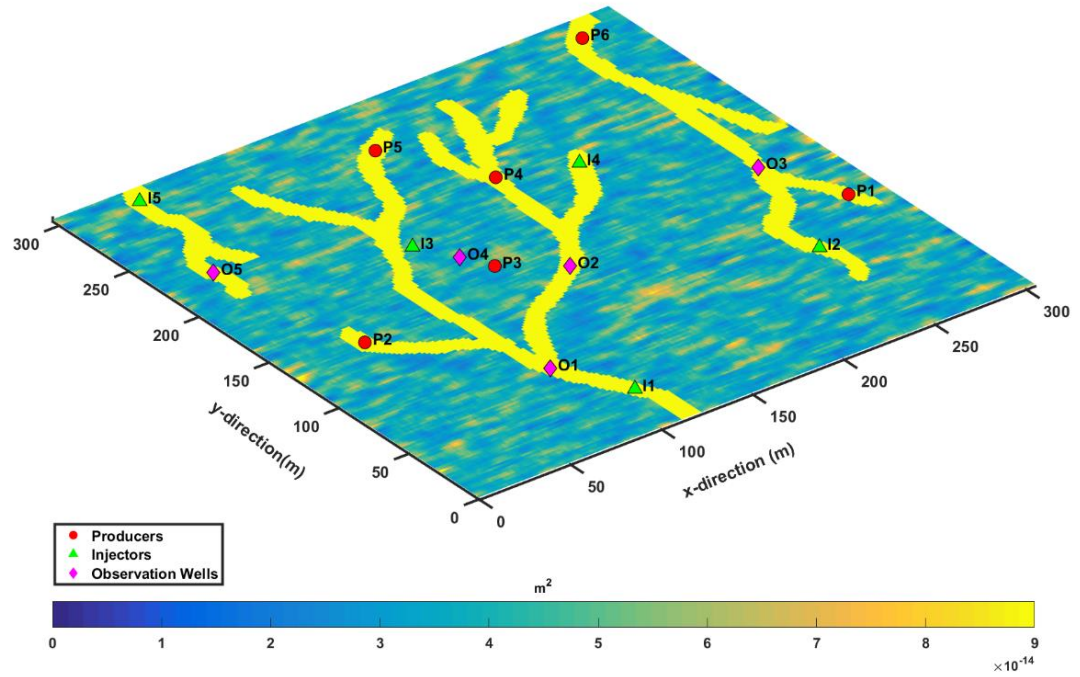


Figure 23: Schematic of the Synthetic Aquifer (Example 2)

The same problem in this example was solved using steady Brinkman's equation and the results were compared with those from the unsteady Brinkman's equation. The comparisons were made using the instantaneous concentration values obtained at the observation wells. Figures 25 – 29 shows the concentration values obtained from Observation Wells 1 to 5, using the Steady and Unsteady-flow Brinkman's equations. All the observation wells except O4 are located within the cave. At the observation wells within the caves (i.e. Figs. 25, 26, 27 and 29), the difference in tracer concentrations obtained from the steady and unsteady-flow Brinkman's model is apparent. In these cases, the unsteady flow Brinkman's model gave lower concentrations than the steady-flow Brinkman's model because its velocity profile takes time to fully develop. However, the difference in tracer concentration between the steady and unsteady-flow model, at the observation well O4 (located in the porous media), is very small and not obvious (Fig. 12). This shows that the effect of addition of unsteady flow parameter for a slightly compressible flow in porous media is negligible and can be neglected.

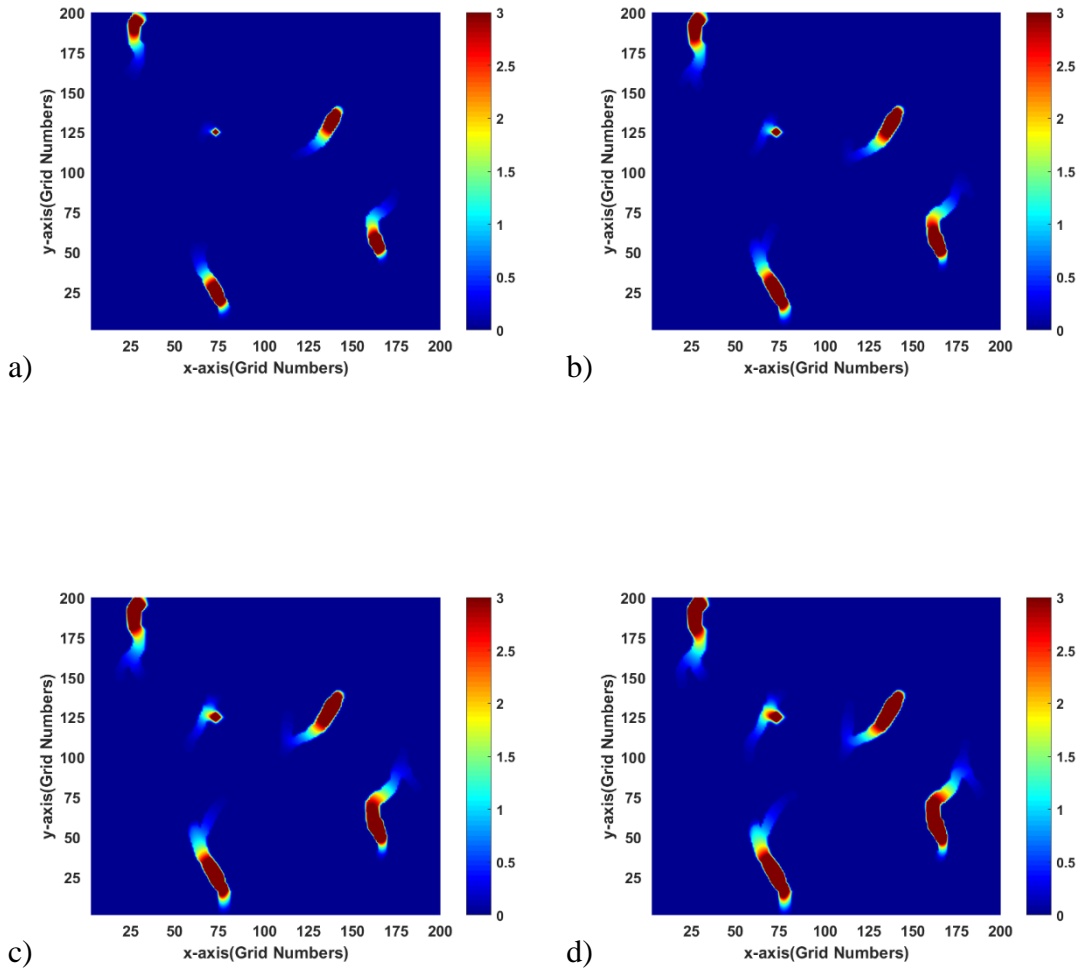


Figure 24: Tracer concentration obtained in the aquifer using Unsteady flow Brinkman's equation after a) 12.5 days, b) 25 days, c) 37.5 days, d) 50 days

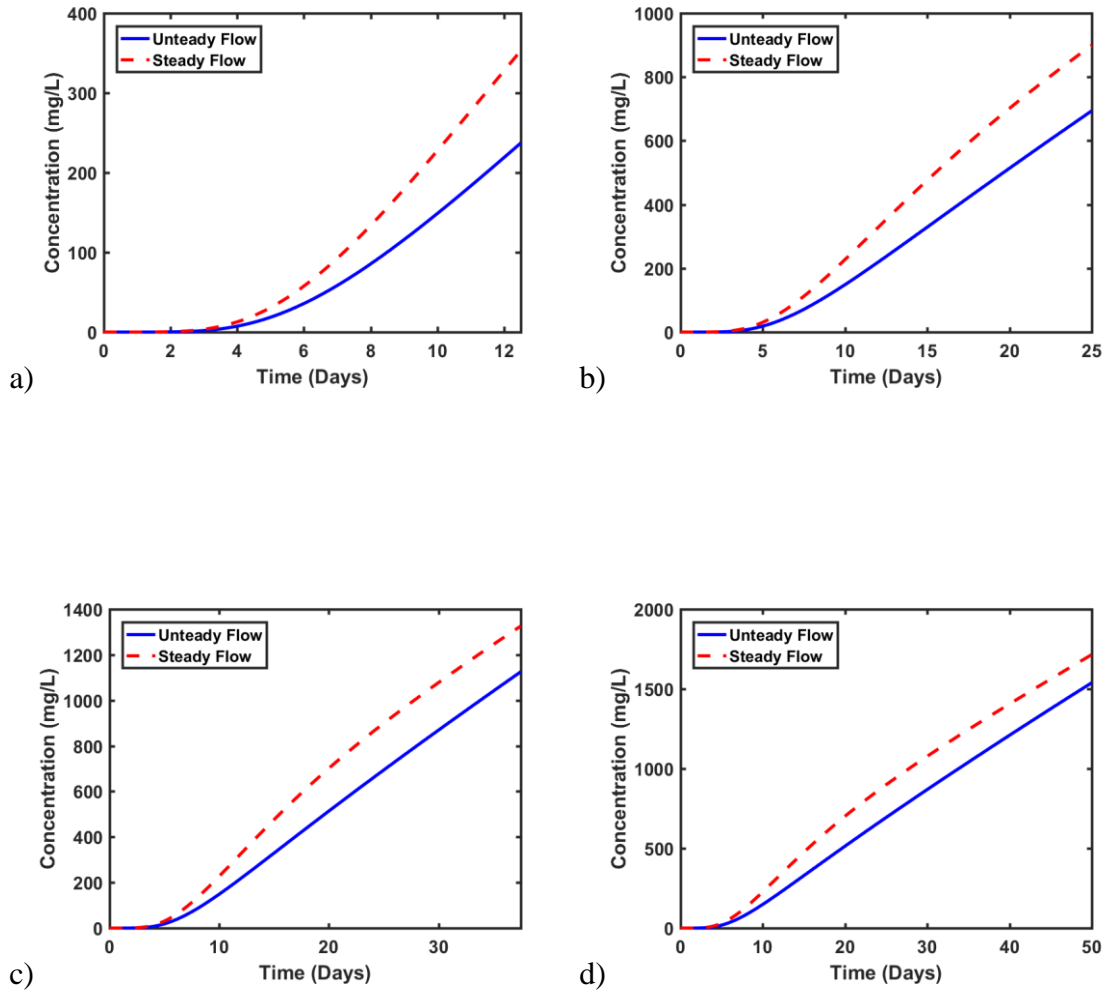


Figure 25: Instantaneous Concentration Profile at Observation Well 1 after a) 12.5 days, b) 25 days, c) 37.5 days, d) 50 days

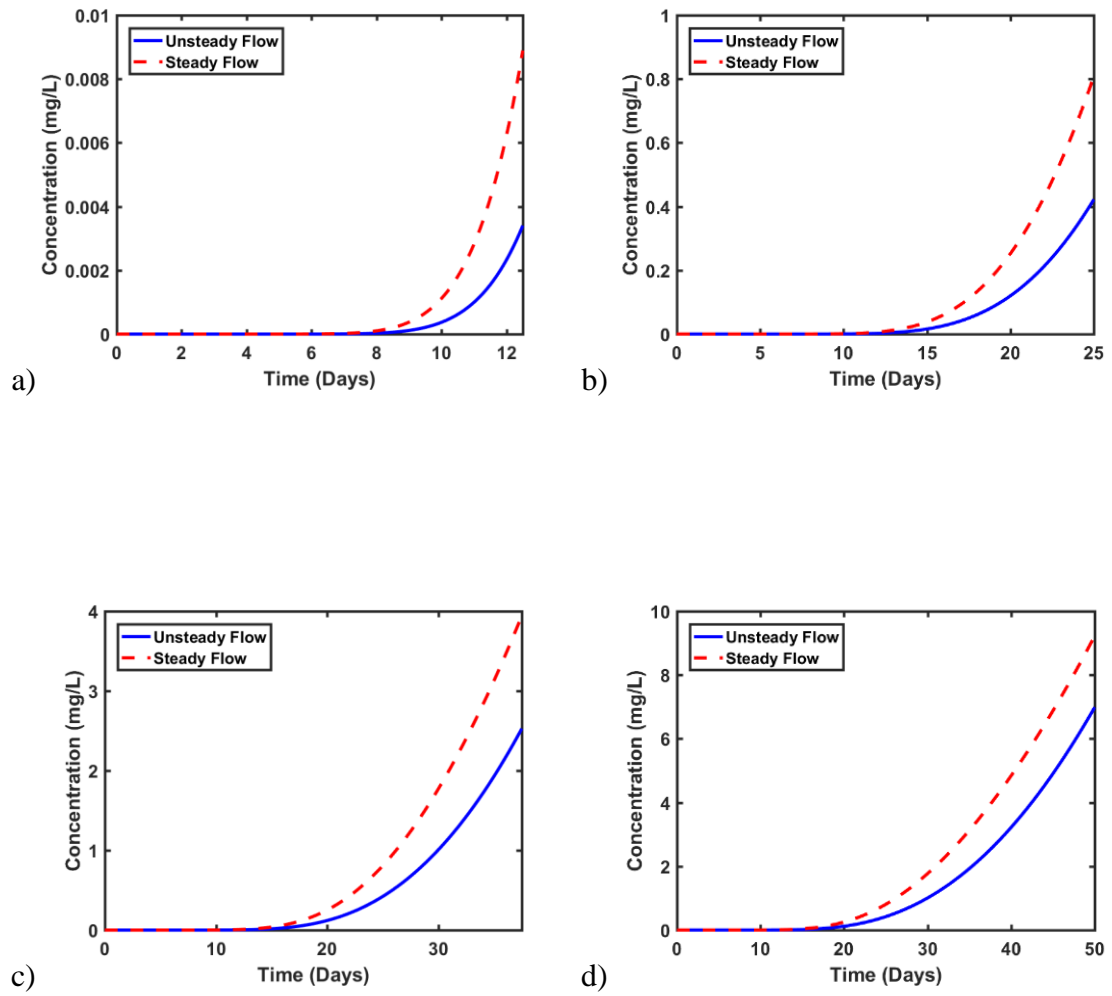


Figure 26: Instantaneous Concentration Profile at Observation Well 2 after a) 12.5 days, b) 25 days, c) 37.5 days, d) 50 days

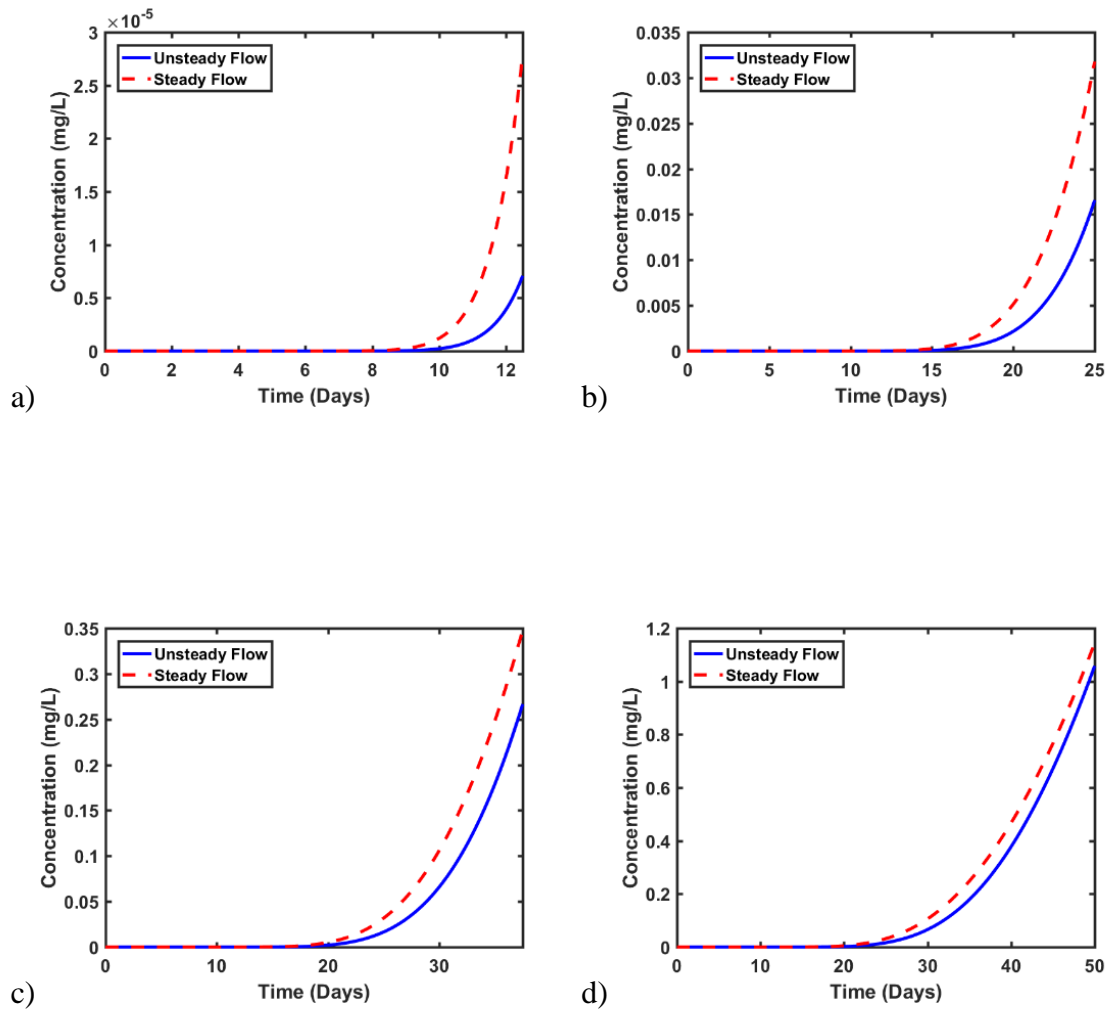


Figure 27: Instantaneous Concentration Profile at Observation Well 3 after a) 12.5 days, b) 25 days, c) 37.5 days, d) 50 days

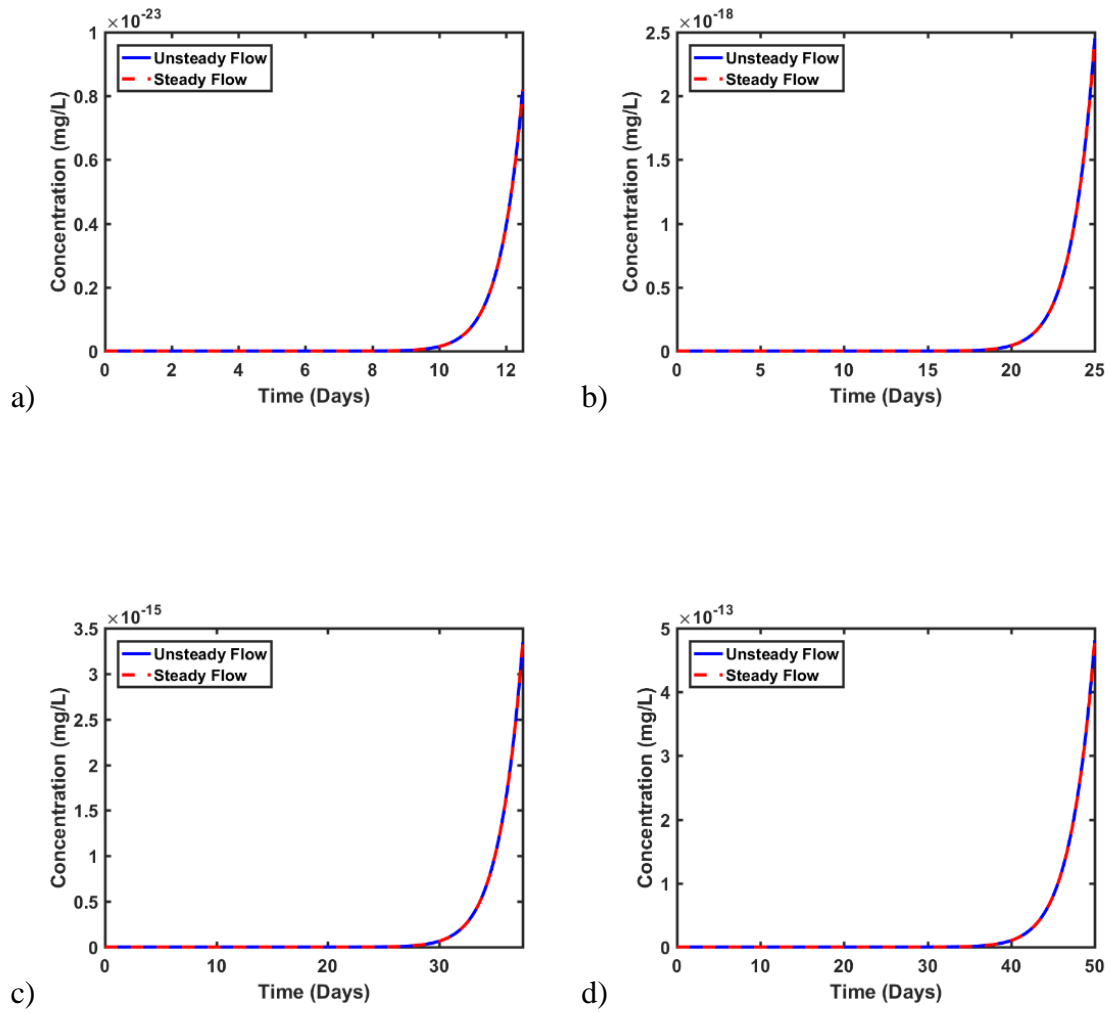


Figure 28: Instantaneous Concentration Profile at Observation Well 4 after a) 12.5 days, b) 25 days, c) 37.5 days, d) 50 days

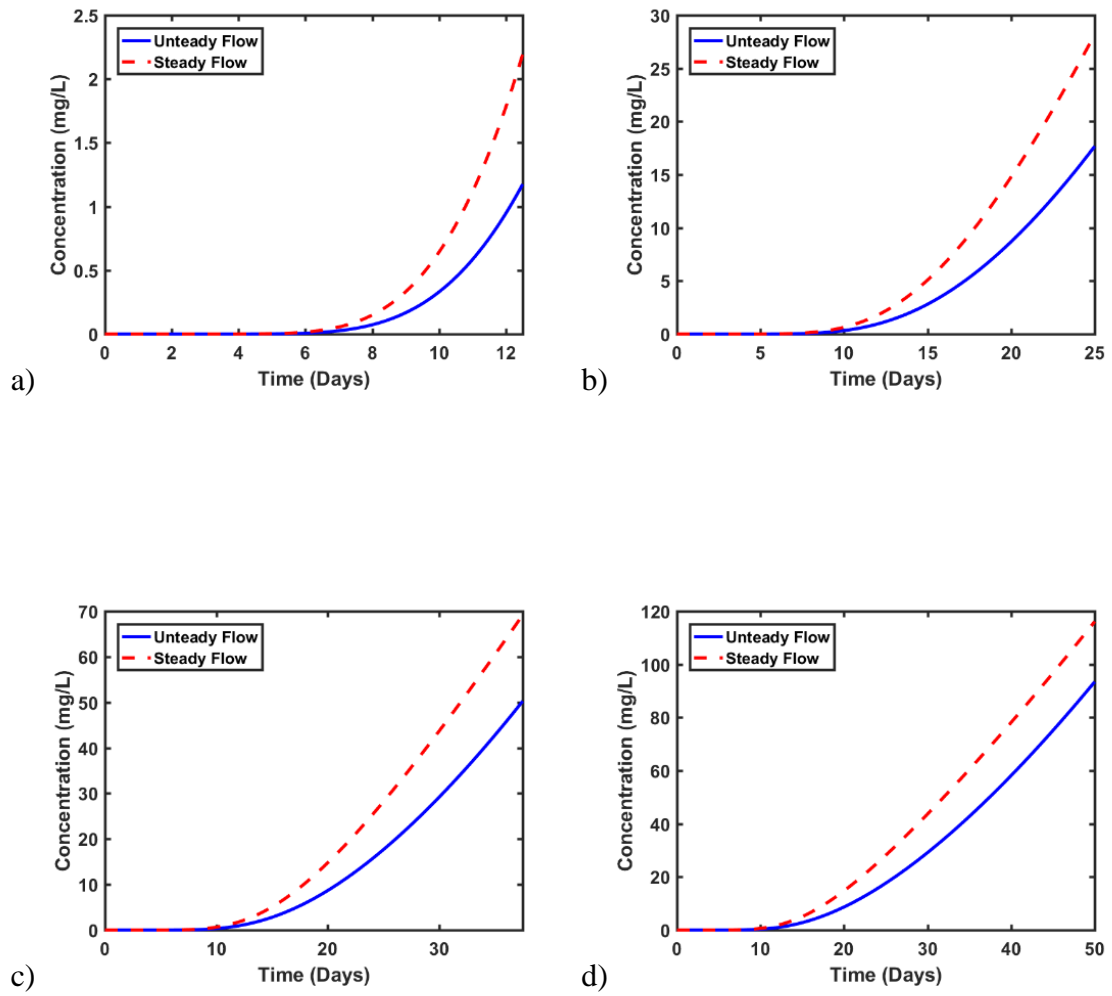


Figure 29: Instantaneous Concentration Profile at Observation Well 5 after a) 12.5 days, b) 25 days, c) 37.5 days, d) 50 days

5.5 Conclusions

An unsteady flow Brinkman's model was used to assess the effects of unsteady flow conditions in an aquifer. Unsteady flow Brinkman's model was obtained by adding the unsteady flow term present in the Navier-Stokes equation to the Brinkman's equation. We used the cell-centered finite-volume approach to solve the partial differential equation arising from the model. The results obtained from the unsteady flow Brinkman's equation were compared to those obtained from the steady flow Brinkman's model. The velocities obtained from the two models were used to simulate tracer transport within the karst aquifers by solving the advection-diffusion-adsorption equation. Two examples were presented to illustrate the effect of the unsteady-flow term on the simulation of tracer transport. The examples showed that the steady and unsteady flow models yielded different tracer concentrations at observation wells located in the free-flow region but almost equal concentrations values at observation points located in the porous media

CHAPTER 6

FULL FIELD TO SECTOR MODELLING FOR EFFICIENT SIMULATION IN KARST RESERVOIRS

6.1 Introduction

The Brinkman's model attempts to model flow within karst aquifers by simultaneously solving the mass continuity equation and the momentum equation (Brinkman's equation) for the pressures and velocity distribution within the karst aquifer. Because the Brinkman's model solves one continuity equation and up to three momentum balance equation per grid block, the method is very expensive particularly for large aquifers. The Darcy's model on the other hand does not require the need to solve multiple equations per grid. A simplification is made by replacing the velocity term in the mass continuity equation by the Darcy's law. This allows solving for only the pressure distribution at the new time step in the aquifer and then updating the velocities with these pressures. This makes the Darcy's model a very cheap alternative to the Brinkman' model. However, the Darcy's equation produces inaccurate results within the caves.

We propose a sector modeling approach for fluid flow in Karst aquifers. In this approach, sectors are carefully chosen to consist of only the caves and a small area of the porous region surrounding the caves. The Darcy's model is first solved in the entire aquifer to obtain the pressure and velocity distributions. The Brinkman's model is then used to solve for pressure and velocity in the identified sectors. Because the sectors are much smaller

than the aquifer, solving the Brinkman's model in these sectors is much faster than solving it in the entire aquifer. Thus, the method works in three stages: first solving the cheap Darcy's model in the entire aquifer, followed by solving the more expensive Brinkman's model on isolated sectors surrounding each distinct cave, and then updating results from the full-field model with those from the sector model. In addition to fluid flow modeling, tracer transport in the karst aquifer is implemented to enable us compare the performance of sector modeling with those of the Darcy's and Brinkman's models.

Two examples are presented to show the effectiveness of this method. The first example involves a simple aquifer model consisting of a cave surrounded on two sides by porous media. The second example is a more complex heterogeneous geological structure consisting of more realistic caves with randomly placed water producers and injectors. The results from the Sector modeling approach were compared with results from the Darcy's and Brinkman's models. Results showed excellent match between the sector modeling approach and the Brinkman's model. In addition, the sector modeling approach was much faster than the Brinkman's approach.

6.2 Mathematical Models for Flow

This section describes the differential equations governing the flow of a single-phase fluid in a complex karst aquifer and the mathematical formulations used to solve those equations

6.2.1 The Brinkman's Model

The mathematical equations and discretization of the Brinkman's model have been discussed in detail in the sections 4.2.1 and 4.2.2 of this manuscript

6.2.2 The Darcy's Model

Based on experimental observations, Darcy (1856) developed a simple correlation to model flow across porous media. The Darcy's equation, shown in Eq. 2.8 can be rearranged as

$$\vec{u} = -\mu^{-1} \overline{\overline{K}} \nabla p. \quad (6.1)$$

Similar to Brinkman's equation, Darcy's equation for flow has to be combined with the continuity equation (Eq. 2.7) to model flow in karst aquifers. In the Darcy's model, Eq. 6.1 is substituted into Eq. 2.7 to produce one parabolic equation:

$$\frac{\partial(\phi\rho)}{\partial t} - \nabla \cdot \left(\frac{\rho \overline{\overline{K}}}{\mu} \nabla p \right) = \frac{\rho q_w}{V_b}. \quad (6.2)$$

which can be solved for pressure. This means that only one equation is solved per grid block and the size of the linear system of equations remains $M \times M$, where M is the number of grids in the discretized system. Once the pressures are obtained, the velocities can be calculated using Eq. 9 wherever required. This method is well documented (Ertekin, Abou-Kassem and King, 2001; Chen, 2007). We note that in the Darcy's model, the permeability in the cave is set to a very high value typically $K \geq 10^{12}$, which is much greater than the permeability in the porous media.

6.2.3 Discretization of the Darcy's Model

Equation 6.2 can be written for slightly compressible flow as (Chen, 2007)

$$\nabla \cdot \left(\frac{\overline{\rho K}}{\mu} \nabla p \right) + \frac{\rho q_w}{V_b} = \phi \rho c_t \frac{\partial p}{\partial t}. \quad (6.3)$$

Equation 6.3 for a 2D aquifer can be expanded as

$$\frac{\partial}{\partial x} \left(\frac{\rho K_x}{\mu} \frac{\partial p}{\partial x} \right) + \frac{\partial}{\partial y} \left(\frac{\rho K_y}{\mu} \frac{\partial p}{\partial y} \right) + \frac{\rho q_w}{V_b} = \phi \rho c_t \frac{\partial p}{\partial t}. \quad (6.4)$$

The discretized form of Eq. 6.4 is given as

$$\begin{aligned} & \left(\frac{\rho K_y}{\mu} \right)_{h,i+\frac{1}{2}} p_{h,i+1}^{n+1} + \left(\frac{\rho K_x}{\mu} \right)_{h+\frac{1}{2},i} p_{h+1,i}^{n+1} \\ & - \left[\left(\frac{\rho K_y}{\mu} \right)_{h,i+\frac{1}{2}} + \left(\frac{\rho K_x}{\mu} \right)_{h+\frac{1}{2},i} + \left(\frac{\rho K_x}{\mu} \right)_{h-\frac{1}{2},i} + \left(\frac{\rho K_y}{\mu} \right)_{h,i-\frac{1}{2}} + \frac{\phi \rho c_t}{\Delta t} \right] p_{h,i}^{n+1} \\ & + \left(\frac{\rho K_x}{\mu} \right)_{h-\frac{1}{2},i} p_{h-1,i}^{n+1} + \left(\frac{\rho K_y}{\mu} \right)_{h,i-\frac{1}{2}} p_{h,i-1}^{n+1} = -\frac{\phi \rho c_t}{\Delta t} p_{h,i}^n - \frac{\rho q_w}{V_b} \end{aligned} \quad (6.5)$$

where h and i are the indices of the grid blocks in the x and y -directions, respectively, and n is the index of the time. The above equation is then solved for pressures across the aquifer at different time steps. There is only one pressure equation per grid and the solution can be computed in much less time. The pressure obtained from solving Eq. 6.5 is used to compute the velocity distribution in the aquifer. The computation of velocities in this case is very cheap as no system of linear equations is required.

6.3 Mathematical Models for Tracer Transport

The mathematical models for tracer transport has already been discussed in detail in Section 4.3 of this manuscript

6.4 Sector Modeling Approach

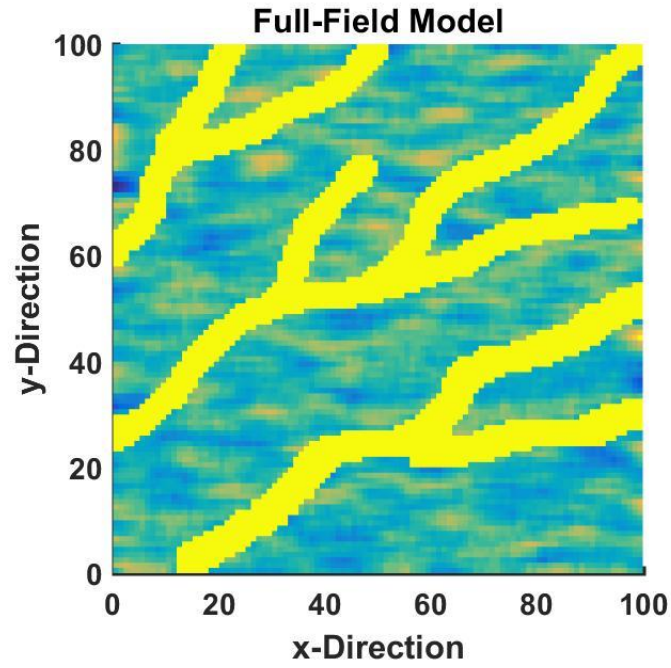
The numerical solution of the Brinkman's model is a computationally expensive but gives accurate fluid velocity profiles in both the porous media and the free-flow regions. On the other hand, the numerical solution to the Darcy's model is very cheap but gives an inaccurate fluid velocity profile in the free-flow region. Consequently, we introduce a sector modeling approach that exploits the computational inexpensiveness of the Darcy's model and the accuracy of the Brinkman's model in the caves. The sector modeling technique solves the Darcy's model on the full-field (entire aquifer) and then solves the Brinkman's model on small sectors carved out from the full-field. In doing so, dynamic-flux boundary conditions (obtained from the solution of the Darcy's model on the entire aquifer) are imposed on the sectors and the results obtained from solving the Brinkman's model (on the small sectors) are used to update the results from the full-field model. A description of the sector modeling approach is as follows:

1. Simulate the pressure distribution in the entire aquifer by solving the Darcy's model (Eq. 6.5). This is the full-field model.
2. Compute the velocities u_x , u_y and u_z at all grid interfaces using Darcy's law (Eq. 6.1).
3. Extract a small region surrounding each distinct cavern.

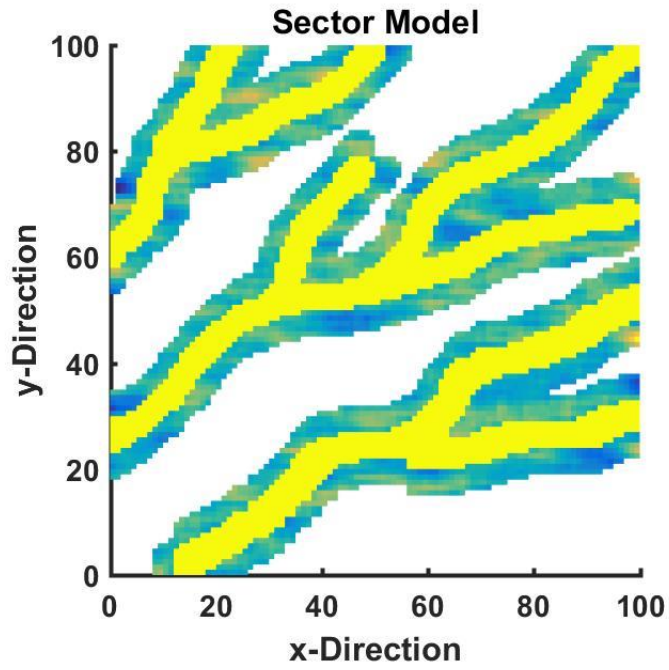
4. Set the velocities obtained at the grid interfaces forming the boundary of each sector as the dynamic-flux boundary condition for that sector.
5. Solve for pressure and velocity distributions in each sector using the Brinkman's model (Eqs. 2.7 and 2.13). This is the sector model.
6. Update the full-field model with the results from the sector models.
7. Model tracer transport using the velocity distribution in the updated full-field model.

Figure 30 illustrates the procedure used in sector modeling. Three distinct caves are present in the karst aquifer shown in Fig. 30a. In sector modeling, a sector surrounding each of these caves would be extracted to obtain three sectors as shown in Fig. 30b. Then the Brinkman's model is run on each of these small sectors to obtain reasonably accurate pressure and velocity distributions in the caves.

To avoid confusion, we define some terminologies introduced in this section. Cave is synonymous with free-flow region while Full-field is synonymous with entire aquifer. However, a full-field model involves solving the Darcy's model on the entire aquifer. A sector consists of a cave and a small porous region surrounding it. A sector is extracted from the full-field. A sector model involves solving the Brinkman's model on a sector while imposing dynamic flux boundary conditions (obtained from the full-field model) on the sector.



a)



b)

Figure 30: Sector extraction from full-field (a) full-field (b) extracted sectors. Note that the yellow regions indicate the caves

6.5 Example Applications, Results and Discussions

Two examples are presented to evaluate the accuracy and computational performance of the sector modeling technique. The first example is a simple two-dimensional linear aquifer model consisting of a cave surrounded on both sides in the y-direction by porous media. The second example is a more complicated heterogeneous aquifer consisting of more realistic cave-like structures embedded in porous media. The transport of a tracer is used to quantify the results.

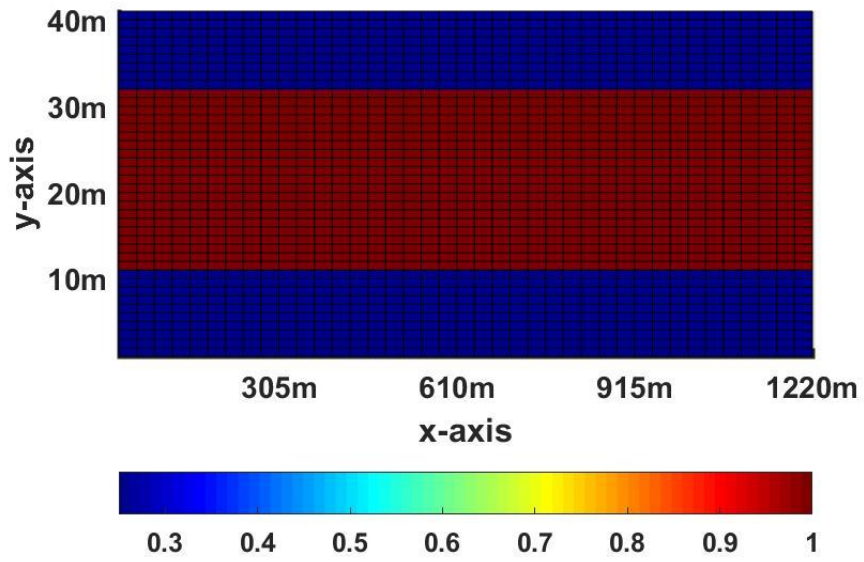
6.5.1 Example 1

The first example consists of a simple linear flow in a two-dimensional aquifer model being flooded from the left side at a velocity of 3.26 m/day. The aquifer, of dimensions $1220m \times 41m \times 1.5m$, was discretized into $40 \times 41 \times 1$ grids (Fig. 31). The aquifer is closed at the top and bottom. In Fig. 31a, the region with 100% porosity (red portion in the middle) is the cave, and this section corresponds to Grids 11–31. This region is surrounded by a porous media whose porosity is 25% (blue portions). The initial aquifer pressure was 1.38MPa. The aquifer rock and fluid properties are listed on Table 1. Initially, the concentration of tracer in the aquifer was set to zero. Then, $30g/L$ of tracer was injected from. The numerical simulation was run for 50 days.

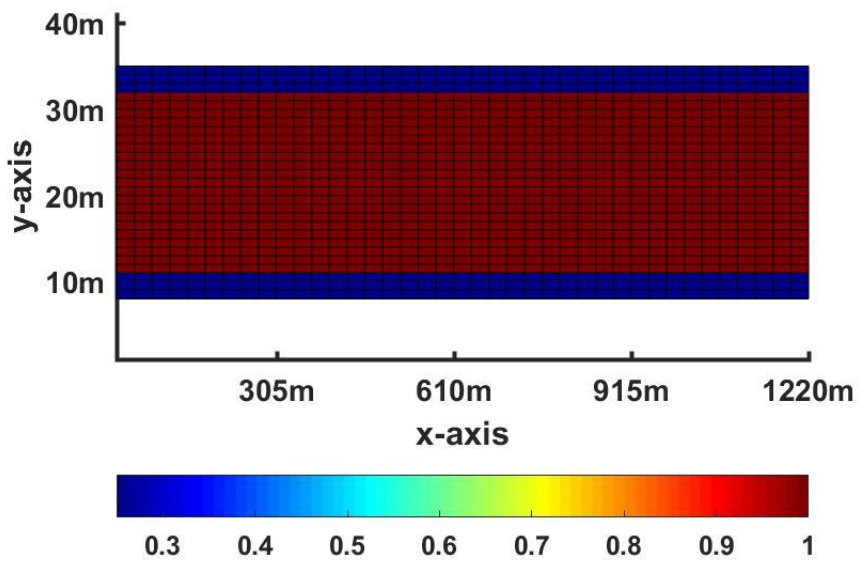
To apply the sector modeling approach, the full-field (Fig. 31a) is reduced to a sector (Fig. 31b). The number of grids was reduced from 1640 in the full-field to 1080 in the sector. Darcy's model was run on the full-field to obtain the aquifer pressure distribution. The velocity distributions in the full-field (Fig. 32a-c) are then computed from the pressure

distribution. The velocities at the locations where the sector is extracted from the full-field are used as the (flux) boundary conditions of the sector. Because these velocities change with time, the boundary conditions imposed on the sector is dynamic and will vary from one time to another. The Brinkman's model is subsequently run on the sector to obtain the pressure and velocity distributions in the sector. Results from the portion of the full-field model corresponding to where the sector was carved out are then replaced by the results from the sector model (Fig. 33a-c).

To evaluate the accuracy and performance of the sector modeling approach, the Brinkman's model and Darcy's model approaches were equally solved to obtain the pressure, velocity and concentration distributions in the aquifer. Results from the three approaches (Darcy, Brinkman and sector modeling) are shown in Figs. 34. The velocity profiles from the three approaches are displayed in Fig. 35. We observe an excellent match between the profiles from the sector modeling and Brinkman's model. The Darcy's model however gave a very poor match to the Brinkman's model. As shown in Fig. 34, the concentration distributions obtained from the sector modeling approach and the Brinkman's model are also similar to each other but different from that from the Darcy's model. Thus, the sector modeling approach is more accurate than the Darcy's model, with the accuracy of the sector modeling approach reasonably close to that of the Brinkman's model.



a)



b)

Figure 31: Schematic of the aquifer used in Example 1: (a) full-field (b) sector

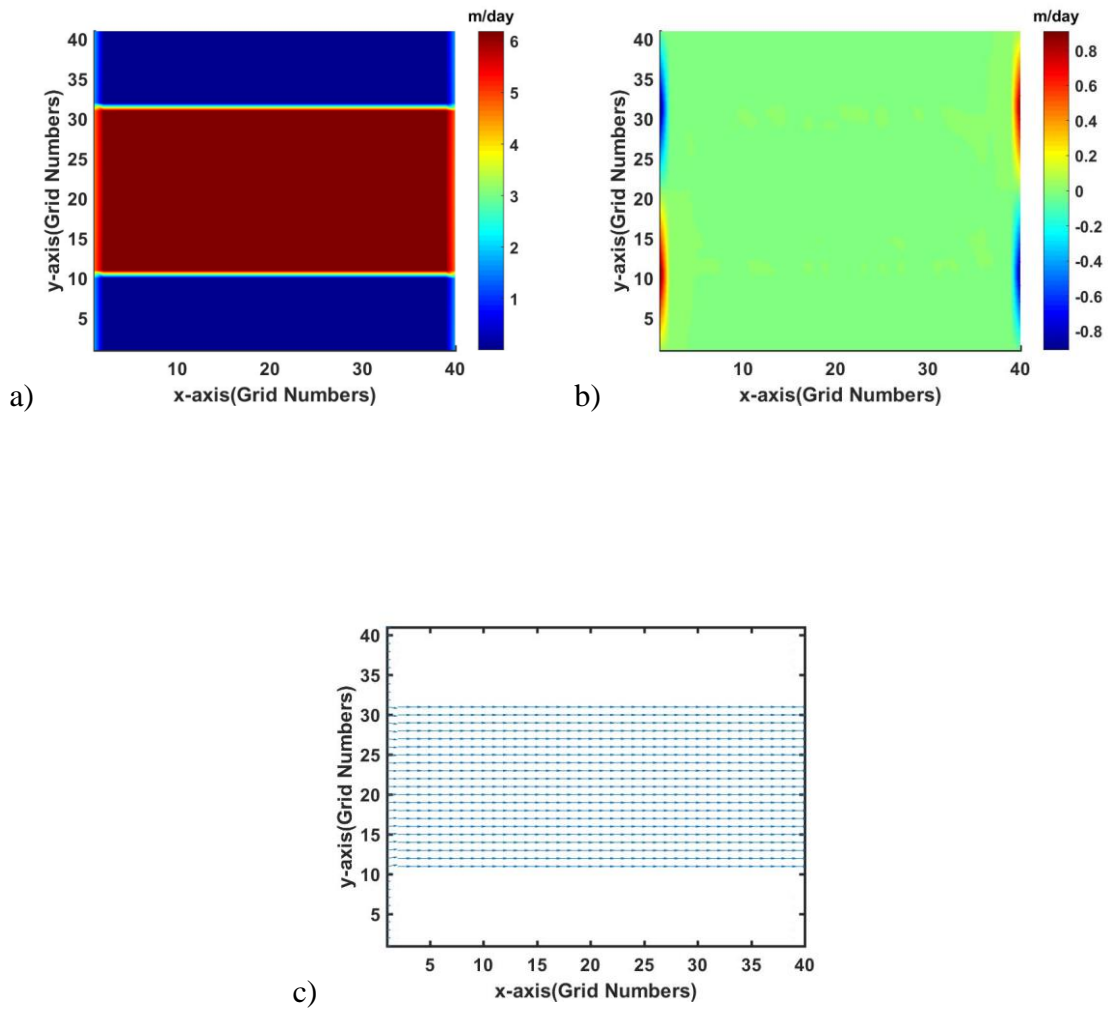


Figure 32: Velocity plots obtained after solving Darcy's equation on the full-field (a) velocity distribution in the x-direction, (b) velocity distribution obtained in the y-direction, and (c) Quiver plot using the velocity distributions in x and y-directions

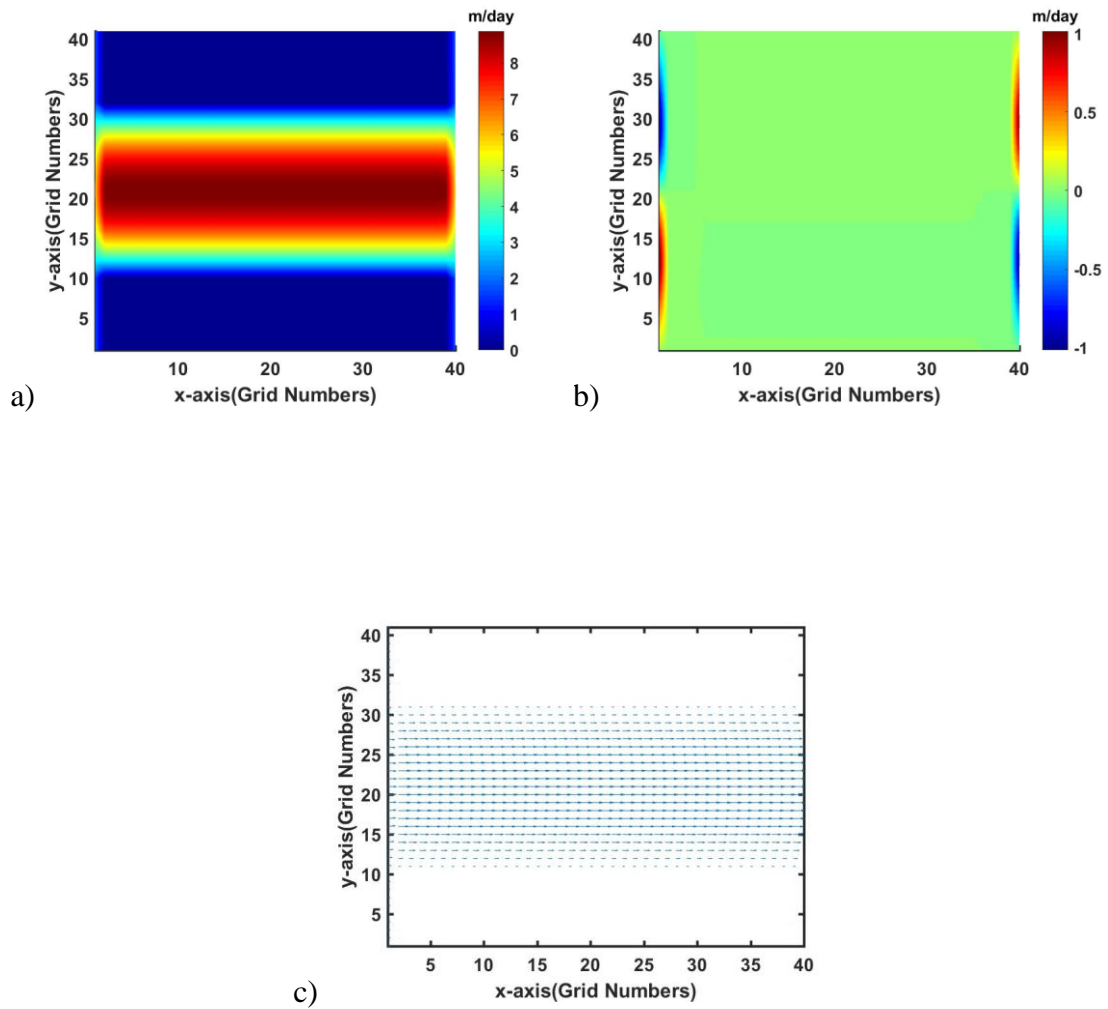
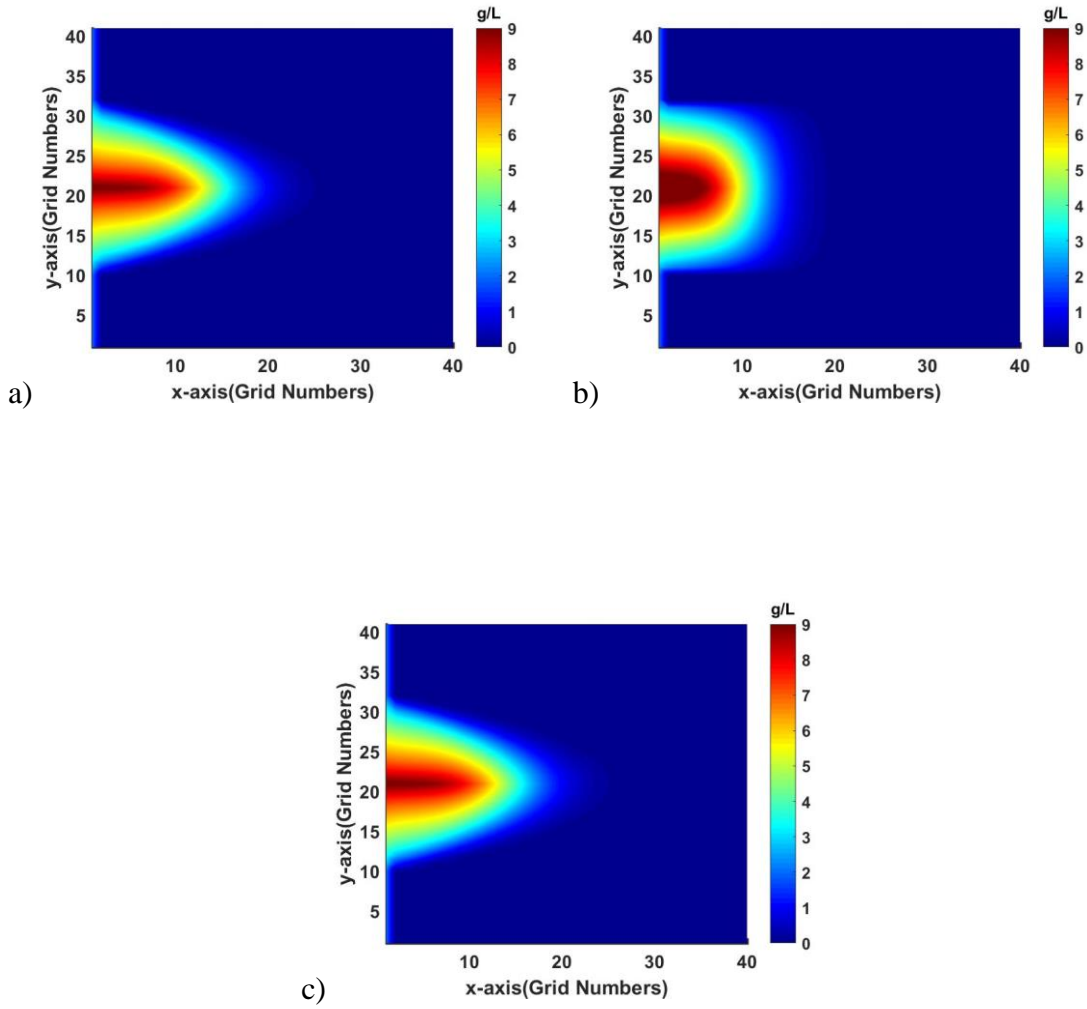


Figure 33: Velocity plots obtained after updating the results obtained from solving the Brinkman’s equation on the sector a) velocity distribution in the x-direction, b) velocity distribution obtained in the y-direction, and c) Quiver plot using velocity distribution



**Figure 34: Concentration maps from different modeling techniques (a) Brinkman's model
(b) Darcy's model (c) sector modeling technique**

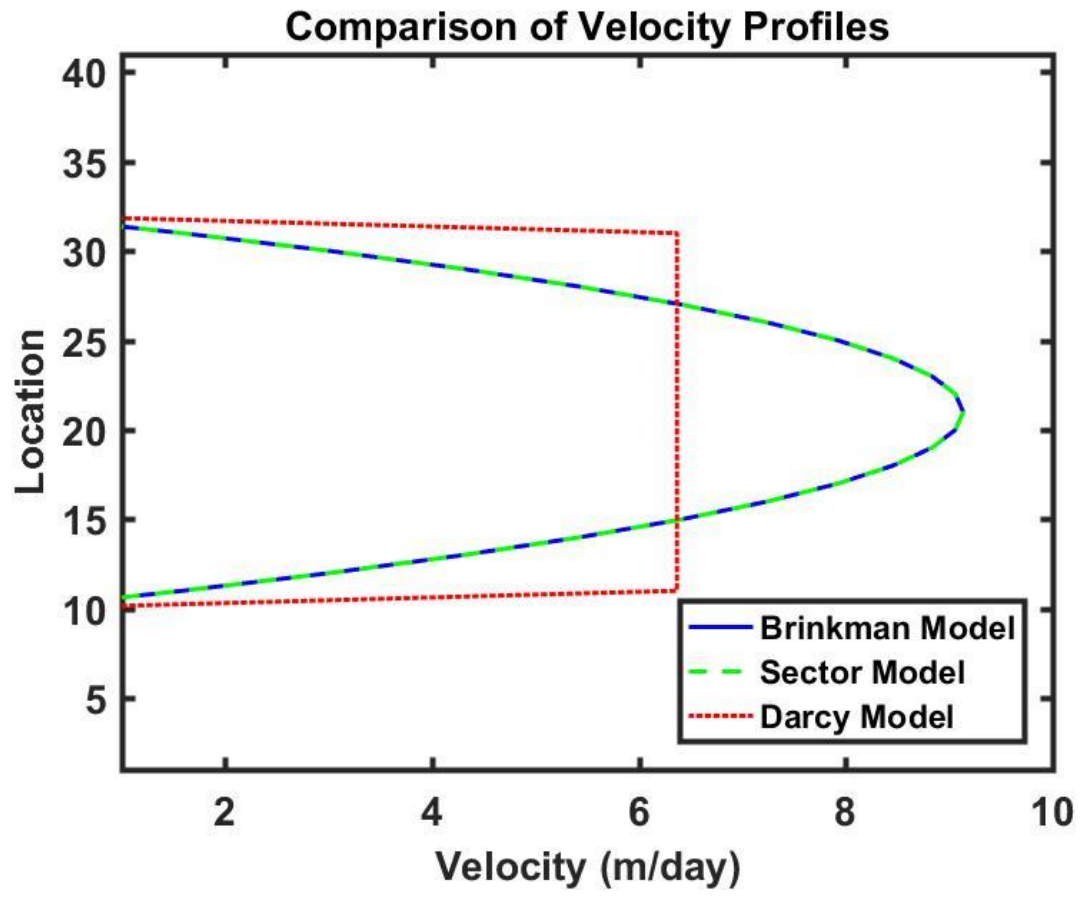


Figure 35: Velocity profiles from different modeling techniques

Figure 36 shows a plot of instantaneous tracer concentration at two different observation stations. The first observation station (Observation Station 1) is located in Grid (10,21), which is 305m from the inlet. The second observation station (Observation Station 2) is located in Grid (20,21), which is 610m from the inlet. We observe that the sector modeling technique gives a very close match to the Brinkman's model. Darcy's model however gives inaccurate and much lower concentration values when compared to the other two approaches.

Table 3 displays the sizes of the linear equations solved in the three approaches, their complexities, and the runtime taken to solve the problem by those approaches. Also, displayed on the table are the ratios of runtimes from the methods to the runtime from the Darcy's model. One way to roughly compare the computational performances of the approaches is by analyzing the complexity of problem solved in each approach. A method with a higher complexity requires larger simulation time. The set of linear equations generated in this example was solved using the LU factorization method. The computational complexity or the cost of computation of LU is given as (Boyd and Vandenberghe, 2004)

$$Cost = \frac{2}{3}n^3 + 2n^2 \quad (6.6)$$

where n is the size of the problem or the number of unknowns. For large values of n the leading term becomes dominant so that the second term ($2n^2$) becomes negligible and

thus can be neglected. Therefore, in calculating the cost of running the Brinkman's model and the Darcy's model we have used

$$Cost \approx \frac{2}{3}n^3. \quad (6.7)$$

Because there are two stages of simulation in the sector modeling approach, the computational complexity of this approach is computed from

$$Cost \approx \frac{2}{3}n_1^3 + \frac{2}{3}n_2^3 \quad (6.8)$$

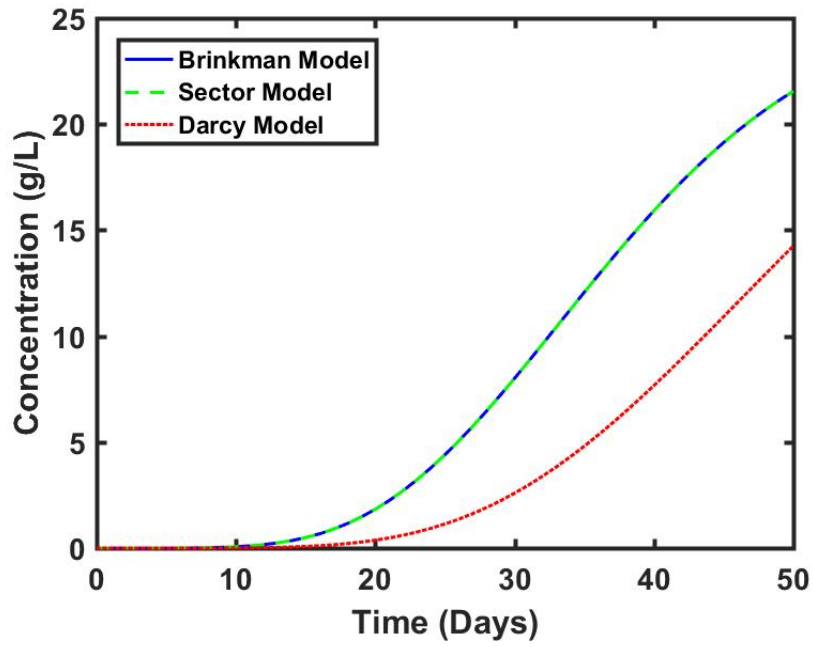
where n_1 is the size of the problem solved in the first stage (running the Darcy's model on the entire aquifer) and n_2 is the size of the problem solved in the second stage (running the Brinkman's model on the sector). The computational complexities of the three approaches in this example are listed on Table 3. We observe that the Brinkman's model has the largest complexity while the Darcy's model has the lowest complexity.

Darcy's model is the fastest of the three methods with a matrix size of 1640×1640 and a runtime of 6.941s (≈ 7.6 times faster than Brinkman's model). This is because the Darcy's model solves for only pressure and hence solves only one equation per grid block. The sector modeling technique is the second fastest (≈ 2 times faster than the Brinkman's model). The Brinkman's model is the slowest (with a runtime of 52.856s) due to its high computational complexity. We note the relative speed-up achieved by the sector modeling approach over the Brinkman's model approach depends on the size of the carved out sector relative to the full-field (entire aquifer). The smaller the sector relative to the aquifer, the

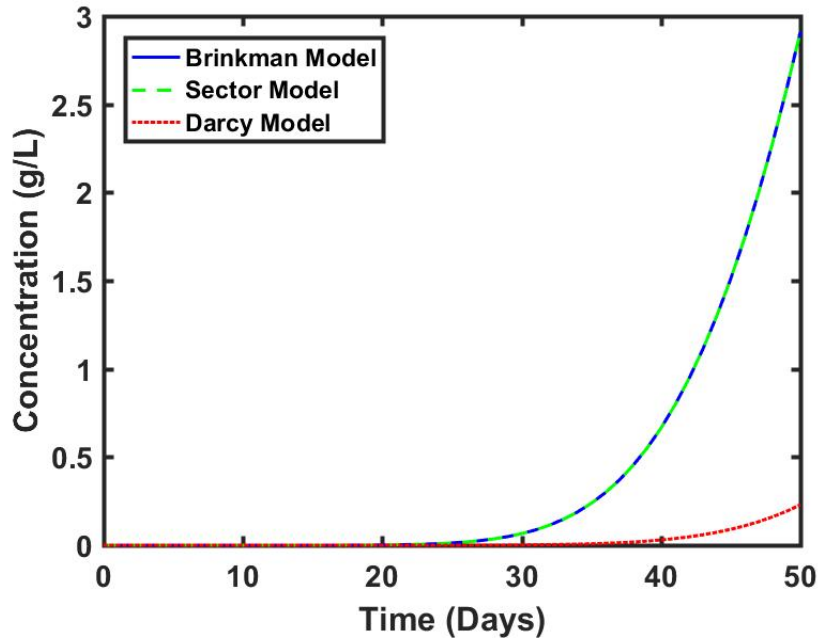
larger the speed-up in computational time. Also, where there exist several unconnected caves that require separate sectoral models, all those separate models can be simulated simultaneously if parallel computing is available. This is because the simulation of one sector does not rely on another sector for inputs. Rather, every sector takes input (in the form of dynamic flux boundary conditions) from the solution of the Darcy’s model on the entire aquifer (i.e. from the full-field model)

Table 3: Comparison of problem sizes and simulation runtimes (Example 1)

Model		Number of Unknowns	Coefficient Matrix Size	Computational Complexity	Runtime (seconds)	Time Ratio w.r.t Darcy Model
Brinkman's Model Approach		4839	4839×4839	7.56×10^{10}	52.856	7.615
Darcy's Model Approach		1640	1640×1640	2.95×10^9	6.941	1.000
Sector Modeling Approach	Full-field model	1640	1640×1640	2.43×10^{11}	26.193	3.774
	Sector model	3173	3173×3173			



a)



b)

Figure 36: Instantaneous contaminant concentrations obtained from the different modeling techniques at (a) Observation Station 1 (b) Observation Station 2

6.5.2 Example 2

The second example consists of a complex, more realistic, heterogeneous, two-dimensional aquifer (Fig. 37a). The aquifer dimensions are $304.8m \times 304.8m \times 7.62m$ ($1000ft \times 1000ft \times 25ft$). The aquifer is discretized into $200 \times 200 \times 1$ grid blocks. The initial aquifer pressure is $2.41MPa$. The cave is about $7.5m$ wide. The aquifer is closed on all sides and the flow and transport of tracers within the model is due to five randomly placed injectors and six randomly placed producers. The injector wells are responsible for injecting Cesium at a concentration of $30g/L$. The rock and fluid properties used in this example is the same as those used in Example 1 and is given on Table 1. The porous region is heterogeneous and the permeability within this region is log-normally distributed with an average value of $3.95 \times 10^{-15}m^2$ ($40md$). There are 6 producers each producing at a rate of $63.59m^3/day$ ($\approx 400bbls/day$) and 5 injectors each injecting at a rate of $31.79m^3/day$ ($\approx 200bbls/day$).

The numerical simulation was run for 50 days using a time-step of 0.1 day. Figure 37b shows the sector extracted from the aquifer. The number of grids in this sector is 7491 while that in the full-field is 40000. The Brinkman's model, Darcy's model and sector modeling approaches were used to solve for the pressure and velocity distributions in the aquifer and the results from these methods were used to solve for the tracer concentration in the aquifer. Table 4 lists the number of unknowns, the sizes of the coefficient matrices, the computational complexities and the runtimes associated with the three approaches. The table shows that the Brinkman's model approach has the highest complexity while the

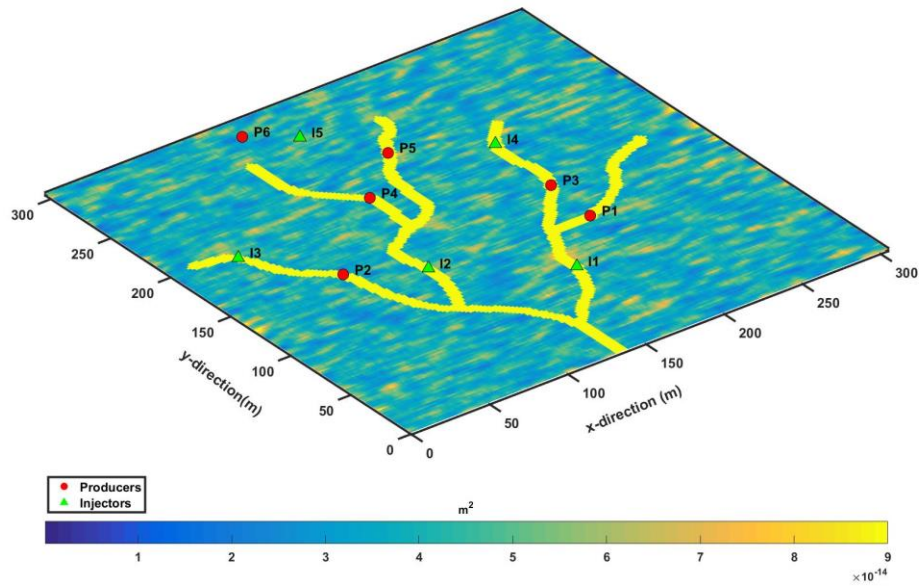
Darcy's approach has the lowest complexity. The table also shows that in this particular example, the Sector modeling approach is about 13 times faster than the Brinkman's model approach while the Darcy's model is about 27 times faster than the Brinkman's model approach.

Figure 38 shows the concentration distribution within the aquifer at different times obtained from the sector modeling technique. It is evident from the figure that tracer transport within the caves is much faster than that in the porous media. The transport in porous media is slower due to the lower permeability of porous media to flow and the adsorption of tracer on the surfaces of the rocks.

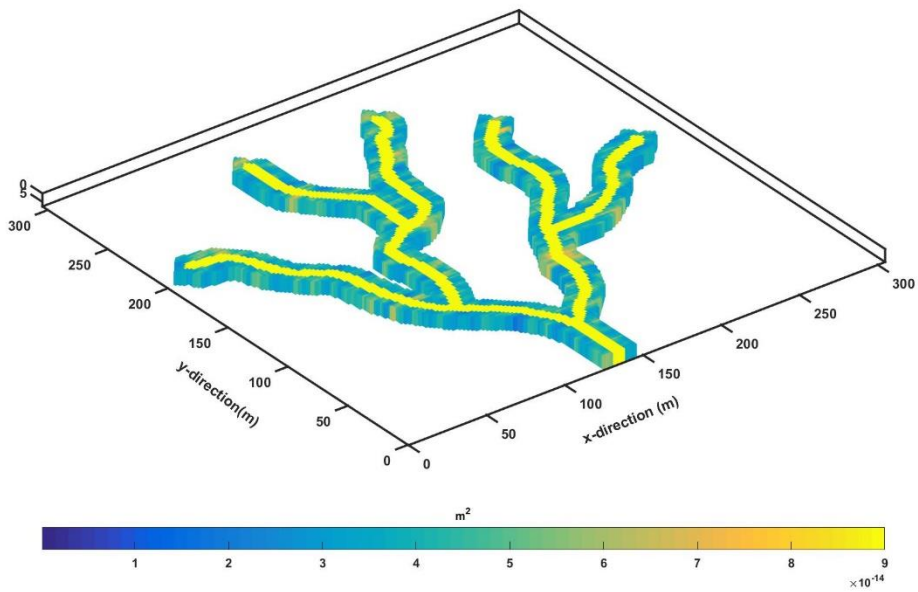
In Fig. 39, we compare the instantaneous tracer concentration observed at different production wells located within the aquifer. All the producers except P6 are located within the caves. The producer P6 is located in the porous region. It is evident from the figure that the Darcy's model gave wrong concentration values at the wells located in the caves. In fact, the Darcy's model underestimated the tracer concentration at the wells located in the caves. On the other hand, the sector modeling technique gave an excellent match to the Brinkman's model. In P6, all the three methods gave similar results because the Brinkman's model becomes Darcy's model in the porous media.

Table 4: Comparison problem sizes and simulation runtimes in Example 2

Model		Number of Unknowns	Coefficient Matrix Size	Computational Complexity	Runtime (seconds)	Time Ratio w.r.t. Darcy Model
Brinkman's Model Approach		119600	119600 × 119600	1.14×10^{15}	55021.27	27.887
Darcy's Model Approach		40000	40000 × 40000	4.27×10^{13}	1973.01	1.000
Sector Modeling Approach	Full-field model	40000	40000 × 40000	4.95×10^{13}	4161.09	2.109
	Sector model	21735	21735 × 21735			



a)



b)

Figure 37: The full-field, the wells and the extracted sector (a) full-field showing the wells

(b) extracted sector (Example 2)

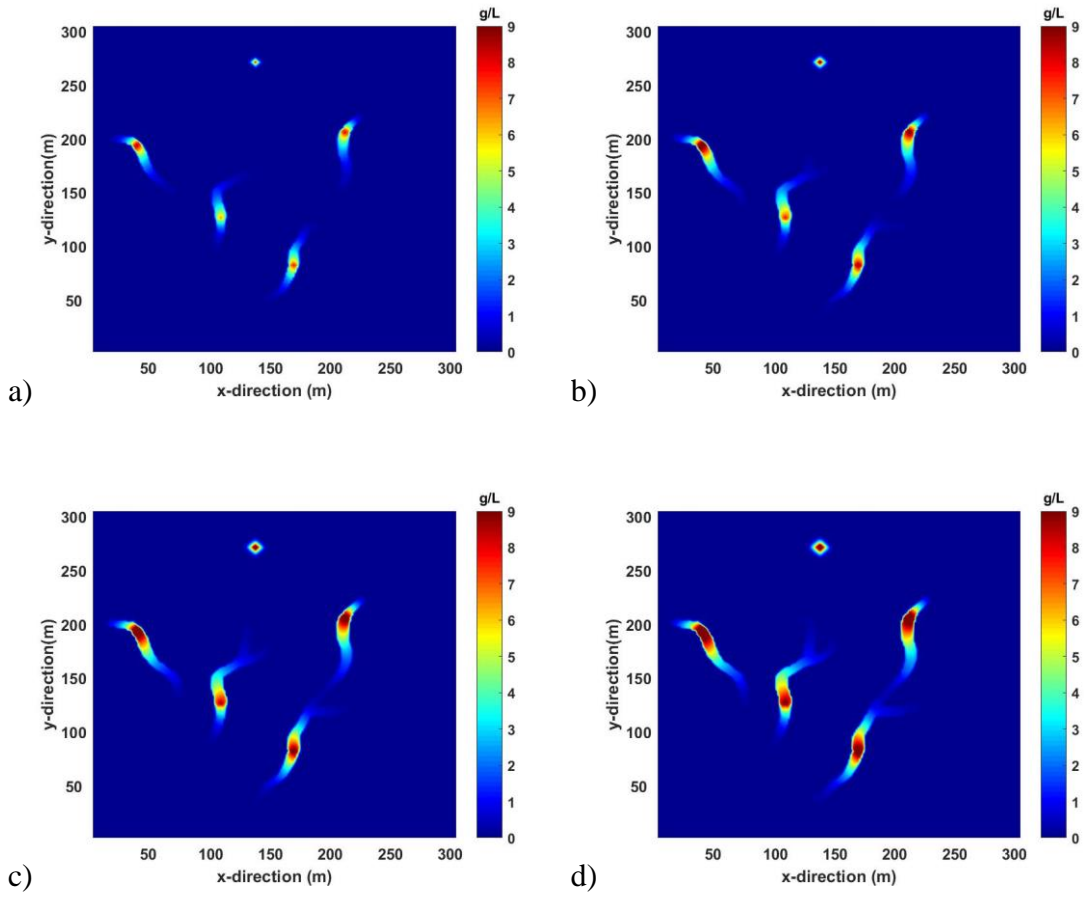


Figure 38: Concentration maps at (a) 12.5 days (b) 25 days (c) 37.5 days (d) 50 days.

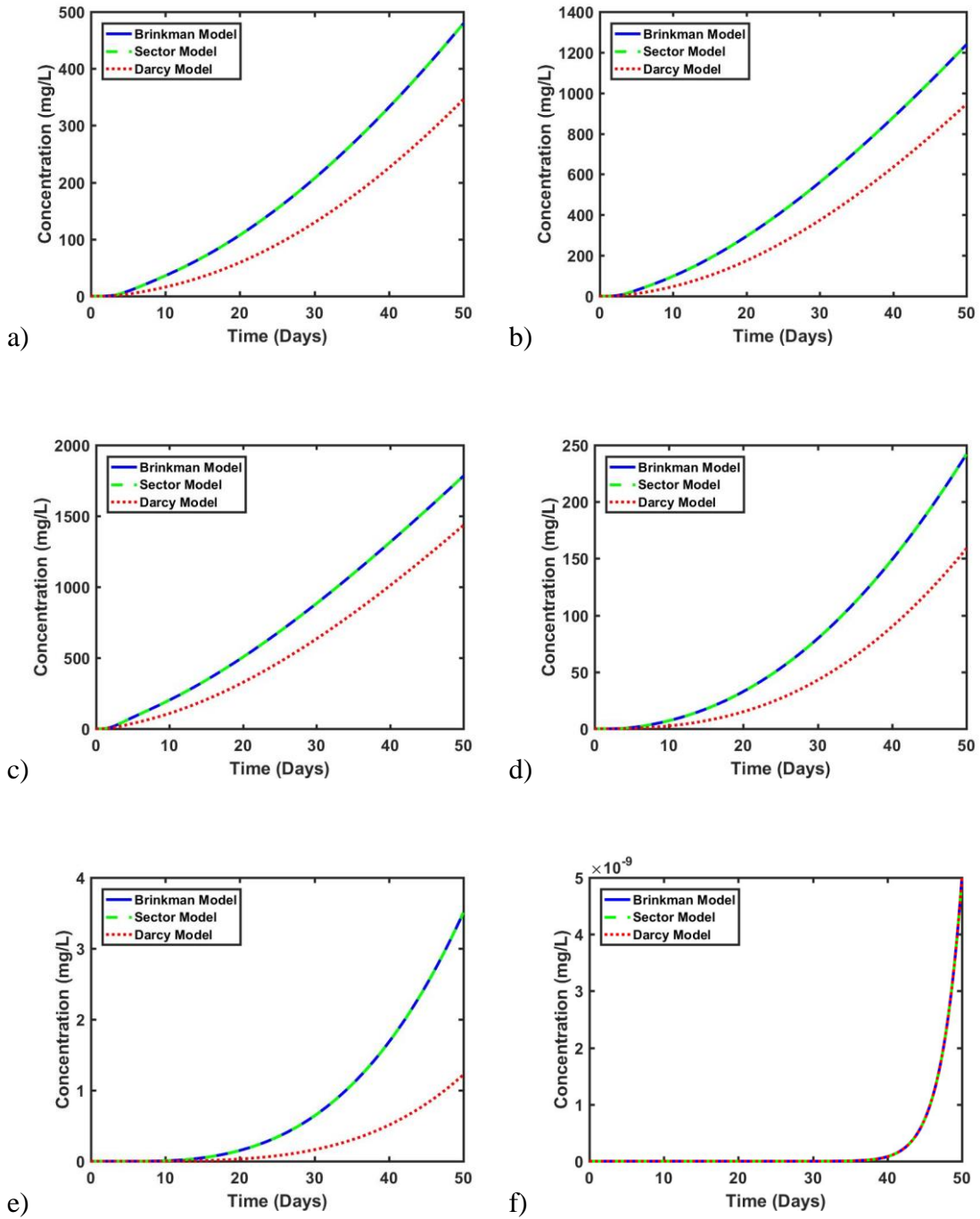


Figure 39: Instantaneous tracer concentration at different production wells (a)P1, (b)P2, (c)P3, (d)P4, (e)P5 and (f)P6

6.6 Conclusion

A sector modeling approach was proposed to model fluid transport in karst aquifers. The approach involves first solving the Darcy's model on the entire aquifer (full-field model), then solving the Brinkman's model on small sectors extracted from the aquifer (sector model) and finally updating the results from the full-field model with those from the sector model. Each sector is extracted from a region surrounding a distinct cave in the aquifer. The method exploits the fast computation associated with the Darcy's model and the accuracy of modeling flow in the caves associated with the Brinkman's model. Thus, the method runs much faster than the Brinkman's model without compromising the accuracy of results obtained in the caves.

Two examples were presented to illustrate the effectiveness of the sector modeling approach. The first example uses a simple cave surrounded by porous regions in two dimensions while the second involves flow in a larger and more complex heterogeneous aquifer with realistic cave structures. Both examples clearly show that the sector modeling approach is computationally more efficient than the Brinkman's model and it also gives results that matches those from the Brinkman's model. The Darcy's model although runs faster than both the Brinkman's model and the sector modeling approach, gave inaccurate results within the free-flow regions. We also noticed that the computational speed-up realized from the sector modeling approach is higher when the size of the extracted sector relative to the full-field is smaller.

CHAPTER 7

DARCY MODEL WITH OPTIMIZED PERMEABILITY DISTRIBUTION (DMOPD) TECHNIQUE FOR EFFICIENT SIMULATION IN KARST RESERVOIRS

7.1 Introduction

As discussed in the previous chapter the issue with both the Brinkman's model and the Darcy-Stokes model is that although both provide fairly accurate results, they are however computationally expensive as both these methods attempt to model flow within karst aquifers by simultaneously solving the mass conservation equation and up to three transport equation per grid block, for the pressure and velocity distribution within the aquifer. Darcy's model on the other hand although inaccurate provides a cheaper alternative to the other models as it does not need to solve multiple equations per grid. A simplification wherein the transport equation (Darcy's equation) is substituted into the mass conservation equation requires the solution of only one parabolic equation for pressure distribution throughout the aquifer.

The velocity profile obtained when using the Darcy's model has a more flattened and piston like shape which is not accurate and hence it underestimates the flow and therefore contaminant transport within the aquifer. The actual velocity profile obtained within free-flowing regions should be parabolic in shape which is obtained when using the Brinkman's equation or the Navier-Stokes equation. It was observed after running a few test cases that

Darcy's model can be used to mimic the velocity profile obtained from the Brinkman's equation by using a gradually decreasing permeability values from the center towards the edges of the free-flowing regions instead of using a single value throughout. This can be done by fixing the value of permeability at the center of the free-flowing region equal to the value obtained from comparing the Darcy's law to the Poiseuille Equation of flow between two parallel plates (k_{\max}). The permeability values for the consequent zones can then be obtained by multiplying k_{\max} with a value between 0.1 – 1 (permeability ratio). This value is largest for the zone next to the central region and decreases towards the boundaries of the free flow region. Hence in this study, we propose the use of Darcy's model with optimized permeability distribution (DMOPD). This method comprises of the following steps: Firstly, the Brinkman's model is run on the whole aquifer for the first timestep. The next step comprises the estimation of the permeability ratios using a global optimization technique such as differential evolution (DE). The computations are further sped up by parallelly computing each agent within an iterant. Finally, the Darcy's model is run for the remaining timesteps using the optimized values of permeability obtained in the second step.

Three examples are presented to compare the effectiveness of this method to the other existing methods. The first example involves a simple aquifer model consisting of a cave surrounded on two sides by porous media, this example has a small problem dimension with the aquifer having been discretized into $40 \times 41 \times 1$ grids. The second example has a slightly larger problem dimension with the aquifer having been discretized into $200 \times 200 \times 1$ grids. It has a more complex heterogeneous geological structure consisting

of more realistic caves with randomly placed water producers and injectors. The third example has the largest problem dimension with the aquifer having been discretized into $400 \times 400 \times 1$ grids. Similar to the second example this is also a complex heterogeneous geological structure being flooded from one corner of the aquifer and water being produced from randomly located producers. The results from the DMOPD modeling approach were compared with results from the Darcy's model and the Brinkman's model. Results showed a fairly accurate match between the DMOPD approach and the Brinkman's model. DMOPD method was also faster when compared to the Brinkman's model.

7.2 Optimization Strategy

The permeability ratios within the different zones in the caves are estimated using a global optimization algorithm. We have used differential evolution (DE) as the global optimizer in this work and this section describes the DE algorithm.

7.2.1 Differential Evolution (DE)

Differential evolution is an evolutionary type global optimization algorithm developed in 1997 (Storn and Price, 1997). At each generation, the DE generates a population of agents (N_p). The population size can be determined using the equation

$$N_p = 4 + \text{floor} \left[3 \times \log(M) \right], \quad (7.1)$$

where, M is the problem dimension or in our case the length of vector \vec{r} , and the $\text{floor}(\)$ function rounds a number to its nearest integer towards negative infinity. Equation 7.1 has

previously been used in literature to obtain the population size for different evolutionary algorithms (Auger and Hansen, 2005; Liao and Stützle, 2013). It has also been shown to be very efficient with DE (Awotunde, 2015, 2016).

The best agent and its fitness values are saved as the best solution (\vec{x}_b^τ) found for the current generation τ . This is updated whenever a better solution is found during the optimization process. The candidate agents for the next generation is then created using methods such as mutation, cross-over and selection. For a given vector \vec{x}_j^τ , the mutation process is carried out by first selecting three other random vectors $\vec{x}_{k1}^\tau, \vec{x}_{k2}^\tau$, and \vec{x}_{k3}^τ from the population. A mutant vector $\vec{v}_j^{\tau+1}$ is then generated using the equation

$$\vec{v}_j^{\tau+1} = \vec{x}_{k1}^\tau + F(\vec{x}_{k2}^\tau - \vec{x}_{k3}^\tau), \quad (7.2)$$

or,

$$\vec{v}_j^{\tau+1} = \vec{x}_b^\tau + F(\vec{x}_{k1}^\tau - \vec{x}_{k2}^\tau), \quad (7.3)$$

where, $F \in [0, 2]$, is the mutation factor.

The cross-over is carried out by generating a trial vector $\vec{\alpha}_j^{\tau+1}$ from each parent vector \vec{x}_j^τ .

A crossover parameter, $CR \in [0, 1]$, is selected at random by the user, and a random number is drawn from a uniform distribution between zero and one. The drawn number is then compared to the crossover parameter, if it is less than the crossover parameter the element in the trial vector is picked from the mutant vector, otherwise it is picked from

the parent vector. The final step is selection, which is carried out by comparing the fitness values from both the trial vector and the parent vector. The vector which gives the minimum value is selected for the next generation. This process of mutation, cross-over and selection is carried out until a pre-determined stopping criteria has been reached

7.3 The Darcy Model with Optimized Permeability Distribution (DMOPD) Approach

The Brinkman's model is computationally expensive but accurate in modeling flow in karst aquifers. Its high computational requirement results from the fact that it requires the simultaneous solution of mass conservation and up to three transport equations for a 3D aquifer. The Darcy's model on the other hand is computationally cheap but is less accurate in modeling fluid flow within the caves.

Here, we introduce a Darcy Model with Optimized Permeability (DMOPD) approach which divides the caves into an odd number of zones and then estimates an apparent permeability value in each zone such that using the optimized permeability values, the Darcy's model can accurately describe the true velocity profile of flow similar to that obtained from the Brinkman's model. To estimate the permeability distribution within the zones, a parameter-estimation algorithm is used to obtain an acceptable match between the velocity distribution in the cave computed by the Darcy's model and that computed by the Brinkman's model. Thus, within the parameter estimation framework, the objective function minimized to obtain the set of permeability ratios that provide a velocity profile match of the Darcy's model with the Brinkman's model is given as

$$\Phi(\vec{r}) = \frac{1}{\xi} \|\vec{u}_{BE} - \vec{u}_D\|_2^2, \quad (7.4)$$

where \vec{r} is the vector of unknown permeability ratios, \vec{u}_{BE} is a vector containing the velocities u_x , u_y and u_z in all the grids within the caves, calculated using the Brinkman's model at the first time-step, \vec{u}_D a vector containing the velocities u_x , u_y and u_z in all the grids within the caves, calculated using the Darcy's model, and ξ is the length of vectors \vec{u}_{BE} and \vec{u}_D . Notice that these are velocities computed within the caves only.

The steps involved in the DMOPD approach are the following:

1. At the first simulation time-step, use the Brinkman's model to compute the pressure and velocity distribution in the aquifer.
2. Partition each cave in the aquifer into an odd number of zones.
3. Assign a maximum permeability value, k_{max} to the zone in the central zone of each cave.
4. Use an efficient optimization algorithm to compute the ratio of permeabilities in the other zone with respect to the permeability in the central zone. This ratio should decrease as we move toward the walls of the cave.
5. Compute the permeability value for each zone within the cave by multiplying the estimated permeability ratio for that zone by the permeability value (k_{max}) assigned to the central zone.
6. Use the Darcy's model with the optimized permeability distribution to model velocity and pressure distribution for the remaining time-steps.

7. Model the tracer transport at subsequent time-steps using the velocity distribution obtained in Step 6.

In Step 3, k_{max} is obtained from Poiseuille's equation for flow in pipes. The global optimization performed in Step 4 is carried out using parallel computation techniques, whereby the objective function for each agent in an iteration is computed simultaneously.

Figure 40 illustrates the procedure of the selection of zones within the caves. The cave in the example shown in Fig. 40 is divided into nine zones, four on each side of the high permeability central zone (Zone 5). As can be seen in Fig. 40c, corresponding zones on the two sides of the central zone have the same permeability ratio. Thus, every zone except the central zone occurs twice so that we only have labels for Zones 1 to 5 for this nine-zone partitioning. The permeability ratio of each of Zones 1 to 4 is then estimated using an optimization algorithm. The permeability ratio is the ratio of the permeability in that zone to the ratio of the permeability in the central zone.

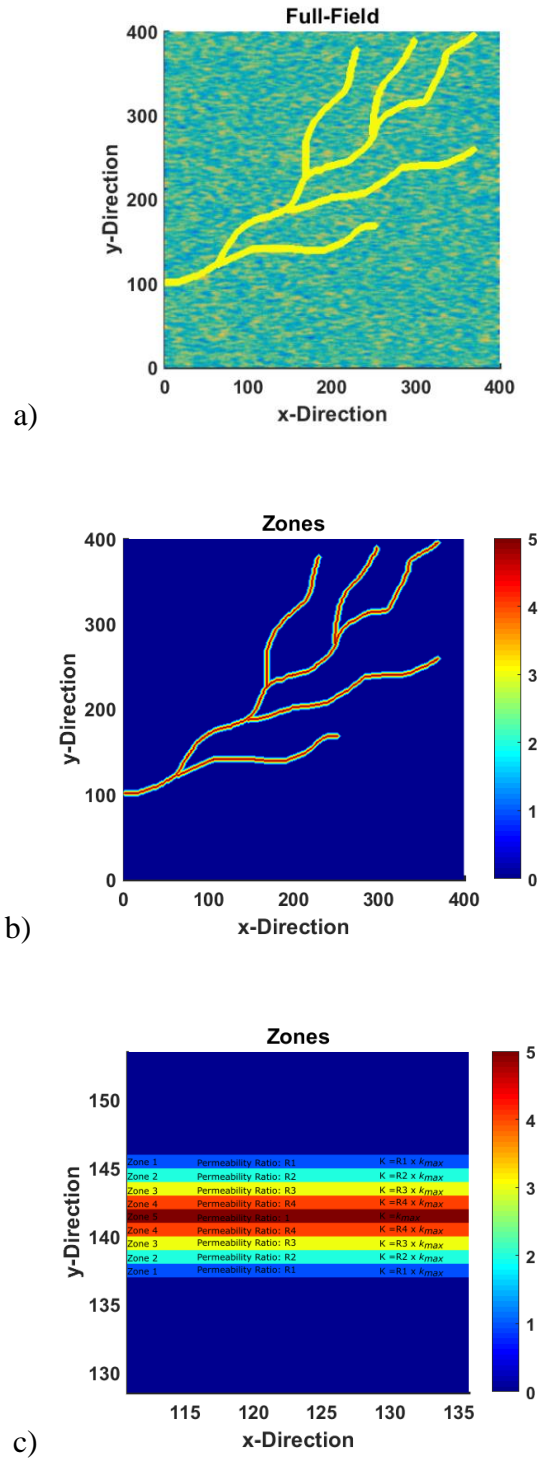


Figure 40: Figure showing the division of caves into different zones and the permeability assignment into those zones (a) full-field model (b) division of caves into different zones (c) magnification of a section of cave in Fig. 40b

7.4 Example Application, Results and Discussions

To evaluate the computational accuracy of the DMOPD model three examples have been studied in this study. The first example is a simple 2D linear aquifer model consisting of a cave surrounded by porous media on either side of it. The second example is a slightly larger 2D aquifer consisting of more realistic caves embedded into a heterogeneous porous media, this example studies the transport of tracers being injected into the aquifer through injection wells. The third and the final example is the largest aquifer model studied in this study and it studies the transport of contaminants entering the area of interest from one corner of the aquifer, with the contaminants being produced at randomly located producer wells within the aquifer.

7.4.1 Example 1

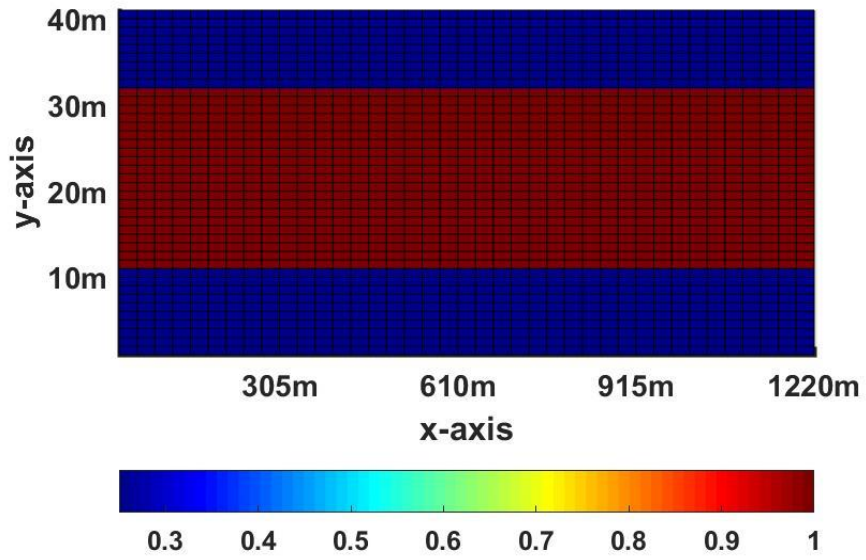
The first example studied in this paper consists of a simple two-dimensional linear aquifer (Fig. 41), consisting of a cave surrounded by porous media on either side of it. The aquifer dimensions are $1220m \times 41m \times 1.5m$ and it has been discretized into $40 \times 41 \times 1$ grids. The aquifer is being flooded with water carrying $30g / L$ of contaminant from the left boundary at a velocity of $3.26m/day$. The aquifer is closed at the top and bottom. The initial aquifer pressure was $1.38MPa$. The aquifer rock and fluid properties are listed on Table 1. In Fig. 41a, the region with 100% porosity (red portion in the middle) is the cave, and this section corresponds to Grids 11–31. This region is surrounded by a porous media whose porosity is 25% (blue portions).

Figure 41b, presents the division of the aquifer into different zones for the DMOPD model. The aquifer in this example has been divided into 10 separate zones on either side of the central zone. The central zone is assigned a very high permeability value, and an optimizer is used to estimate the permeability ratios of the other 10 zones.

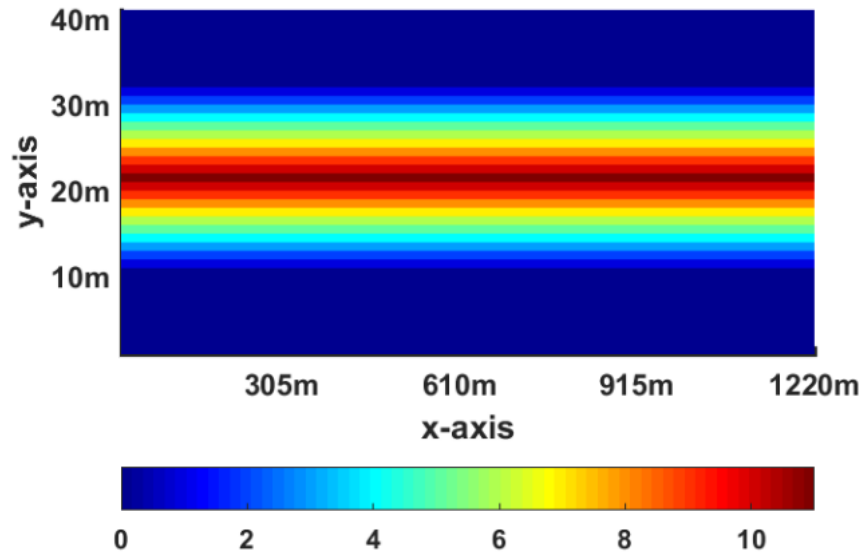
7.4.1.1 Trial using rough estimation of permeability ratios

To check the effectiveness of assigning permeability ratios to different zones a trial case was run where instead of optimizing the permeability ratios, they were assigned rough estimates. The results showed an improvement in comparison to using a Darcy's model with a single large value of permeability in the whole cave. The estimated permeability ratios are shown in Table 5. The permeability ratios are roughly estimated in such a manner that lower permeability ratios are used for the zones near the edges of the cave (closer to the porous media) and larger permeability ratios are used for zones near the center of the caves. This is done because the flow is faster in the center compared to the edges because of the viscous shear effects.

Figure 42 displays the concentration profiles obtained at the end of the simulation run using the three different models and it can be observed that the model with the rough permeability estimates showed a more parabolic profile which is comparable to the results obtained from the Brinkman's model. The Darcy's model provides a concentration profile with a flatter front.



a)



b)

Figure 41: Schematic of the aquifer used in Example 1: (a) full-field model (b) division of the caves into different zones

**Table 5: Rough estimated permeability ratios and the corresponding permeability values
for the 11 zones in Example 1**

Zones	Permeability Ratio	Permeability Value (md)
Zone 1	0.3	1.011×10^{12}
Zone 2	0.4	1.348×10^{12}
Zone 3	0.5	1.685×10^{12}
Zone 4	0.6	2.022×10^{12}
Zone 5	0.65	2.191×10^{12}
Zone 6	0.7	2.359×10^{12}
Zone 7	0.75	2.528×10^{12}
Zone 8	0.8	2.696×10^{12}
Zone 9	0.85	2.865×10^{12}
Zone 10	0.9	3.033×10^{12}
Zone 11 (Central Zone)	1	3.370×10^{12}

Figure 43, displays the velocity profiles obtained at the center of the aquifer from the three models and it can be seen here that the velocity profile obtained using the estimated permeability is closer to the parabolic shape obtained using the Brinkman's model.

The above results prove that estimating permeability ratios within the zones work and can be used to mimic the velocity profiles obtained using the Brinkman's model. The permeability ratios can be more accurately estimated using optimization techniques which is performed in the DMOPD model.

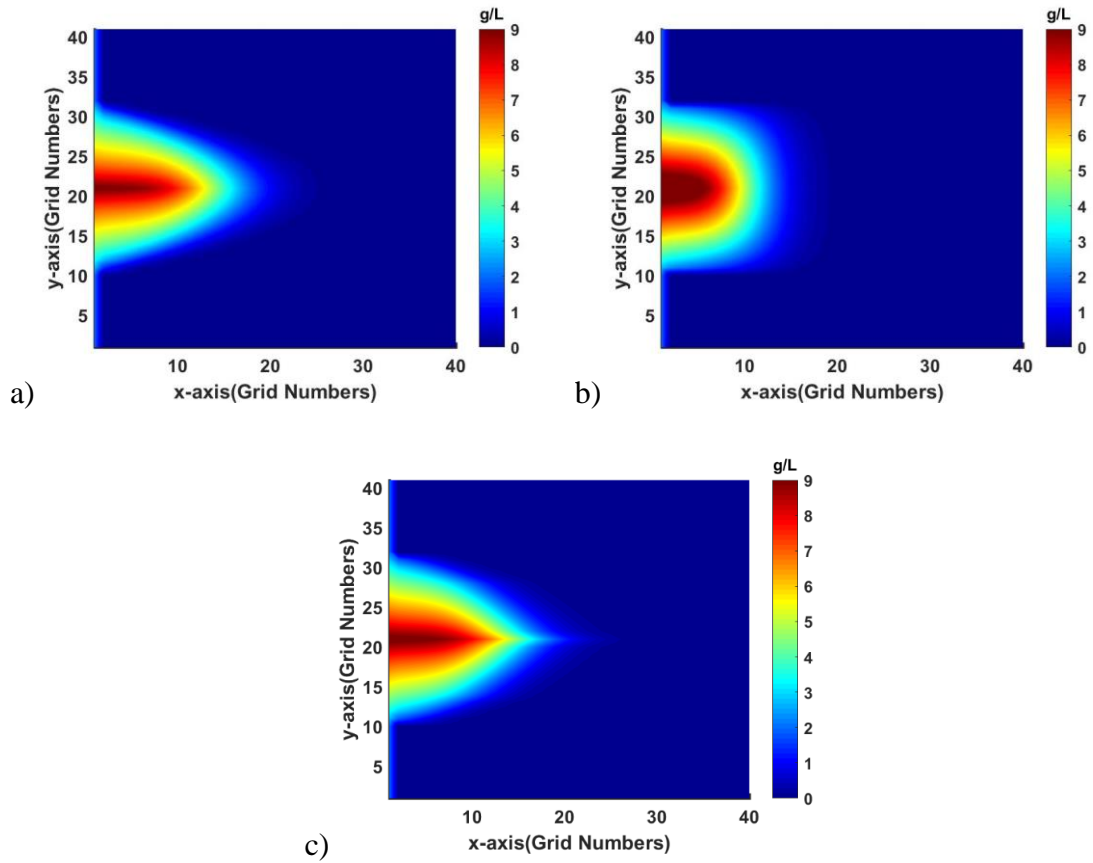


Figure 42: Concentration maps obtained from the three different models (a) Brinkman's model (b) Darcy's model (c) Rough Estimated permeability ratios in the 10 different

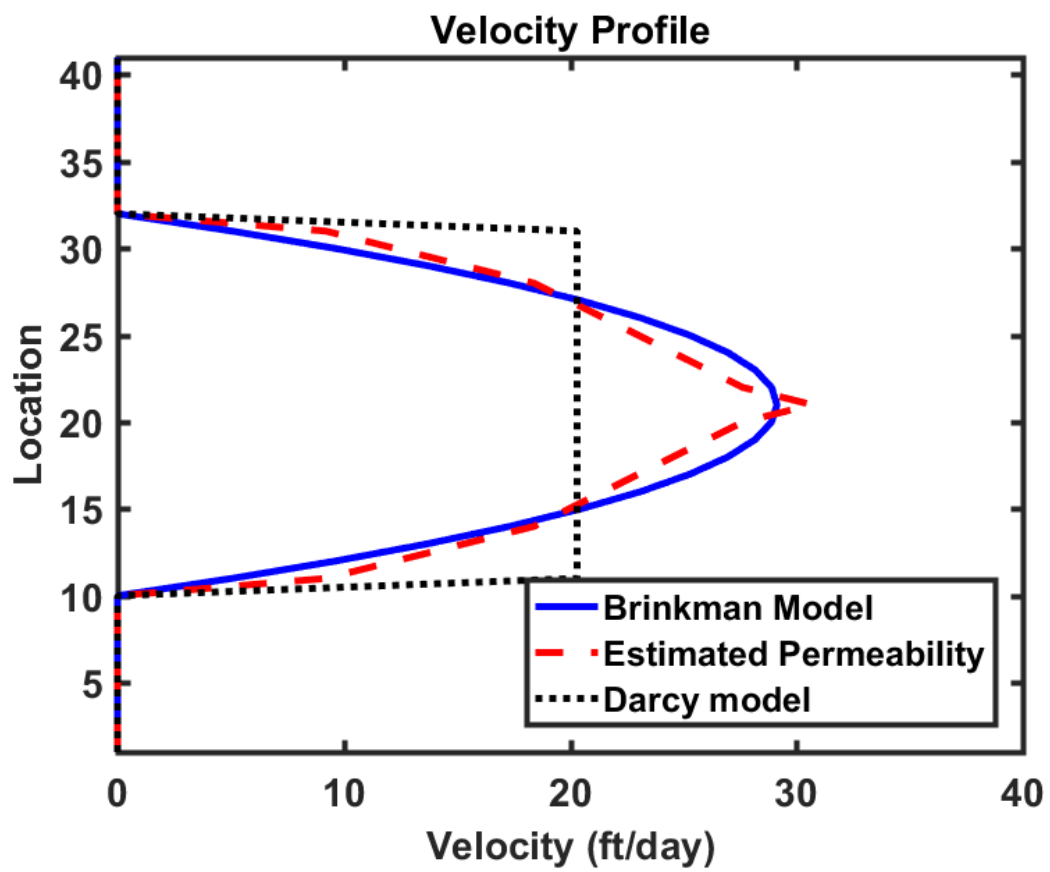


Figure 43: Velocity Profiles obtained using the three different modelling techniques

7.4.1.2 Actual run using the DMOPD model

The DMOPD model was run on aquifer of example 1 and the results obtained were compared to the results of the Brinkman's model and the Darcy's model. Differential Evolution algorithm was used to estimate the permeabilities by minimizing the objective function shown in Eq. 7.4. The upper and lower limits of permeability ratios to be optimized for each zone was fixed as 0.1 and 1 respectively. The optimization termination criteria was set as 1500 function evaluations. Figure 44 displays the minimization of the objective function. Table 6 lists the permeability ratios estimated at the end of the optimization cycle in the DMOPD model.

To evaluate the accuracy and performance of the DMOPD model, the Brinkman's model and the Darcy's model were solved as well. Figure 45 compares the velocity profiles obtained using the different techniques. It can be observed that the velocity profile generated by the DMOPD modelling technique produced a very good match with the velocity profiles generated from the Brinkman's model. The velocity profile generated by the Darcy's model did not give a good match in comparison to the other two techniques. Fig. 46 shows the contaminant concentration profile generated from the three models. The concentration profiles generated by the DMOPD is similar to the concentration profiles generated by the Brinkman's model. The Darcy's model on the other hand provides a poor match in comparison to the Brinkman's model.

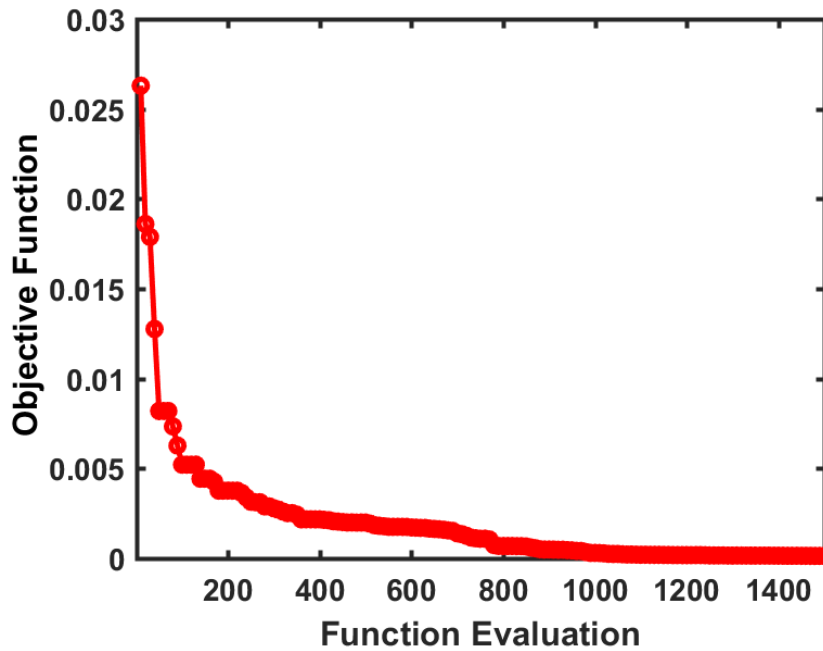


Figure 44: Graph showing the minimization of the objective function (Example 1)

Table 6: Optimized permeability ratios and the corresponding permeability values for the 11 zones in Example 1

Zones	Permeability Ratio	Permeability Value
Zone 1	0.172	0.580×10^{12}
Zone 2	0.331	1.115×10^{12}
Zone 3	0.470	1.584×10^{12}
Zone 4	0.596	2.009×10^{12}
Zone 5	0.703	2.369×10^{12}
Zone 6	0.795	2.679×10^{12}
Zone 7	0.866	2.918×10^{12}
Zone 8	0.926	3.121×10^{12}
Zone 9	0.967	3.235×10^{12}
Zone 10	0.996	3.357×10^{12}
Zone 11 (Central Zone)	1.000	3.370×10^{12}

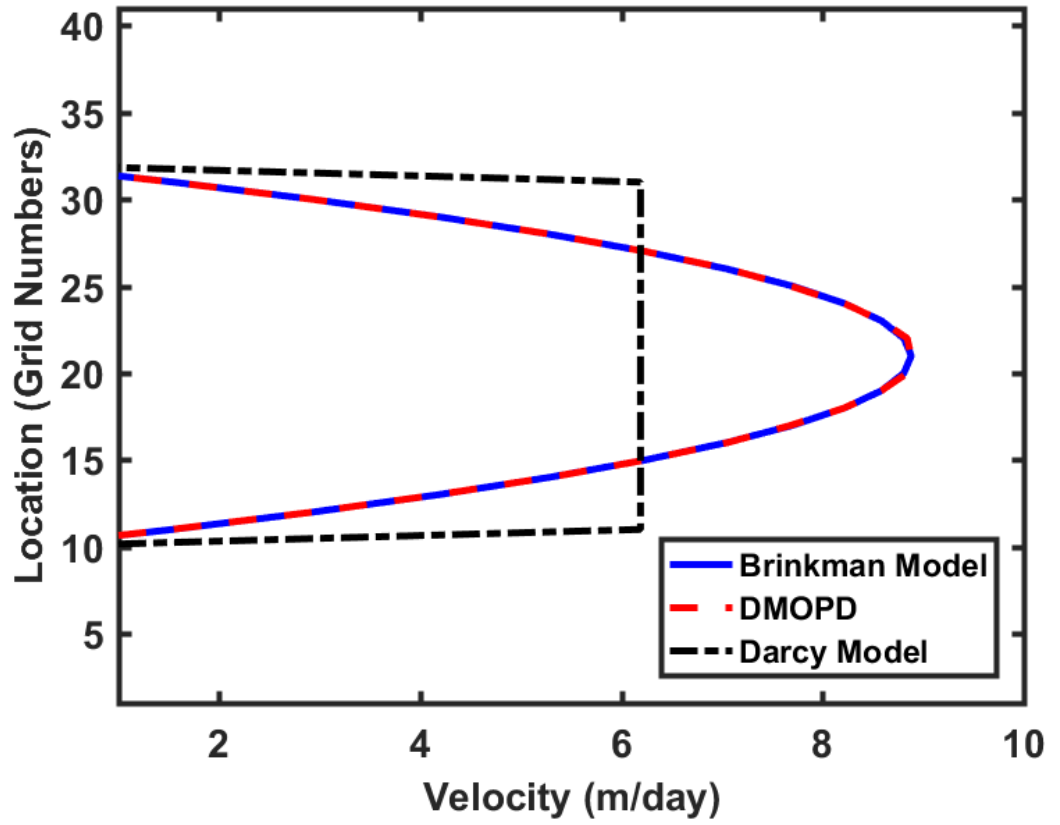
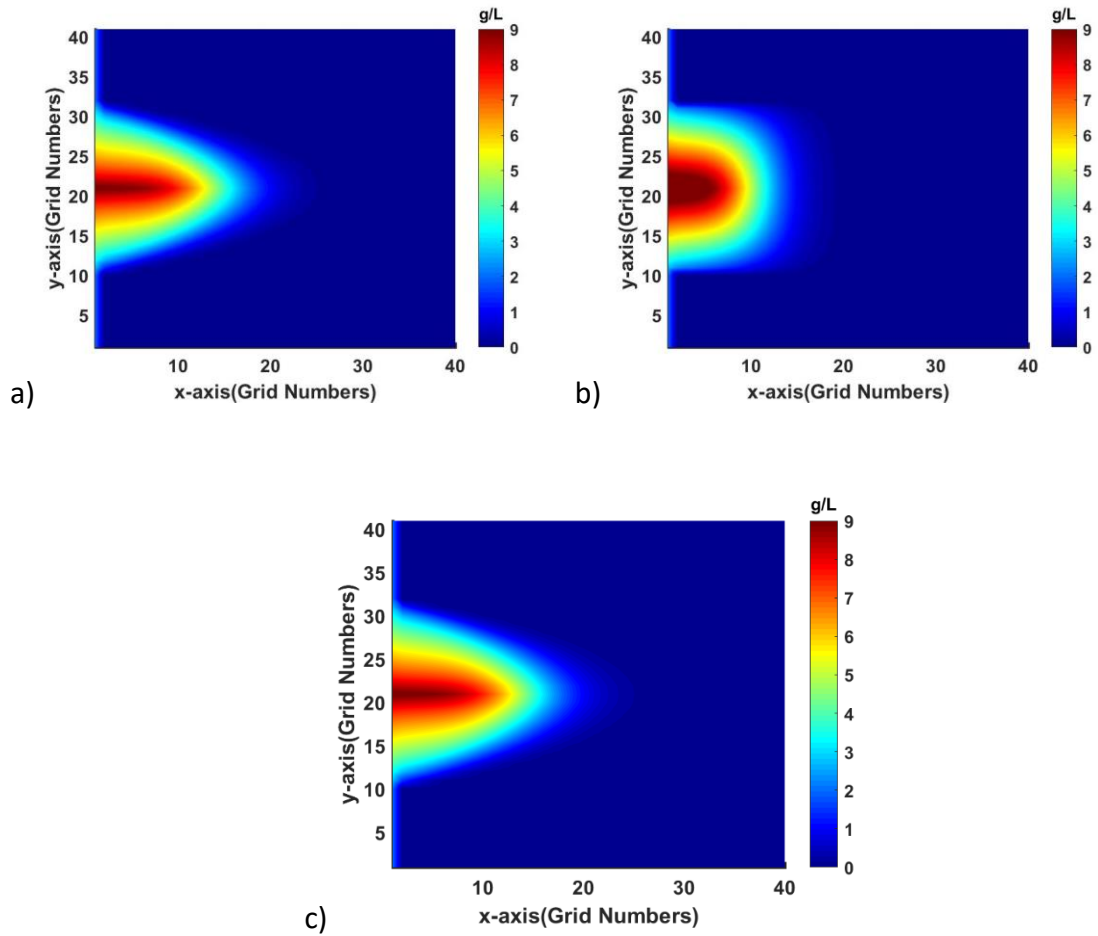


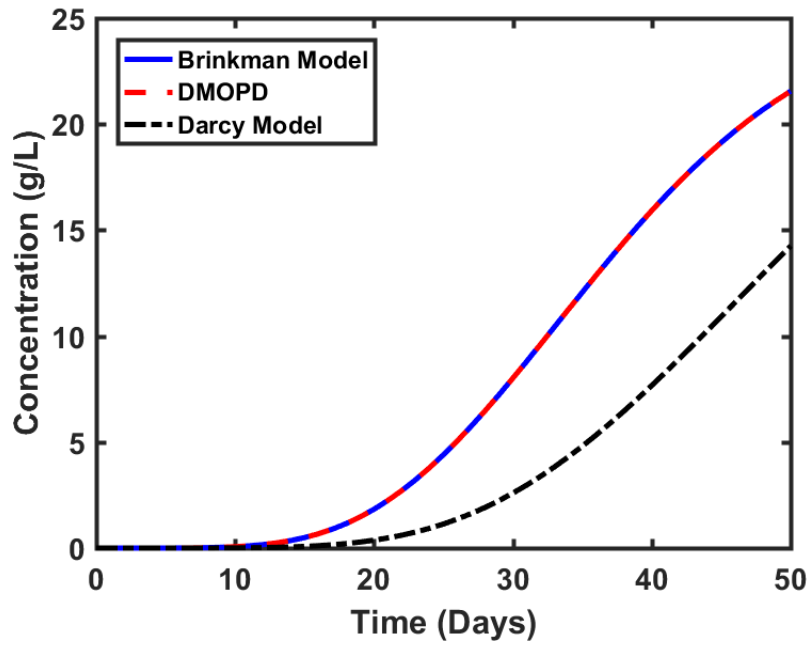
Figure 45: Velocity Profiles obtained using the three different modelling techniques



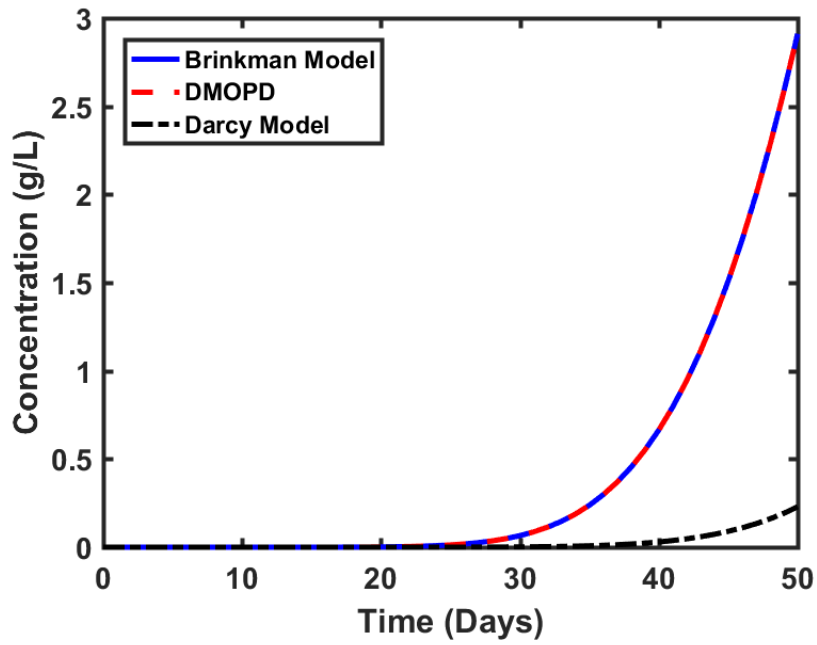
**Figure 46: Concentration maps from different modeling techniques (a) Brinkman's model
(b) Darcy's model (c) DMOPD model**

To further quantify the results the instantaneous contaminant concentration was observed at two different locations within the aquifer. The first observation station (Observation Station 1) is located in Grid (10,21), which is 305m from the inlet. The second observation station (Observation Station 2) is located in Grid (20,21), which is 610m from the inlet. It can be observed from Fig. 47 that the DMOPD model gave a very close match to the results obtained from the Brinkman's model. The Darcy's model however underestimated the contaminant concentration at the observed locations.

Table 7 shows the runtime taken by each model to solve the problems. The table also displays the ratios of the runtime taken to solve the problem by each of the approaches to the runtime taken to solve the problem using the Darcy's model. Darcy's method is the fastest amongst all the methods with a runtime of only 0.437 minutes and is almost 7.615 times faster than the Brinkman's model, but the problem with this model which has been earlier discussed is that it provides erroneous results. The DMOPD model takes 0.803 minutes to generate the results and is faster than the Brinkman's model. The interesting thing to notice for this case is the majority of time is being taken to estimate the permeability. The time taken to run the remaining timesteps is only 0.08 minutes, which is closer to Darcy's model. The number of unknowns when solving the Brinkman's model is 4839 compared to 1640 for solving the Darcy's model or the DMOPD model. For very large cases or cases which has more timesteps the DMOPD model can potentially provide even faster results. This would be further clarified and tested in the next two examples.



a)



b)

Figure 47: Instantaneous contaminant concentrations obtained from the different modeling techniques at (a) Observation Station 1 (b) Observation Station 2

Table 7: Comparison of the simulation run times (Example 1)

Model	Time Taken (min)		Time Ratio w.r.t. Darcy Model
Brinkman's Model	0.881		7.615
Darcy's Model	0.116		1
DMOPD	Time for Permeability Estimation: 0.723	0.803	6.92
	Time to run using the estimated Permeability: 0.08		

7.4.2 Example 2

The second example (Fig. 48) studied in this paper is a slightly larger model with the dimensions $304.8m \times 304.8m \times 7.62m$ ($1000ft \times 1000ft \times 25ft$) and has been discretized into $200 \times 200 \times 1$ grid blocks. This is a more realistic example consisting of geometrically complex caves embedded in a heterogeneous porous media. The rock and fluid properties used in this example is the same as those used in Example 1 and is given on Table 1. The aquifer is closed on all sides and the flow and transport of tracers within the model is due to five randomly placed injectors and six randomly placed producers. The injector wells are responsible for injecting a tracer at a concentration of $30g / L$. The porous region is heterogeneous and the permeability within this region is log-normally distributed with an average value of $3.95 \times 10^{-15} m^2$ ($40md$). There are 6 producers each producing at a rate of $63.59m^3/day$ ($\approx 400bbls/day$) and 5 injectors each injecting at a rate of

31.79m³/day (\approx 200bbls/day). The numerical simulation was run for 50 days using a time-step of 0.1 day.

Figures 49a and 49b show the division of the caves into three zones. Two above and below the central zone.

This case requires the estimation of only two permeability ratios. The upper and lower limits of permeability ratios to be optimized for each zone was fixed as 0.1 and 1 respectively. The optimization termination criteria was set as 400 function evaluations. Figure 50 shows the minimization of the objective function using the DE optimization algorithm. Table 8 lists the permeability ratios estimated and the corresponding permeability values of each zone.

The concentration profile obtained using the DMOPD model at the end of the simulation run after 50 days is shown in Fig. 51a. Figure 51b shows the quiver plot of the velocities in the aquifer. The quiver plot shows the velocity magnitude. The larger and more thicker the size of the arrows the larger the magnitude of velocity in the region. Note that the velocity is higher in the areas where the wells are located. It is evident from these figures that the tracer travels faster within the caves in comparison to the porous media. The transport in porous media is slower due to the lower permeability of porous media to flow and the adsorption of tracer on the surfaces of the rocks.

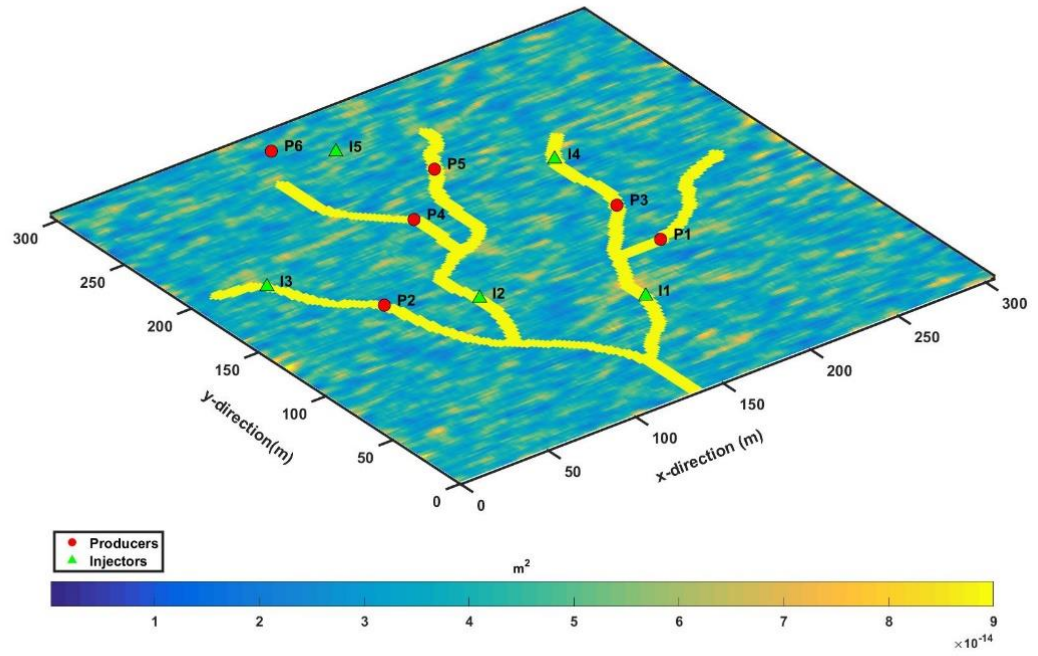


Figure 48: Aquifer model used in Example 2

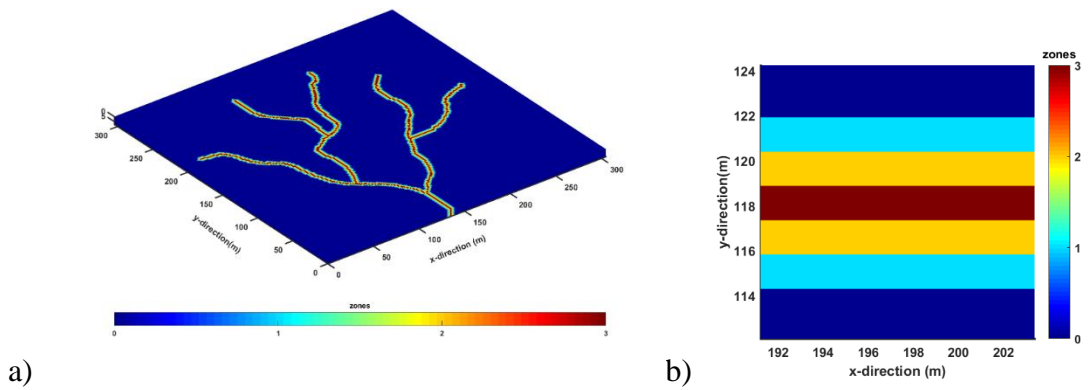


Figure 49: (a) Figure showing the division of the caves into three different zones (b) magnification of a section of the cave

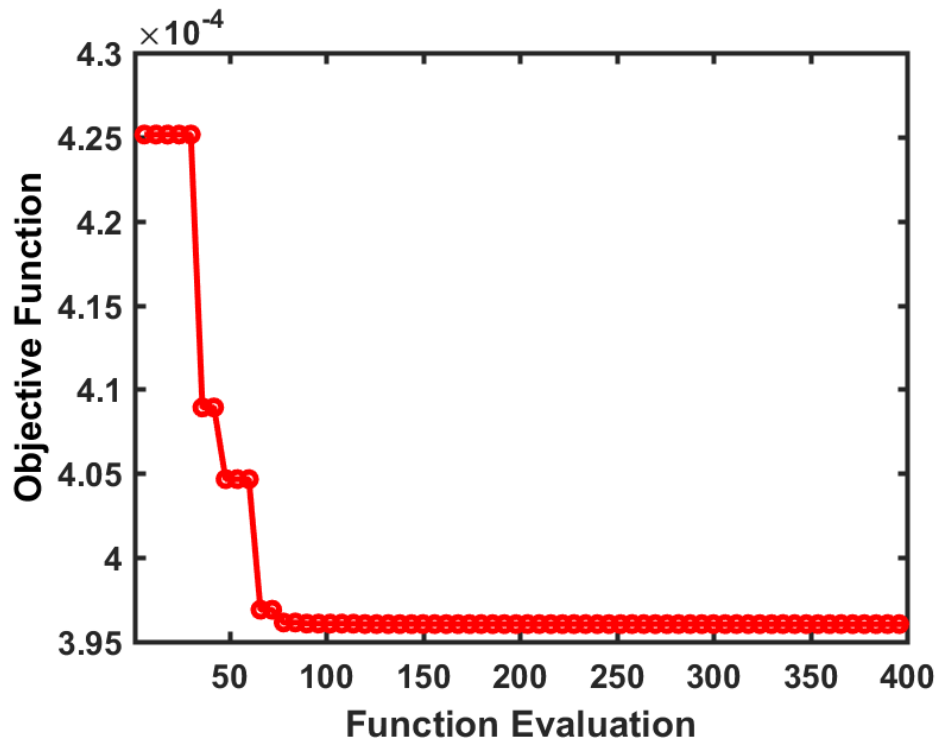


Figure 50: Graph showing the minimization of the objective function (Example 2)

Table 8: Optimized permeability ratios and the corresponding permeability values for the 3 zones in Example 2

Zones	Permeability Ratio	Permeability Value
Zone 1	0.485	1.091×10^{10}
Zone 2	0.863	1.942×10^{10}
Zone 3 (Central Zone)	1.000	2.250×10^{10}

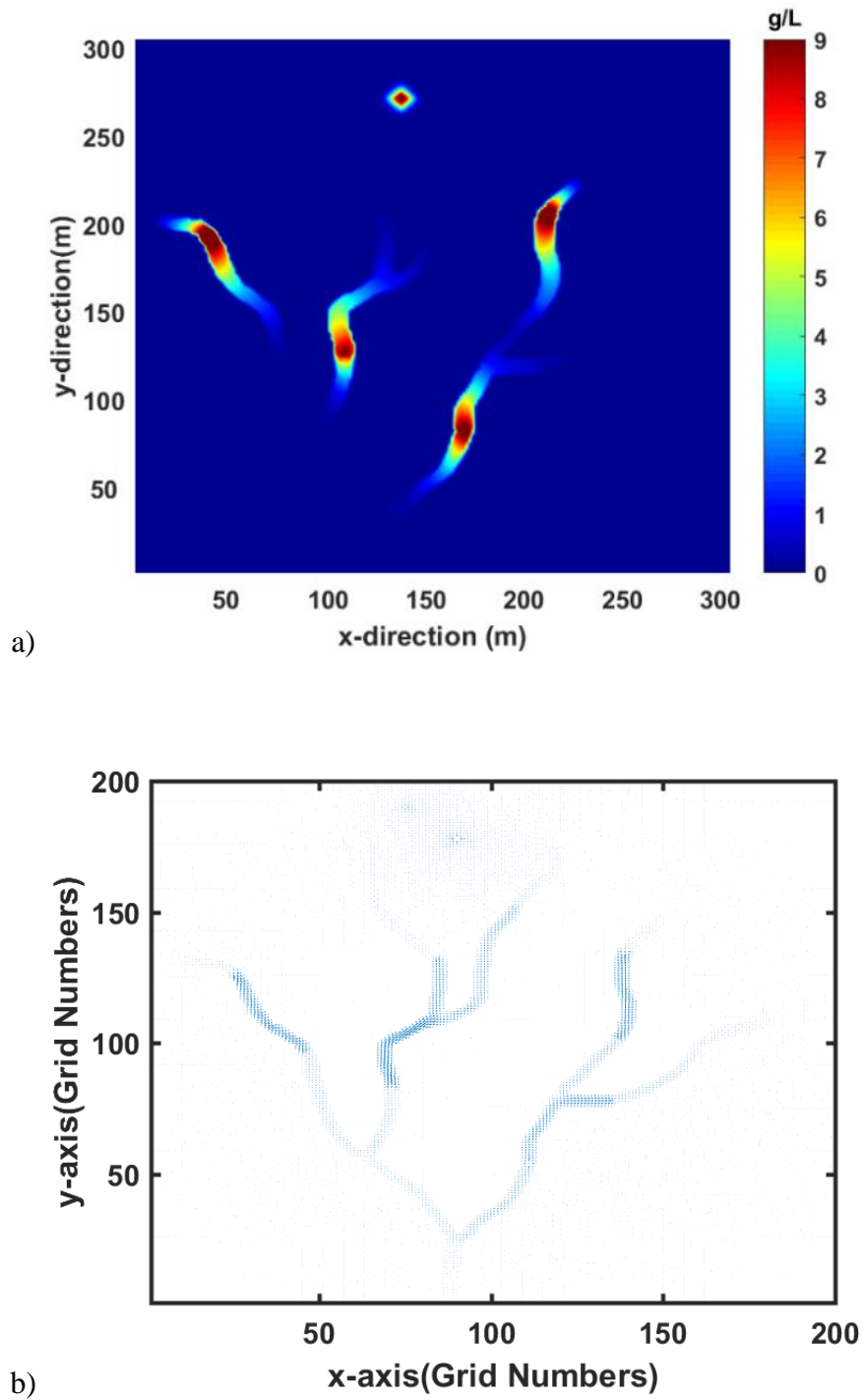


Figure 51: (a) Plot of concentration profile at the end of 50 days (b) quiver plot showing the velocity direction and magnitude within the aquifer

The instantaneous tracer concentration at the producers obtained from the DMOPD model were compared to the results obtained from the Brinkman's model and the Darcy's model (Fig. 52). All the producers are located in the caves except for P6 which is located in the porous region. It is evident from the results that the Darcy's model produced erroneous results as it underestimated the tracer concentration in the caves except for in the porous region where it gave similar results to the Brinkman's model. The DMOPD model provided a very good match with the Brinkman's model. Table 9 compares the runtime for each modelling technique and the ratio with respect to time taken to run Darcy model. The fastest of all techniques is the Darcy's model but it produces erroneous results. The DMOPD model gives very accurate results and is about 24 times faster than the Brinkman's model. Compared to Example 1 DMOPD model provided much faster results because of the increase in model size. The number of unknowns to be solved in DMOPD or Darcy's model is only 40000 compared to 119600 for the Brinkman's model.

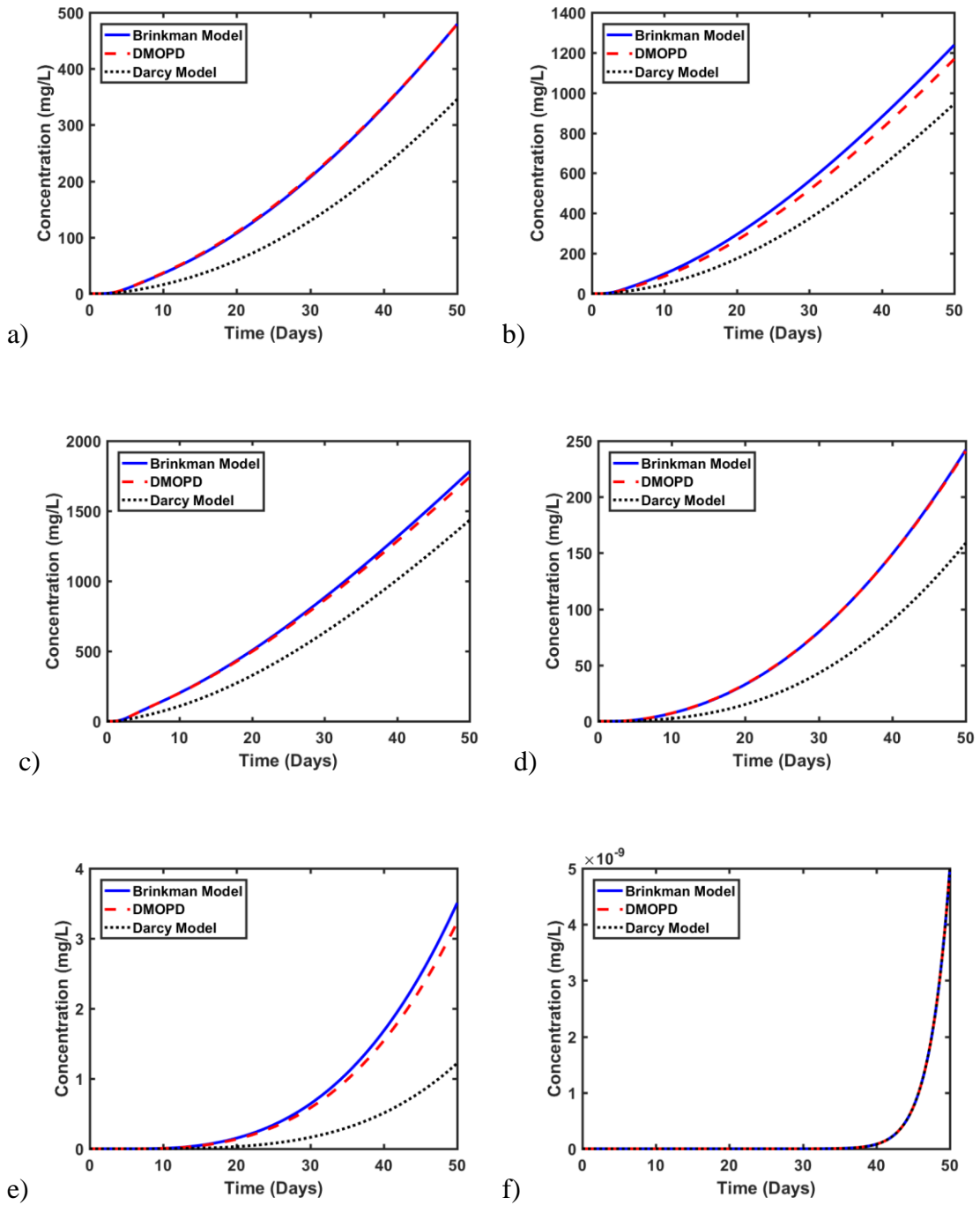


Figure 52: Instantaneous tracer concentration at different production wells (a)P1, (b)P2, (c)P3, (d)P4, (e)P5 and (f)P6

Table 9: Comparison of the simulation run times (Example 2)

Model	Time Taken (min)		Time Ratio w.r.t. Darcy Model
Brinkman's Model	917.021		27.887
Darcy's Model	32.884		1
DMOPD	Time for Permeability Estimation: 3.266	37.929	1.153
	Time to run using the estimated Permeability: 34.664		

7.4.3 Example 3

The third example (Fig. 53) is the largest model studied in this paper and has the dimensions $609.6m \times 609.6m \times 7.62m$ ($2000.ft \times 2000.ft \times 25.ft$) which has been discretized into $400 \times 400 \times 1$ grid blocks. Similar to the second example this aquifer model consists of geometrically complex cave structure embedded into a heterogeneous porous media. The aquifer model is closed on the top and right boundaries. The bottom and left boundaries are partially open such that contaminant laden water enters the aquifer from the bottom left corner of the aquifer at a velocity of $2.57m/day$. There are five randomly placed producers in the aquifer producing at the rate of $15.9m^3/day$ ($\approx 100bbls/day$). The rock and fluid properties are provided in Table 1. The simulation was run for 50 days while using a time-step of 0.1 days.

The aquifer has been divided into four different zones, with three zones on either side of the high permeability central zone (Fig 54 a & b).

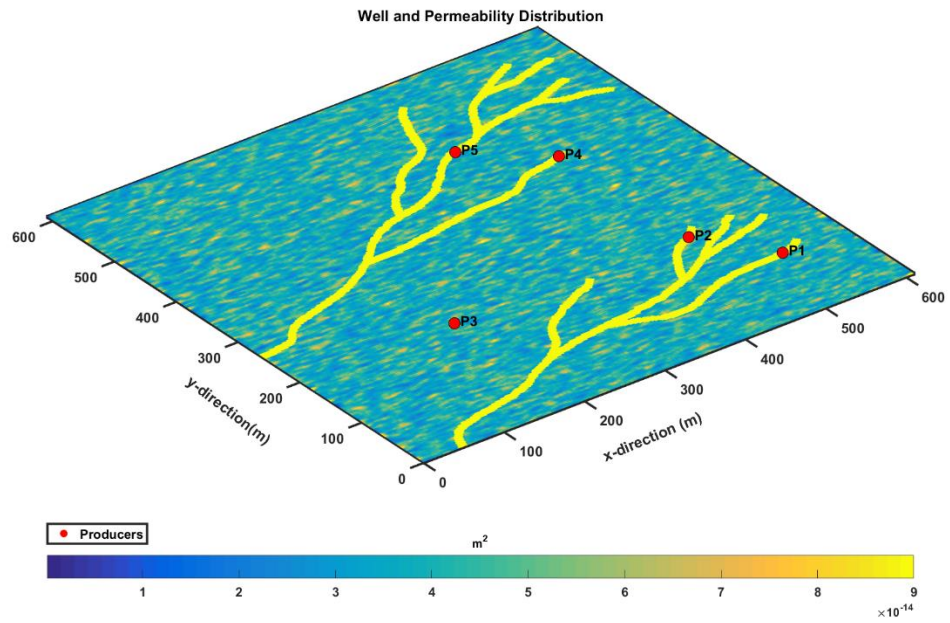


Figure 53: Aquifer model used in Example 3

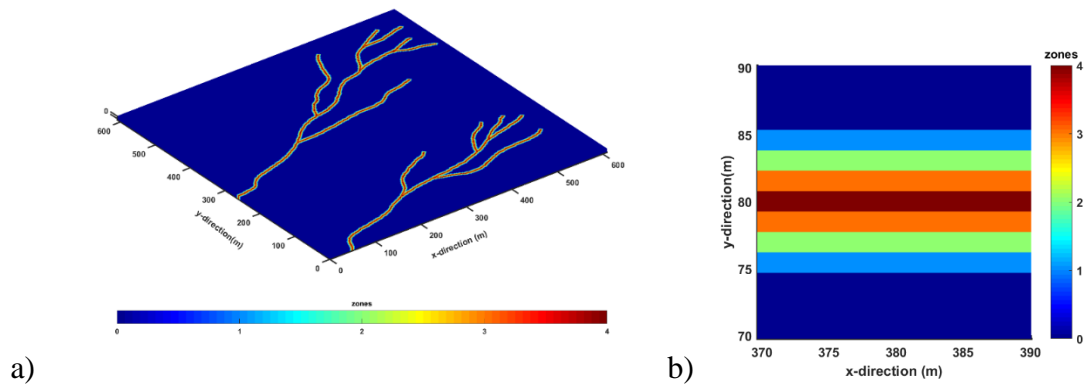


Figure 54: (a) Figure showing the division of the caves into four different zones (b) magnification of a section of the cave

This example required the estimation of permeability ratios in three different zones around the central layer. The minimization of the objective function is shown in Fig. 55. The upper and lower limits of permeability ratios to be optimized for each zone was fixed as 0.1 and 1 respectively. The optimization termination criteria was set as 400 function evaluations. Table 10 lists the estimated permeability ratio and the corresponding permeability values.

Figure 56a displays the contaminant distribution in the aquifer after 50 days. Figure 56b displays the quiver plot of velocities. The contaminant moves faster within the caves than it does in the porous media.

The instantaneous contaminant concentration at the producers obtained from the DMOPD model were compared to the results obtained from the Brinkman's model and the Darcy's model (Fig. 57). All the producers are located in the caves except for P3 which is located in the porous region. Similar to the previous example it can be noticed that the Darcy model

although the fastest, underestimates the contaminant concentration inside the caves. The DMOPD model gives very good match to the Brinkman's model and it is only 1.084 times slower than Darcy, and about 35.5 times faster than the Brinkman's model. The Brinkman's model was the slowest and took almost 13 days to complete 500 timesteps. Table 11 lists the time taken to complete 500 timesteps using each modelling technique.

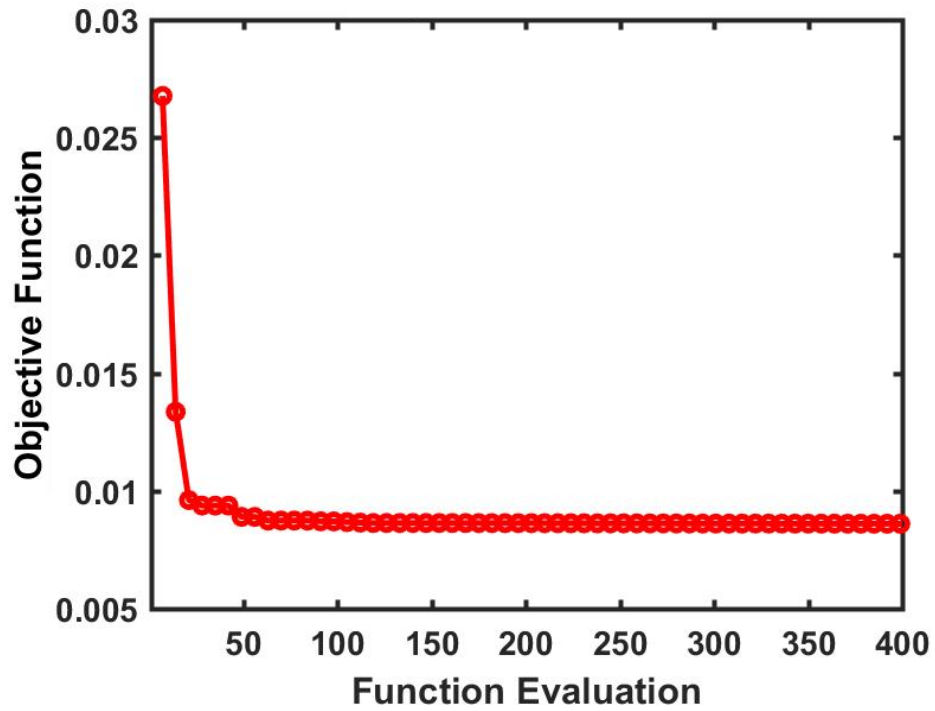


Figure 55: Graph showing the minimization of the objective function (Example 3)

Table 10: Optimized permeability ratios and the corresponding permeability values for the 4 zones in Example 3

Zones	Permeability Ratio	Permeability Value
Zone 1	0.361	0.812×10^9
Zone 2	0.699	1.573×10^9
Zone 3	0.913	2.054×10^9
Zone 4 (Central Zone)	1.000	2.250×10^9

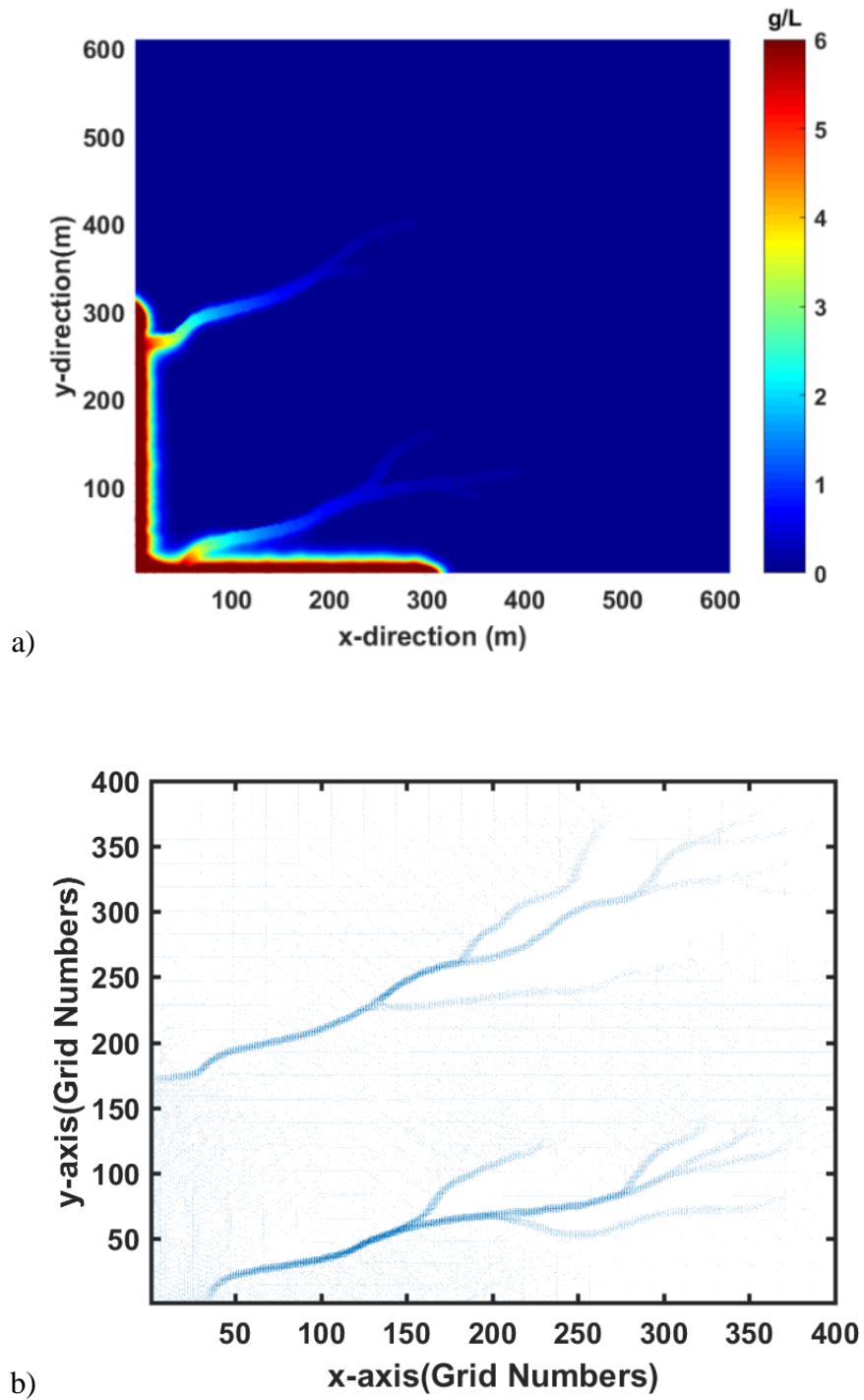


Figure 56: (a) Plot of concentration profile at the end of 50 days (b) quiver plot showing the velocity direction and magnitude within the aquifer

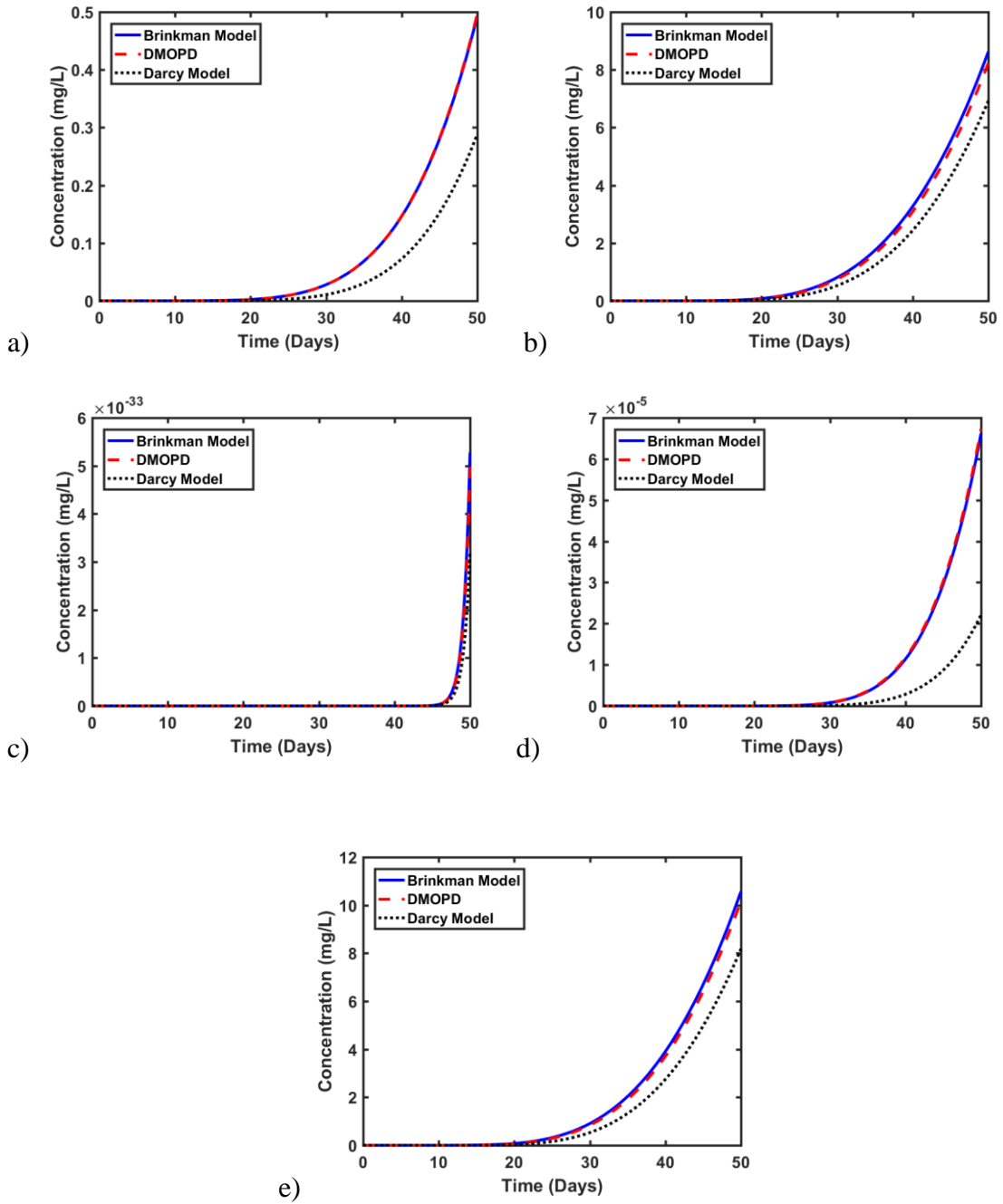


Figure 57: Instantaneous tracer concentration at different production wells after 50 days

(a)P1, (b)P2, (c)P3, (d)P4, and (e)P5

Table 11: Comparison of the simulation run times for first 500 timesteps (Example 3)

Model	Time Taken (min)		Time Ratio w.r.t. Darcy Model
Brinkman's Model	18605.836		38.522
Darcy's Model	482.992		1
DMOPD	Time for Permeability Estimation: 33.328	523.771	1.084
	Time to run using the estimated Permeability: 490.443		

7.5 Conclusion

A Darcy Model with Optimized Permeability Distribution (DMOPD) was proposed to model fluid transport in karst aquifers. This approach divides the free flowing regions (caves) into different zones and optimizes the permeability ratios in those zones to mimic the velocity profile obtained using the Brinkman’s model. The permeability ratio is the ratio of the permeability in that zone to the maximum permeability in the central zone. This method provides a good match to the solution obtained using the Brinkman’s model.

Three examples were presented to illustrate the effectiveness of the DMOPD model. The first example is a simple linear aquifer model consisting of only 1640 grids. The velocity profiles and the contaminant concentration obtained were an excellent match to the results obtained using the Brinkman’s model. The DMOPD model was 1.1 times faster than the Brinkman’s model. The second example is a larger and more complex heterogeneous aquifer consisting of 40000 grids. The results obtained here were also a good match to the

Brinkman's model and was found to be 24 times faster than the Brinkman's model. The final example is the largest model consisting of 160000 grids and the DMOPD model was found to be 35.5 times faster than the Brinkman's model. After looking at these cases it can be concluded that as the number of grids was increased the DMOPD modelling technique was more computationally effective in comparison to the Brinkman's model.

CHAPTER 8

MODELLING OF TWO PHASE FLOW IN KARST RESERVOIRS

8.1 Introduction

The rapid increase in the oil demand makes it a must to tackle complex reservoirs. The numerical modelling of carbonate karst reservoirs is considered to be one of the more challenging and attractable problems to be studied. Statistical studies revealed that 20%-30% of recoverable hydrocarbons are stored in unconformity surfaces (Flügel, 2004). Many oil reservoirs and water aquifers are related to paleokarst, such as Hainaut carbonate and sulphate karstic aquifer (Licour, 2014) , Raspo Mare reservoir (Gauchet and Corre, 1996; Bellentani *et al.*, 2016), gas reservoirs of Sinian (Zou, 2013), Yarqon-Tanimim aquifer (Dafny, Burg and Gvirtzman, 2010), Buda thermal karst system (Albert, Virág and Eröss, 2015) and Tahe oil reservoir in Tarim Basin in China (Peng *et al.*, 2009; Li, Hou and Ma, 2016). Keeping all these factors in mind it is important to come up with a numerical formulation which can model two phase flow in such reservoirs. Methods have been developed to estimate oil recovery factor in karst reservoirs consisting of cave systems by determination of connected caves from 3D maps using advanced workflows which integrate all sources of data: 3D seismic to production data (Montaron *et al.*, 2014).

One method to model two phase flow in karst reservoirs consisting of macroscopic structures such as caves is by using the Darcy-Stokes discontinuum model along with a

BJS boundary condition. A study was conducted on the Tahe oil reservoir where a streamline based Darcy-Stokes model was used to model flow of two phase slightly compressible fluids in karst reservoirs. The Navier Stokes equation for two phase was used in the caves and the two phase Darcy's equation was used in the porous media. Both the equations were coupled using the BJS boundary condition. The solution was compared to the Darcy's model in both the regions and it was found that Darcy-Stokes model provided a faster breakthrough at the producers when compared to the Darcy's model (Peng *et al.*, 2009).

Another method to model two phase flow through such fractured karst reservoirs is by using an effective permeability tensor obtained using the homogenization theory and the Darcy Stokes discontinuum model while using the BJS boundary condition. Once the tensor is obtained the next step is the calculation of the pseudo relative permeabilities using an analytical method. Once the permeability tensor and the the pseudo relative permeabilities are obtained, the simple elliptic formulation of the Darcy's model can be used to model flow within such reservoirs. This is a form of the EPM (effective porous media) method discussed in the literature review section of the manuscript. This study was conducted on the Tahe oil reservoir in western china (Huang, Yao and Wang, 2013).

In this chapter we have attempted to develop numerical formulations to model two phase flow in karst reservoirs using a modified Brinkman's model. We have also attempted to model two phase flow in karst reservoir using the DMOPD (Darcy Model with Optimized Permeability Distribution) model discussed in detail in the previous section. The only difference is that instead of using the elliptic model of the Darcy's equation we used the

decoupled model where the Darcy's equation is solved separately from the mass conservation equation. A finite volume approach is used to model two phase flow in karst reservoirs using the DMOPD model. A simple linear aquifer model consisting of a cave surrounded by porous media on either side is used to study the effect of two phase flow in karst reservoirs. The reservoir is initially at the initial water saturation and is being flooded by water from the left side of the aquifer.

8.2 Mathematical Models for Flow in Caves and Porous Media

8.2.1 Mathematical Equations for Two Phase Flow in Caves

A two phase Navier-Stokes equation can be used to model flow in the caves. The mass conservation equation for a two-phase immiscible laminar flow can be given by (Ishii and Hibiki, 2011)

$$\frac{\partial(\rho_{\theta}S_{\theta})}{\partial t} + \nabla(\rho_{\theta}\vec{v}_{\theta}S_{\theta}) = \frac{\rho_{\theta}q_{\theta}}{V_b}. \quad (8.1)$$

Where, θ denotes the phase, either oil or water in this case. The S_{θ} denotes the fraction of the area covered by the phase θ . The detailed derivation for Eq. 8.1 is as follows

$$\dot{m}_{in} - \dot{m}_{out} + \dot{m}_{source} = \dot{m}_{accumulation}. \quad (8.2)$$

Equation 8.2 shows the mass balance. Each of the terms is shown are shown in Eqs. 8.5, 8.7 and 8.8

$$\dot{m}_{in} - \dot{m}_{out} = \int_A (-\rho_{\theta} \bar{u}_{\theta}) \cdot \bar{n} dA_{\theta}, \quad (8.3)$$

Where, A_{θ} is the area occupied by the particular phase θ , it can be related to the total area of flow by Eq. 8.4

$$A_{\theta} = S_{\theta} A_b, \quad (8.4)$$

Where A_b is the total area available for flow

$$\dot{m}_{in} - \dot{m}_{out} = \int_A (-\rho_{\theta} \bar{u}_{\theta} S_{\theta}) \cdot \bar{n} dA_b, \quad (8.5)$$

$$\dot{m}_{accumulation} = \int_V \frac{\partial(\phi \rho_{\theta})}{\partial t} dV_{\theta}, \quad (8.6)$$

$$\dot{m}_{accumulation} = \int_V \frac{\partial(\phi \rho_{\theta} S_{\theta})}{\partial t} dV_b, \quad (8.7)$$

$$\dot{m}_{source} = \int_V \frac{\rho_{\theta} q_{\theta}}{V_b} dV_b. \quad (8.8)$$

Combining Eqs. 8.5, 8.7 and 8.8 and substituting them in Eq. 8.2 we get

$$\int_A (-\rho_\theta \bar{u}_\theta S_\theta) \cdot \bar{n} dA_b + \int_V \frac{\rho_\theta q_\theta}{V_b} dV_b = \int_V \frac{\partial(\phi \rho_\theta S_\theta)}{\partial t} dV_b. \quad (8.9)$$

Applying the Gauss Divergence Theorem on Eq. 8.9 we get

$$\int_V \nabla(-\rho_\theta \bar{u}_\theta S_\theta) dV_b + \int_V \frac{\rho_\theta q_\theta}{V_b} dV_b = \int_V \frac{\partial(\phi \rho_\theta S_\theta)}{\partial t} dV_b. \quad (8.10)$$

Removing the integral from Eq. 8.10 and rearranging it, we would obtain Eq. 8.1.

The momentum conservation equation for two phase flow or the Steady Flow Navier-Stokes equation for modelling flow in caves can be given by

$$S_\theta \nabla p_\theta - \nabla \bar{\tau}_\theta = 0, \quad (8.11)$$

Where , $\bar{\tau}_\theta$ is the deviatoric stress tensor for that particular phase. The deviatoric stress tensor for two phase flow can be given as follows.

$$\bar{\tau}_\theta = 2\mu_\theta S_\theta \left[\epsilon - \frac{1}{3}(\nabla \cdot \bar{v}_\theta) I \right]. \quad (8.12)$$

Where, μ is the viscosity of the fluid. ϵ can be given as follows

$$\epsilon = \frac{1}{2} \left[(\nabla \bar{v}_\theta) + (\nabla \bar{v}_\theta)^T \right]. \quad (8.13)$$

For an incompressible system Eq. 8.2 can be rewritten as

$$S_{\theta} \nabla p_{\theta} - \nabla \cdot \left[\mu_{\theta} S_{\theta} \left[(\nabla \vec{v}_{\theta}) + (\nabla \vec{v}_{\theta})^T \right] \right] = 0. \quad (8.14)$$

8.2.2 Mathematical Equations for Two Phase Flow in Porous Media

The mass conservation equation for two phase flow in porous media can be given by the following equation

$$\frac{\partial(\phi \rho_{\theta} S_{\theta})}{\partial t} + \nabla \cdot (\rho_{\theta} \vec{u}_{\theta}) = \frac{\rho_{\theta} q_{\theta}}{V_b} \quad (8.15)$$

Where ϕ is the porosity of the porous media

The momentum conservation equation or the transport equation is given by the Darcy's equation for two phase flow

$$\nabla p_{\theta} + \mu_{\theta} \overline{\overline{K}}^{-1} k_{r\theta} \vec{u}_{\theta} = 0, \quad (8.16)$$

Where $k_{r\theta}$ is the relative permeability of that phase

8.3 Modified Brinkman's Model for Two Phase Flow in Karst

Reservoirs

In this section we have attempted to modify the single phase Brinkman's equation in order to obtain a set of equations that would be able to solve the flow of two phase fluids in karst reservoirs.

8.3.1 Mathematical Equations

The mass conservation equations can be obtained by comparing Eqs. 8.1 and 8.15, and is as follows

$$\frac{\partial(\phi\rho_\theta S_\theta)}{\partial t} + \nabla(\rho_\theta \bar{u}_\theta S_\theta^\alpha) = \frac{\rho_\theta q_\theta}{V_b}, \quad (8.17)$$

Where,

$$\alpha = \begin{cases} 0, & \Omega = \Omega_p \\ 1, & \Omega = \Omega_c \end{cases}. \quad (8.18)$$

The momentum equation can be given by comparing Equations 8.14 and 8.16 and is given as follows

$$S_\theta^\alpha \nabla p_\theta - \nabla \cdot \left[\mu_{\theta eff} S_\theta \left[(\nabla \bar{v}) + (\nabla \bar{v})^T \right] \right] + \mu_\theta \bar{K}^{-1} k_{r\theta} \bar{u}_\theta = 0. \quad (8.19)$$

The significance of using the two-phase Brinkman's equation is that it can theoretically interpolate between the two-phase steady flow Navier-Stokes equation and the two-phase Darcy's equation by adjusting the values of \bar{K} , α and $\mu_{\theta eff}$.

8.3.2 Solution of the Two-Phase Modified Brinkman's Equation

Equation 8.17 gives two mass conservation equations for each phase. These equations are as follows:

For Oil,

$$\frac{\partial(\phi\rho_o S_o)}{\partial t} + \nabla(\rho_o \bar{u}_o S_o^\alpha) = \frac{\rho_o q_o}{V_b}, \quad (8.20)$$

For Water,

$$\frac{\partial(\phi\rho_w S_w)}{\partial t} + \nabla(\rho_w \bar{u}_w S_w^\alpha) = \frac{\rho_w q_w}{V_b}, \quad (8.21)$$

The formation volume factor of the fluid is given by $B_w = \rho_{wsc}/\rho_w$, and $B_o = \rho_{osc}/\rho_o$, where, ρ_{osc} and ρ_{wsc} are the fluid densities at standard conditions. The inverse of the formation volume factors are given by $b_o = 1/B_o$, and $b_w = 1/B_w$. Equations 8.20 and 8.21 can be rewritten as

For Oil,

$$\frac{\partial(\phi b_o S_o)}{\partial t} + \nabla(b_o \bar{u}_o S_o^\alpha) = \frac{b_o q_o}{V_b}, \quad (8.22)$$

For Water,

$$\frac{\partial(\phi b_w S_w)}{\partial t} + \nabla(b_w \bar{u}_w S_w^\alpha) = \frac{b_w q_w}{V_b}, \quad (8.23)$$

Equation 8.19 is in a vectoral form and provides two equations (momentum equations in

the x and y direction) per phase. Giving a total of four equations. They are as follows:

For Oil,

$$S_o^\alpha \frac{\partial p_o}{\partial x} - 2 \frac{\partial}{\partial x} \left(\mu_{o\text{eff}} S_o \frac{\partial u_{ox}}{\partial x} \right) - \frac{\partial}{\partial y} \left[\mu_{o\text{eff}} S_o \left(\frac{\partial u_{ox}}{\partial y} + \frac{\partial u_{oy}}{\partial x} \right) \right] + \frac{\mu_o}{K_x K_{ro}} u_{ox} = 0. \quad (8.24)$$

$$S_o^\alpha \frac{\partial p_o}{\partial y} - 2 \frac{\partial}{\partial y} \left(\mu_{o\text{eff}} S_o \frac{\partial u_{oy}}{\partial y} \right) - \frac{\partial}{\partial x} \left[\mu_{o\text{eff}} S_o \left(\frac{\partial u_{ox}}{\partial y} + \frac{\partial u_{oy}}{\partial x} \right) \right] + \frac{\mu_o}{K_y K_{ro}} u_{oy} = 0. \quad (8.25)$$

For Water,

$$S_w^\alpha \frac{\partial p_w}{\partial x} - 2 \frac{\partial}{\partial x} \left(\mu_{w\text{eff}} S_w \frac{\partial u_{wx}}{\partial x} \right) - \frac{\partial}{\partial y} \left[\mu_{w\text{eff}} S_w \left(\frac{\partial u_{wx}}{\partial y} + \frac{\partial u_{wy}}{\partial x} \right) \right] + \frac{\mu_w}{K_x K_{rw}} u_{wx} = 0. \quad (8.26)$$

$$S_w^\alpha \frac{\partial p_w}{\partial y} - 2 \frac{\partial}{\partial y} \left(\mu_{w\text{eff}} S_w \frac{\partial u_{wy}}{\partial y} \right) - \frac{\partial}{\partial x} \left[\mu_{w\text{eff}} S_w \left(\frac{\partial u_{wx}}{\partial y} + \frac{\partial u_{wy}}{\partial x} \right) \right] + \frac{\mu_w}{K_y K_{rw}} u_{wy} = 0. \quad (8.27)$$

The equations 8.22 – 8.27 are solved along with some closure equations. The closure equations are as follows:

$$\sum S_\theta = 1, \quad (8.28)$$

$$p_c = p_o - p_w, \quad (8.29)$$

Where, p_c , is the capillary pressure which is the difference in pressure across the interface between two phases. In this research we assume zero capillary pressure. Therefore,

$$p_o = p_w = p, \quad (8.30)$$

8.3.2 Discretization of the Two-Phase Modified Brinkman's Equation

While discretizing the equations of flow, the perturbation is done such that the pressures are at the center of the grid blocks while the velocities are at the grid interfaces. The system of equations to be solved are non-linear. The primary unknowns are the pressure (p), water saturation (S_w), velocity of oil in x-direction (u_{ox}), velocity of water in x-direction (u_{wx}), velocity of oil in y-direction (u_{oy}), and velocity of water in y-direction (u_{wy}). Because of the non-linearity of the problem, the discretized equations are written as residual functions and the Newton-Raphson method for solving nonlinear simultaneous equations is used to solve the problem.

The discretization for the conservation of mass for each phase (Eq. 8.22 & Eq. 8.23) in two-dimensions is given by

$$\begin{aligned} R_{MCO}^{\gamma+1} = & \frac{\phi b_o^{\gamma+1}}{\Delta t} (1 - S_{w_{h,j}}^{\gamma+1}) + \frac{\left(1 - S_w^{\gamma+1}\right)_{h+\frac{1}{2},j}^{\alpha} b_o^{\gamma+1}}{\Delta x} u_{ox_{h+\frac{1}{2},j}}^{\gamma+1} - \frac{\left(1 - S_w^{\gamma+1}\right)_{h-\frac{1}{2},j}^{\alpha} b_o^{\gamma+1}}{\Delta x} u_{ox_{h-\frac{1}{2},j}}^{\gamma+1} \\ & + \frac{\left(1 - S_w^{\gamma+1}\right)_{h,j+\frac{1}{2}}^{\alpha} b_o^{\gamma+1}}{\Delta y} u_{oy_{h,j+\frac{1}{2}}}^{\gamma+1} - \frac{\left(1 - S_w^{\gamma+1}\right)_{h,j-\frac{1}{2}}^{\alpha} b_o^{\gamma+1}}{\Delta y} u_{oy_{h,j-\frac{1}{2}}}^{\gamma+1} - \frac{b_o q_{osc}}{V_b} - \frac{\phi b_o^n}{\Delta t} (1 - S_{w_{h,j}}^n) \end{aligned} \quad (8.31)$$

$$\begin{aligned}
R_{MCW}^{\gamma+1} = & \frac{\phi b_w^{\gamma+1}}{\Delta t} S_{w_{h,i}}^{\gamma+1} + \frac{S_w^{\alpha^{\gamma+1}} b_w^{\gamma+1}}{\Delta x} u_{wx_{h+\frac{1}{2},j}}^{\gamma+1} - \frac{S_w^{\alpha^{\gamma+1}} b_w^{\gamma+1}}{\Delta x} u_{wx_{h-\frac{1}{2},j}}^{\gamma+1} \\
& + \frac{S_w^{\alpha^{\gamma+1}} b_w^{\gamma+1}}{\Delta y} u_{wy_{h,i+\frac{1}{2}}}^{\gamma+1} - \frac{S_w^{\alpha^{\gamma+1}} b_w^{\gamma+1}}{\Delta y} u_{wy_{h,i-\frac{1}{2}}}^{\gamma+1} - \frac{b_w q_{wsc}}{V_b} - \frac{\phi b_w^n}{\Delta t} S_{w_{h,i}}^n
\end{aligned} \tag{8.32}$$

Where, the values of saturation at the grid boundaries are evaluated using the upwinding technique, For example:

$$\left(1 - S_{w_{h+\frac{1}{2},j}}^{\gamma+1} \right) = \begin{cases} \left(1 - S_{w_{h,i}}^{\gamma+1} \right) & \text{if } u_{ox_{h+\frac{1}{2},j}}^{\gamma+1} > 0 \\ \left(1 - S_{w_{h+1,j}}^{\alpha^{\gamma+1}} \right) & \text{if } u_{ox_{h+\frac{1}{2},j}}^{\gamma+1} < 0 \end{cases} \tag{8.33}$$

$$S_{w_{h+\frac{1}{2},j}}^{\alpha^{\gamma+1}} = \begin{cases} S_{w_{h,i}}^{\alpha^{\gamma+1}} & \text{if } u_{wx_{h+\frac{1}{2},j}}^{\gamma+1} > 0 \\ S_{w_{h+1,j}}^{\alpha^{\gamma+1}} & \text{if } u_{wx_{h+\frac{1}{2},j}}^{\gamma+1} < 0 \end{cases} \tag{8.34}$$

where h and i are the indices of the grid blocks in the x and y -directions, the superscript γ is the iteration index, while the superscript n is the index of time. $R_{MCO}^{\gamma+1}$, is the residual function for the conservation of mass of oil phase, and $R_{MCW}^{\gamma+1}$, is the residual function for the conservation of mass of water phase.

The discretization for Eq. 8.24 is as follows:

$$\begin{aligned}
R_{Mu_{ox}}^{\gamma+1} = & \frac{\left(1 - S_w^{\gamma+1}\right)_{h+\frac{1}{2},i}^{\alpha}}{\Delta x} p_{h+1,i}^{\gamma+1} - \frac{\left(1 - S_w^{\gamma+1}\right)_{h+\frac{1}{2},i}^{\alpha}}{\Delta x} p_{h,i}^{\gamma+1} \\
& - \frac{2}{\Delta x^2} \left[\mu_{o\text{eff}}(1 - S_w)\right]_{h+1,i}^{\gamma+1} u_{ox_{h+\frac{3}{2},i}}^{\gamma+1} - \frac{2}{\Delta x^2} \left[\mu_{o\text{eff}}(1 - S_w)\right]_{h,i}^{\gamma+1} u_{ox_{h-\frac{1}{2},i}}^{\gamma+1} \\
& - \frac{1}{\Delta y^2} \left[\mu_{o\text{eff}}(1 - S_w)\right]_{h+\frac{1}{2},i+\frac{1}{2}}^{\gamma+1} u_{ox_{h+\frac{1}{2},i+1}}^{\gamma+1} - \frac{1}{\Delta y^2} \left[\mu_{o\text{eff}}(1 - S_w)\right]_{h+\frac{1}{2},i-\frac{1}{2}}^{\gamma+1} u_{ox_{h+\frac{1}{2},i-1}}^{\gamma+1} \\
& + \left[\begin{aligned} & \frac{2}{\Delta x^2} \left[\mu_{o\text{eff}}(1 - S_w)\right]_{h+1,i}^{\gamma+1} + \frac{2}{\Delta x^2} \left[\mu_{o\text{eff}}(1 - S_w)\right]_{h,i}^{\gamma+1} \\ & + \frac{1}{\Delta y^2} \left[\mu_{o\text{eff}}(1 - S_w)\right]_{h+\frac{1}{2},i+\frac{1}{2}}^{\gamma+1} + \frac{1}{\Delta y^2} \left[\mu_{o\text{eff}}(1 - S_w)\right]_{h+\frac{1}{2},i-\frac{1}{2}}^{\gamma+1} \end{aligned} \right] u_{ox_{h+\frac{1}{2},i}}^{\gamma+1} \\
& + \frac{\mu_{o_{h+\frac{1}{2},i}}^{\gamma+1}}{K_x k_{ro_{h+\frac{1}{2},i}}^{\gamma+1}} \\
& - \frac{1}{\Delta x \Delta y} \left[\mu_{o\text{eff}}(1 - S_w)\right]_{h+\frac{1}{2},i+\frac{1}{2}}^{\gamma+1} u_{oy_{h+1,i+\frac{1}{2}}}^{\gamma+1} + \frac{1}{\Delta x \Delta y} \left[\mu_{o\text{eff}}(1 - S_w)\right]_{h+\frac{1}{2},i+\frac{1}{2}}^{\gamma+1} u_{oy_{h,i+\frac{1}{2}}}^{\gamma+1} \\
& + \frac{1}{\Delta x \Delta y} \left[\mu_{o\text{eff}}(1 - S_w)\right]_{h+\frac{1}{2},i-\frac{1}{2}}^{\gamma+1} u_{oy_{h+1,i-\frac{1}{2}}}^{\gamma+1} - \frac{1}{\Delta x \Delta y} \left[\mu_{o\text{eff}}(1 - S_w)\right]_{h+\frac{1}{2},i-\frac{1}{2}}^{\gamma+1} u_{oy_{h,i-\frac{1}{2}}}^{\gamma+1}
\end{aligned} \tag{8.35}$$

$R_{Mu_{ox}}^{\gamma+1}$ is the residual for the oil velocity in the x-direction

The discretization for Eq. 8.25 is as follows:

$$\begin{aligned}
R_{Mu_{oy}}^{\gamma+1} &= \frac{\left(1 - S_w^{\gamma+1}\right)_{h,i+\frac{1}{2}}^\alpha}{\Delta y} p_{h,i+1}^{\gamma+1} - \frac{\left(1 - S_w^{\gamma+1}\right)_{h,i+\frac{1}{2}}^\alpha}{\Delta y} p_{h,i}^{\gamma+1} \\
&\quad - \frac{2}{\Delta y^2} \left[\mu_{oeff} (1 - S_w)\right]_{h,i+1}^{\gamma+1} u_{oy}^{\gamma+1}{}_{h,i+\frac{3}{2}} - \frac{2}{\Delta y^2} \left[\mu_{oeff} (1 - S_w)\right]_{h,i}^{\gamma+1} u_{oy}^{\gamma+1}{}_{h,i-\frac{1}{2}} \\
&\quad - \frac{1}{\Delta x^2} \left[\mu_{oeff} (1 - S_w)\right]_{h+\frac{1}{2},i+\frac{1}{2}}^{\gamma+1} u_{oy}^{\gamma+1}{}_{h+i+\frac{1}{2}} - \frac{1}{\Delta x^2} \left[\mu_{oeff} (1 - S_w)\right]_{h-\frac{1}{2},i+\frac{1}{2}}^{\gamma+1} u_{oy}^{\gamma+1}{}_{h-1,i+\frac{1}{2}} \\
&\quad + \left[\begin{aligned} &\frac{2}{\Delta y^2} \left[\mu_{oeff} (1 - S_w)\right]_{h,i+1}^{\gamma+1} + \frac{2}{\Delta y^2} \left[\mu_{oeff} (1 - S_w)\right]_{h,i}^{\gamma+1} \\ &+ \frac{1}{\Delta x^2} \left[\mu_{oeff} (1 - S_w)\right]_{h+\frac{1}{2},i+\frac{1}{2}}^{\gamma+1} + \frac{1}{\Delta x^2} \left[\mu_{oeff} (1 - S_w)\right]_{h-\frac{1}{2},i+\frac{1}{2}}^{\gamma+1} \end{aligned} \right] u_{oy}^{\gamma+1}{}_{h,i+\frac{1}{2}} \\
&\quad + \frac{\mu_o^{\gamma+1}}{K_y k_{ro}^{\gamma+1}}{}_{h,i+\frac{1}{2}} \\
&\quad - \frac{1}{\Delta x \Delta y} \left[\mu_{oeff} (1 - S_w)\right]_{h+\frac{1}{2},i+\frac{1}{2}}^{\gamma+1} u_{ox}^{\gamma+1}{}_{h+\frac{1}{2},i+1} + \frac{1}{\Delta x \Delta y} \left[\mu_{oeff} (1 - S_w)\right]_{h+\frac{1}{2},i+\frac{1}{2}}^{\gamma+1} u_{ox}^{\gamma+1}{}_{h+\frac{1}{2},i} \\
&\quad + \frac{1}{\Delta x \Delta y} \left[\mu_{oeff} (1 - S_w)\right]_{h-\frac{1}{2},i+\frac{1}{2}}^{\gamma+1} u_{ox}^{\gamma+1}{}_{h-\frac{1}{2},i+1} - \frac{1}{\Delta x \Delta y} \left[\mu_{oeff} (1 - S_w)\right]_{h-\frac{1}{2},i+\frac{1}{2}}^{\gamma+1} u_{ox}^{\gamma+1}{}_{h-\frac{1}{2},i}
\end{aligned} \tag{8.36}$$

$R_{Mu_{oy}}^{\gamma+1}$ is the residual for the oil velocity in the y-direction

The discretization for Eq. 8.26 is as follows:

$$\begin{aligned}
R_{Mu_{wx}}^{\gamma+1} &= \frac{S_w^{\alpha^{\gamma+1}}}{\Delta x} P_{h+1,i}^{\gamma+1} - \frac{S_w^{\alpha^{\gamma+1}}}{\Delta x} P_{h,i}^{\gamma+1} \\
&\quad - \frac{2}{\Delta x^2} [\mu_{weff} S_w]_{h+1,i}^{\gamma+1} u_{wx, \frac{3}{2}}^{\gamma+1} - \frac{2}{\Delta x^2} [\mu_{weff} S_w]_{h,i}^{\gamma+1} u_{wx, \frac{1}{2}}^{\gamma+1} \\
&\quad - \frac{1}{\Delta y^2} [\mu_{weff} S_w]_{h+\frac{1}{2}, i+\frac{1}{2}}^{\gamma+1} u_{wx, \frac{1}{2}}^{\gamma+1} - \frac{1}{\Delta y^2} [\mu_{weff} S_w]_{h+\frac{1}{2}, i-\frac{1}{2}}^{\gamma+1} u_{wx, \frac{1}{2}}^{\gamma+1} \\
&\quad + \left[\begin{aligned} &\frac{2}{\Delta x^2} [\mu_{weff} S_w]_{h+1,i}^{\gamma+1} + \frac{2}{\Delta x^2} [\mu_{weff} S_w]_{h,i}^{\gamma+1} \\ &+ \frac{1}{\Delta y^2} [\mu_{weff} S_w]_{h+\frac{1}{2}, i+\frac{1}{2}}^{\gamma+1} + \frac{1}{\Delta y^2} [\mu_{weff} S_w]_{h+\frac{1}{2}, i-\frac{1}{2}}^{\gamma+1} \end{aligned} \right] u_{wx, \frac{1}{2}}^{\gamma+1} \\
&\quad + \frac{\mu_w^{\gamma+1}}{K_x k_{rw, \frac{1}{2}}^{\gamma+1}} \\
&\quad - \frac{1}{\Delta x \Delta y} [\mu_{weff} S_w]_{h+\frac{1}{2}, i+\frac{1}{2}}^{\gamma+1} u_{wy, \frac{1}{2}}^{\gamma+1} + \frac{1}{\Delta x \Delta y} [\mu_{weff} S_w]_{h+\frac{1}{2}, i+\frac{1}{2}}^{\gamma+1} u_{wy, \frac{1}{2}}^{\gamma+1} \\
&\quad + \frac{1}{\Delta x \Delta y} [\mu_{weff} S_w]_{h+\frac{1}{2}, i-\frac{1}{2}}^{\gamma+1} u_{wy, \frac{1}{2}}^{\gamma+1} - \frac{1}{\Delta x \Delta y} [\mu_{weff} S_w]_{h+\frac{1}{2}, i-\frac{1}{2}}^{\gamma+1} u_{wy, \frac{1}{2}}^{\gamma+1}
\end{aligned} \tag{8.37}$$

$R_{Mu_{wx}}^{\gamma+1}$ is the residual for the water velocity in the x-direction

The discretization for Eq. 8.257 is as follows:

$$\begin{aligned}
R_{Mu_{wy}}^{\gamma+1} &= \frac{S_w^{\alpha^{\gamma+1}}}{\Delta y} P_{h,i+1}^{\gamma+1} - \frac{S_w^{\alpha^{\gamma+1}}}{\Delta y} P_{h,i}^{\gamma+1} \\
&\quad - \frac{2}{\Delta y^2} [\mu_{weff} S_w]_{h,i+1}^{\gamma+1} u_{wy_{h,i+\frac{3}{2}}}^{\gamma+1} - \frac{2}{\Delta y^2} [\mu_{weff} S_w]_{h,i}^{\gamma+1} u_{wy_{h,i-\frac{1}{2}}}^{\gamma+1} \\
&\quad - \frac{1}{\Delta x^2} [\mu_{weff} S_w]_{h+\frac{1}{2},i+\frac{1}{2}}^{\gamma+1} u_{wy_{h+1,i+\frac{1}{2}}}^{\gamma+1} - \frac{1}{\Delta x^2} [\mu_{weff} S_w]_{h-\frac{1}{2},i+\frac{1}{2}}^{\gamma+1} u_{wy_{h-1,i+\frac{1}{2}}}^{\gamma+1} \\
&\quad + \left[\begin{aligned} &\frac{2}{\Delta y^2} [\mu_{weff} S_w]_{h,i+1}^{\gamma+1} + \frac{2}{\Delta y^2} [\mu_{weff} S_w]_{h,i}^{\gamma+1} \\ &+ \frac{1}{\Delta x^2} [\mu_{weff} S_w]_{h+\frac{1}{2},i+\frac{1}{2}}^{\gamma+1} + \frac{1}{\Delta x^2} [\mu_{weff} S_w]_{h-\frac{1}{2},i+\frac{1}{2}}^{\gamma+1} \end{aligned} \right] u_{wy_{h,i+\frac{1}{2}}}^{\gamma+1} \\
&\quad + \frac{\mu_w^{\gamma+1}}{K_y k_{rw_{h,i+\frac{1}{2}}}} \\
&\quad - \frac{1}{\Delta x \Delta y} [\mu_{weff} S_w]_{h+\frac{1}{2},i+\frac{1}{2}}^{\gamma+1} u_{wx_{h+\frac{1}{2},i+1}}^{\gamma+1} + \frac{1}{\Delta x \Delta y} [\mu_{weff} S_w]_{h+\frac{1}{2},i+\frac{1}{2}}^{\gamma+1} u_{wx_{h+\frac{1}{2},i}}^{\gamma+1} \\
&\quad + \frac{1}{\Delta x \Delta y} [\mu_{weff} S_w]_{h-\frac{1}{2},i+\frac{1}{2}}^{\gamma+1} u_{wx_{h-\frac{1}{2},i+1}}^{\gamma+1} - \frac{1}{\Delta x \Delta y} [\mu_{weff} S_w]_{h-\frac{1}{2},i+\frac{1}{2}}^{\gamma+1} u_{wx_{h-\frac{1}{2},i+1}}^{\gamma+1} .
\end{aligned} \tag{8.38}$$

$R_{Mu_{wy}}^{\gamma+1}$ is the residual for the water velocity in the y-direction

8.4 Numerical Modelling of Two-Phase Flow Using the Darcy Model with Optimized Permeability Distribution (DMOPD) Approach

The Modified Brinkman's model for two phase flow is complicated to model and code because it requires the simultaneous solution of six different equations. Here, we introduce a Darcy Model with Optimized Permeability (DMOPD) approach for two-phase flow which is similar to the DMOPD approach for single phase flow wherein it divides the caves into an odd number of zones and then estimates an apparent permeability value in each zone such that using the optimized permeability values, the Darcy's model can accurately describe the true velocity profile of flow similar to that obtained from the Brinkman's model. The difference here from the DMOPD approach discussed in Chapter 7 is that the permeability distribution within the caves is obtained by assuming single phase flow through the reservoir. Once the permeability distribution has been obtained the two-phase Darcy's model (Eq. 8.15 & Eq. 8.16), can be used to predict flow within the reservoir. To estimate the permeability distribution within the zones, a parameter-estimation algorithm is used to obtain an acceptable match between the velocity distribution in the cave computed by the Darcy's model and that computed by the Brinkman's model. Thus, within the parameter estimation framework, the objective function minimized to obtain the set of permeability ratios that provide a velocity profile match of the Darcy's model with the Brinkman's model is given by Eq. 7.4.

The steps involved in the DMOPD approach are the following:

1. Initially the Brinkman's model for single phase fluid (water) is used to compute the pressure and velocity distribution in the aquifer.

2. Partition each cave in the aquifer into an odd number of zones.
3. Assign a maximum permeability value, k_{max} to the zone in the central zone of each cave.
4. Use an efficient optimization algorithm to compute the ratio of permeabilities in the other zone with respect to the permeability in the central zone. This ratio should decrease as we move toward the walls of the cave.
5. Compute the permeability value for each zone within the cave by multiplying the estimated permeability ratio for that zone by the permeability value (k_{max}) assigned to the central zone.
6. The two-phase Darcy's model with the optimized permeability distribution is then used to model velocity and pressure distribution within the reservoir.

8.5 Example Application, Results and Discussions

The example studied here consists of a simple linear flow in a two-dimensional reservoir model being flooded with water from the left side at a velocity of 3.18 m/day . The aquifer, of dimensions $1220m \times 41m \times 1.5m$, was discretized into $40 \times 41 \times 1$ grids (Fig. 58). The aquifer is closed at the top and bottom. In Fig. 31a, the region with 100% porosity (red portion in the middle) is the cave, and this section corresponds to Grids 14 – 28 . This region is surrounded by a porous media whose porosity is 25% (blue portions). The initial aquifer pressure was 27.58MPa .The numerical simulation was run for 50 days. Different correlations have been used to calculate the oil and water properties at each timesteps. They are as follows (Note: All these equations input and output values in field units)

$$b_0^{\gamma+1} = e^{c_o(P_o^{\gamma+1} - P_{sc})}. \quad (8.39)$$

Where, $c_o = 1.2 \times 10^{-5}$

$$b_w^{\gamma+1} = e^{c_w(P_o^{\gamma+1} - P_c^{\gamma+1} - P_{sc})}. \quad (8.40)$$

Where, $c_w = 5 \times 10^{-7}$

$$\mu_0^{\gamma+1} = 5e^{c_{\mu_o}(P_o^{\gamma+1} - P_{sc})}. \quad (8.41)$$

Where, $c_{\mu_o} = 2 \times 10^{-6}$

$$\mu_w^{\gamma+1} = e^{c_{\mu_w}(P_o^{\gamma+1} - P_c^{\gamma+1} - P_{sc})}. \quad (8.42)$$

Where, $c_{\mu_w} = 6 \times 10^{-8}$

Relative Permeabilities within porous media is given by:

$$k_{ro}^{\gamma+1} = 0.93 \times (1 - S_n)^{2.5}. \quad (8.43)$$

$$k_{rw}^{\gamma+1} = 0.5 \times (S_n)^{3.5}. \quad (8.44)$$

Where,

$$S_n = \frac{S_w^{\gamma+1} - S_{wc}}{1 - S_{or} - S_{wc}}. \quad (8.45)$$

Within the caves the Relative permeabilities are linear with respect to saturation

$$k_{ro}^{\gamma+1} = S_o^{\gamma+1} . \quad (8.43)$$

$$k_{rw}^{\gamma+1} = S_w^{\gamma+1} . \quad (8.44)$$

The caves have been divided into eight different zones, seven on either side of the central zone (Fig. 59). The initial water saturation in the reservoir is 35%. The irreducible water saturation is 20% and the residual oil saturation is 10%.

The DMOPD model was run on reservoir shown in Fig. 58 & 59. Differential Evolution algorithm was used to estimate the permeabilities by minimizing the objective function shown in Eq. 7.4. The upper and lower limits of permeability ratios to be optimized for each zone was fixed as 0.1 and 1 respectively. The optimization termination criteria was set as 3000 function evaluations. Figure 60 displays the minimization of the objective function. Table 12 lists the permeability ratios estimated at the end of the optimization cycle in the DMOPD model. The same case was run using the Darcy's model to compare the results obtained using the DMOPD model

Figure 61 shows the plot of water saturation obtained after 20 days and after 50 days using the DMOPD model. We can observe the parabolic shape obtained due to the free-flowing region. To further quantify the results the instantaneous water saturation was observed at two different locations within the aquifer (Fig 62). The first observation station (Observation Station 1) is located in Grid (10,21), which is 305m from the inlet. The second observation station (Observation Station 2) is located in Grid (20,21), which is 610m from the inlet. It can be observed from Fig 62 that breakthrough occurred quicker in

both the locations when DMOOD model has been used. This is due to the parabolic shape of the front.

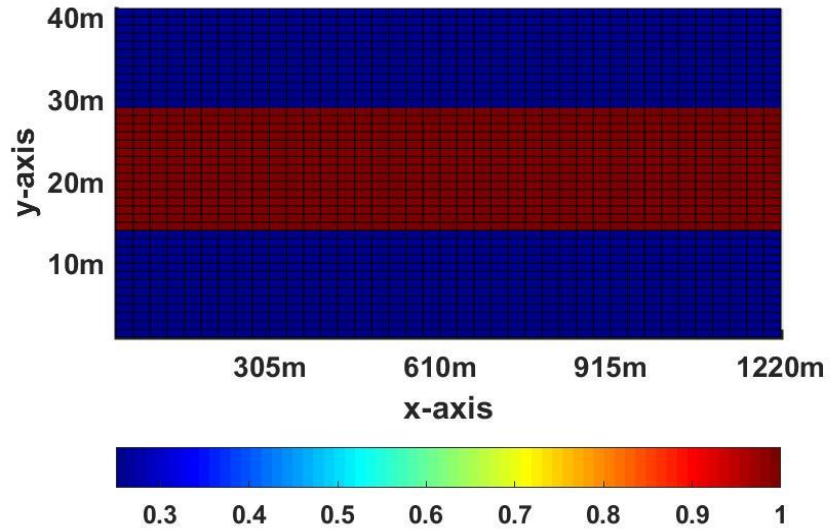


Figure 58: Reservoir Model Used

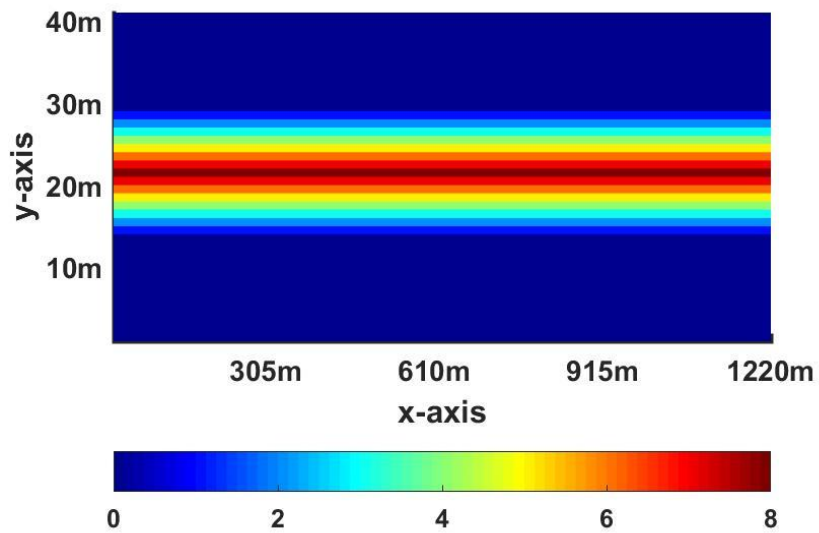


Figure 59: Division of Cave into 8 different zones

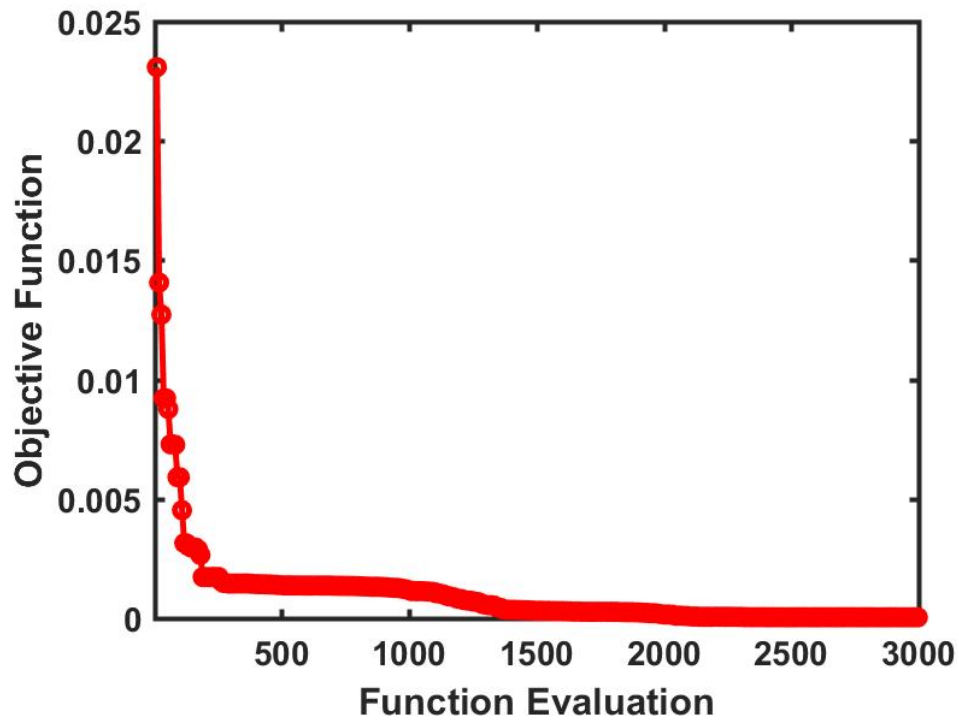


Figure 60: Graph showing the minimization of the objective function

Table 12: Optimized permeability ratios and the corresponding permeability values for the 8 zones

Zones	Permeability Ratio	Permeability Value
Zone 1	0.234	0.819×10^{12}
Zone 2	0.437	1.473×10^{12}
Zone 3	0.609	2.052×10^{12}
Zone 4	0.750	2.528×10^{12}
Zone 5	0.859	2.895×10^{12}
Zone 6	0.938	3.161×10^{12}
Zone 7	0.985	3.319×10^{12}
Zone 8 (Central Zone)	1	3.370×10^{12}

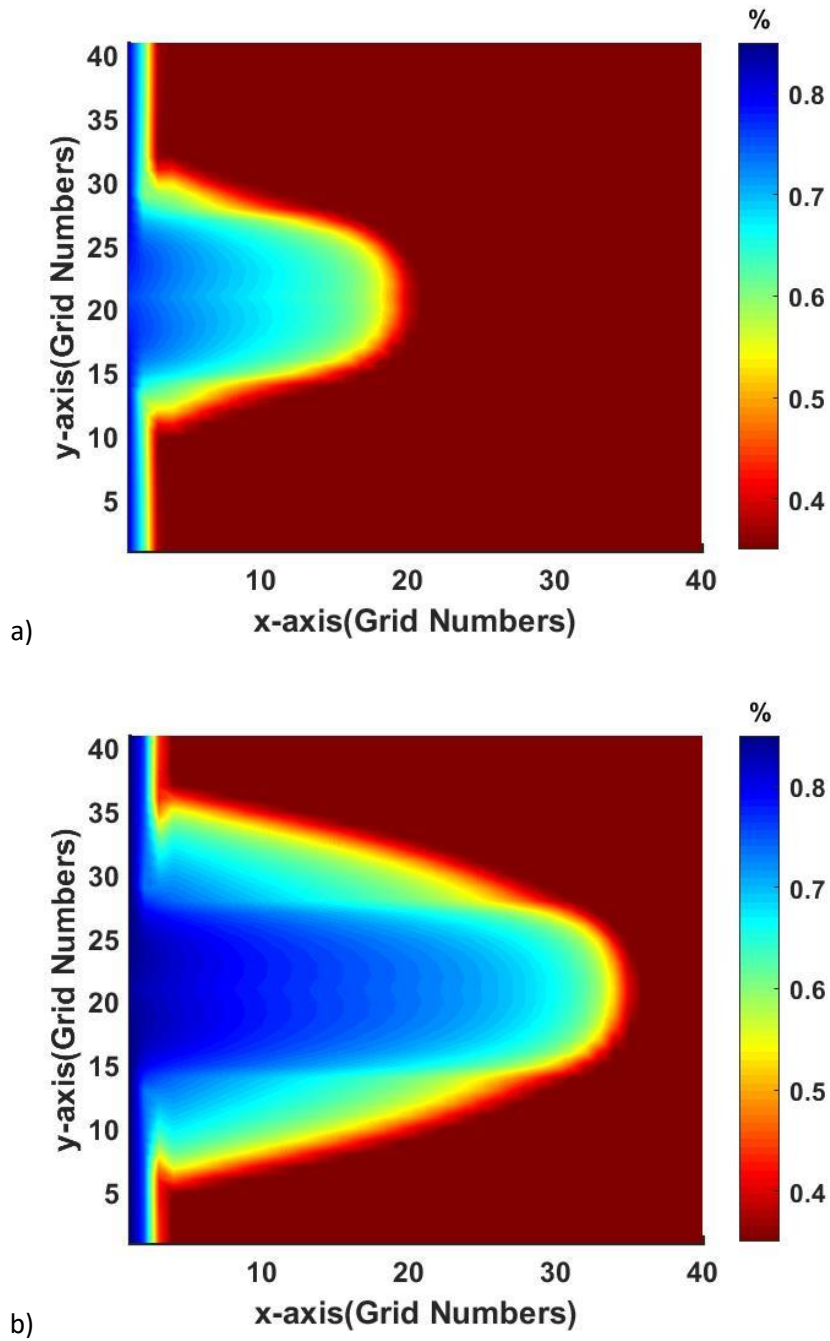
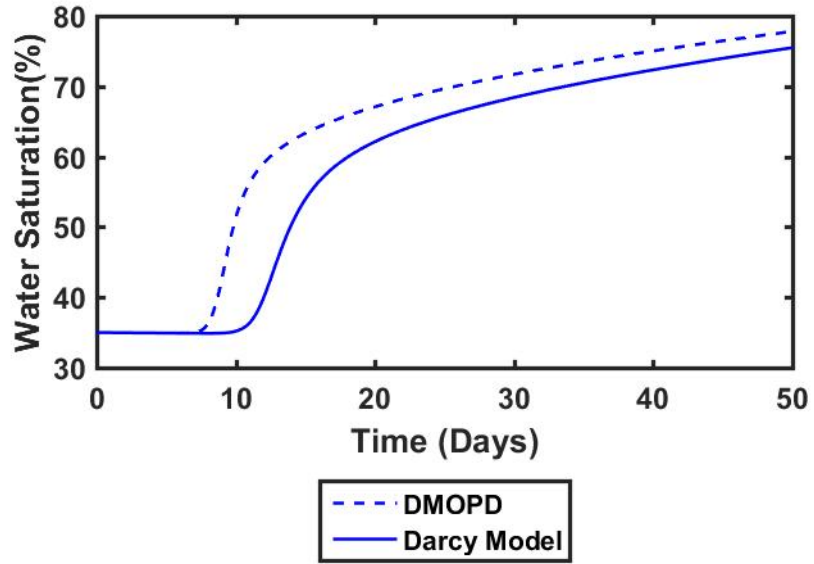
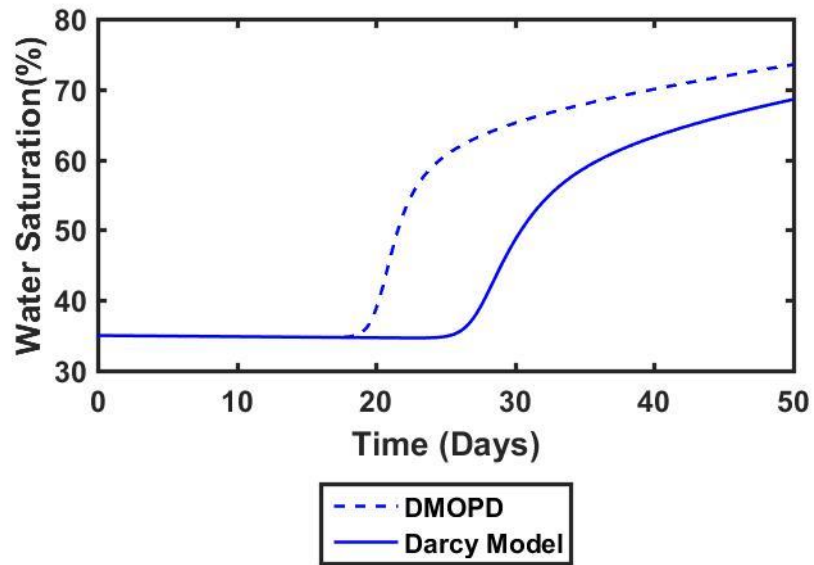


Figure 61: Figure Showing the Plot of Water Saturation after a) 20 days, and b) 50 days



a)



b)

Figure 62: Plot Showing the Water Saturation a) Observation Station 1, b) Observation Station 2

8.6 Conclusion

We have presented the mathematical formulation for the modified Brinkman's model to numerically model two-phase flow in karst reservoirs. A cell-centered finite volume discretization of the modified Brinkman's model has also been presented.

Due to the complexities associated with the development of codes for a two phase modified Brinkman's model we used the DMOPD model for two-phase flow. This approach divides the free flowing regions (caves) into different zones and optimizes the permeability ratios in those zones to mimic the velocity profile obtained using the Brinkman's model assuming single phase flow. The permeability ratio is the ratio of the permeability in that zone to the maximum permeability in the central zone. Once the permeabilities for each zones have been obtained a two-phase Darcy's model is used to simulate flow within the reservoir.

We presented one example to study this method. The example studied is a simple linear reservoir consisting of a cave surrounded by porous media on either side. The resulting water saturation plot showed a parabolic shape within the cave. When compared to the Darcy's model, the DMOPD model observed a faster breakthrough of water at the observation locations.

CHAPTER 9

CONCLUSIONS AND RECOMMENDATIONS

9.1 Conclusions

The primary outcomes of this research work are as follows

- Brinkman's equation was used to model flow in karst reservoirs using the cell-centered finite volume method and then the advection-diffusion-adsorption equations were used to model tracer transport. Comparisons were made to the Darcy's model and it was found that at high Peclet number, the results obtained from the two models are significantly different, with transport being faster in the Brinkman's model, while at low Peclet number, the difference between the two models are not significant.
- An unsteady flow Brinkman's model was obtained by adding the unsteady flow term present in the Navier-Stokes equation to the Brinkman's equation. The results obtained from the unsteady flow Brinkman's equation were compared to those obtained from the steady flow Brinkman's model. The examples showed that the steady and unsteady flow models yielded different tracer concentrations at observation wells located in the free-flow region but almost equal concentrations values at observation points located in the porous media. The velocity profile generated by the unsteady Brinkman's model does not produce a parabolic shape instantaneously, but gradually becomes more parabolic with time.

- A sector modeling approach was proposed to model fluid transport in karst aquifers. The method exploits the fast computation associated with the Darcy's model and the accuracy of modeling flow in the caves associated with the Brinkman's model. Thus, the method runs much faster than the Brinkman's model without compromising the accuracy of results obtained in the caves. Results clearly show that the sector modeling approach is computationally more efficient than the Brinkman's model and it also gives results that matches those from the Brinkman's model. For a model consisting of 40000 grids the Sector modelling approach was found to be 13 times faster than the Brinkman's model.
- A Darcy Model with Optimized Permeability Distribution (DMOPD) was proposed to model fluid transport in karst aquifers. Results obtained show that as the number of grids was increased the DMOPD modelling technique was more computationally effective in comparison to the Brinkman's model. For a model consisting of 40000 grids the DMOPD model was found to be 24 times faster than the Brinkman's model.
- The mathematical formulation for the modified Brinkman's model to numerically model two-phase flow in karst reservoirs was developed. A cell-centered finite volume discretization of the modified Brinkman's model has also been presented. The DMOPD modelling technique was used to model flow within the reservoir. The resulting water saturation plot showed a parabolic shape within the cave. When compared to the Darcy's model, the DMOPD model observed a faster breakthrough of water at the observation locations.

9.2 Recommendations

Based on the insights obtained from this research work, we propose the implementation of the following items to further improve upon the methods that have already been discussed in this dissertation:

- Modelling reactive transport within the karst caves by coupling advection-diffusion-adsorption-reaction equation along with the Brinkman's model
- Application of the Sector Modelling approach and the DMOPD approach to irregular shaped grids, while using different discretization techniques
- Study the existence of a correlation between the cave dimensions and the permeability ratios in the DMOPD model
- Codes can be developed for the modified Brinkman's model for two phase flow and the results can be compared with the DMOPD model to check the accuracy of the results obtained

REFERENCES

- Adler, P. M. (1979) 'Motion and Rupture of a Porous Sphere in a Linear Flow Field', *Journal of Rheology*, 23(1), p. 25. doi: 10.1122/1.549514.
- Albert, G., Virág, M. and Eróss, A. (2015) 'Karst porosity estimations from archive cave surveys - Studies in the Buda Thermal Karst System (Hungary)', *International Journal of Speleology*, 44(2), pp. 151–165. doi: 10.5038/1827-806X.44.2.5.
- Allaire, G. (1989) 'Homogenization of the stokes flow in a connected porous medium', *Asymptotic Analysis*. IOS Press, pp. 203–222. doi: 10.3233/ASY-1989-2302.
- Andreo, B., Carrasco, F., Duran, J. J. and LaMoreaux, J. W. (2010) *Advances in Research in Karst Media*. Leipzig: Springer-Verlag Berlin Heidelberg. doi: 10.1007/978-3-642-12486-0.
- Arbogast, T. and Brunson, D. S. (2007) 'A Computational Method for Approximating a Darcy-Stokes system Governing a Vuggy Porous Media', *Computational Geosciences*, 11(3), pp. 207–218.
- Arbogast, T. and Gomez, M. S. M. (2009) 'A discretization and multigrid solver for a Darcy-Stokes system of three dimensional vuggy porous media', *Computational Geosciences*, 13(3), pp. 331–348. doi: 10.1007/s10596-008-9121-y.
- Arbogast, T. and Lehr, H. L. (2006) 'Homogenization of a Darcy – Stokes system modeling vuggy porous media', *Media*, 78712, pp. 291–302. doi: 10.1007/s10596-006-9024-8.
- ASTM (1994) *1994 Annual Book of ASTM Standards: Emergency Standard Guide for Risk-Based Corrective Action Applied at Petroleum Release Sites (Designation: ES 38-94)*. West Conshohocken, PA: American Society for Testing and Materials.
- Auger, A. and Hansen, N. (2005) 'A Restart CMA Evolution Strategy With Increasing Population Size', in *2005 IEEE Congress on Evolutionary Computation*. IEEE, pp. 1769–1776. doi: 10.1109/CEC.2005.1554902.
- Awotunde, A. A. (2015) 'Estimation of well test parameters using global optimization techniques', *Journal of Petroleum Science and Engineering*. Elsevier, 125, pp. 269–277. doi: 10.1016/J.PETROL.2014.11.033.
- Awotunde, A. A. (2016) 'Generalized field-development optimization with well-control zonation', *Computational Geosciences*. Springer International Publishing, 20(1), pp. 213–230. doi: 10.1007/s10596-016-9559-2.

- Bai, M., Elsworth, D. and Roegiers, J.-C. (1993) ‘Multiporosity/multipermeability approach to the simulation of naturally fractured reservoirs’, *Water Resources Research*, pp. 1621–1633. doi: 10.1029/92wr02746.
- Beavers, G. S. and Joseph, D. D. (1967) ‘Boundary conditions at a naturally permeable wall’, *Journal of Fluid Mechanics*. Cambridge University Press, 30(1), p. 197. doi: 10.1017/S0022112067001375.
- Beavers, G. S., Sparrow, E. M. and Magnuson, R. A. (1970) ‘Experiments on Coupled Parallel Flows in a Channel and a Bounding Porous Medium’, *Journal of Basic Engineering*. American Society of Mechanical Engineers, 92(4), p. 843. doi: 10.1115/1.3425155.
- Belhaj, H., Agha, K., Butt, S. and Islam, M. (2003) ‘A Comprehensive Numerical Simulation Model for Non-Darcy Flow including Viscous Inertial and Convective Contributions. Paper SPE-85678-MS’, in *Nigeria Annual International Conference and Exhibition, 4-6 August*. Abuja, Nigeria: Society of Petroleum Engineers. doi: <http://dx.doi.org/10.2118/85678-MS>.
- Bellentani, G., Godi, A., Siliprandi, F., Terdich, P., Famy, C., Fournier, F., Jumeaucourt, C., Leandri, P. and Le Maux, T. (2016) ‘Rospo Mare Integrated Reservoir Study Italy, Adriatic Sea: An Innovative Approach of Karst System Modeling and History Match’, in: Society of Petroleum Engineers. doi: 10.2118/181636-MS.
- Bi, L., Qin, G. and Popov, P. (2009) ‘An Efficient Upscaling Process BMulti-Physics Model for Flow used on a Unified Fine-scale Simulation in Naturally Fracture Carbonate Karst Reservoirs.Paper SPE 125593’, in *SPE/EAGE Reservoir Characterization and Simulation Conference, 19-21 October*. Abu Dhabi: Society of Petroleum Engineers. doi: 10.2118/125593-MS.
- Bird, R., Stewart, W. and Lightfoot, E. (2002) *Transport phenomena*. Second. John Wiley & Sons.
- Bjørnstad, T., Haugen, O. B. and Hundere, I. A. (1994) ‘Dynamic behavior of radio-labelled water tracer candidates for chalk reservoirs’, *Journal of Petroleum Science and Engineering*. Elsevier, 10(3), pp. 223–238. doi: 10.1016/0920-4105(94)90083-3.
- Borghini, A., Renard, P. and Cornaton, F. (2016) ‘Can one identify karst conduit networks geometry and properties from hydraulic and tracer test data?’, *Advances in Water Resources*. Elsevier Ltd, 90, pp. 99–115. doi: 10.1016/j.advwatres.2016.02.009.
- Boyd, S. and Vandenberghe, L. (2004) *Convex Optimization*. Cambridge University Press. Available at: <https://dl.acm.org/citation.cfm?id=993483> (Accessed: 20 October 2017).

- Brinkman, H. C. (1949) 'A calculation of the viscous force exerted by a flowing fluid on a dense swarm of particles', *Applied Scientific Research*, 1(1), pp. 27–34. doi: 10.1007/BF02120313.
- Cabras, S., De Waele, J. and Sanna, L. (2008) 'Caves and Karst Aquifer Drainage of Supramonte (Sardinia, Italy): A Review.', *Acta Carsologica*, 37(2–3). doi: 10.3986/ac.v37i2.148.
- Castany, G. (1966) *Traite Partique des Equx Souterraines*. Edited by Dunod. Pariss.
- Chen, Z. (2007) *Reservoir Simulation: Mathematical Techniques in Oil Recovery*. Society for Industrial and Applied Mathematics. doi: 10.1137/1.9780898717075.
- CIPR, U. R. (2016) *Oil in ancient caves poses new challenges*. *ScienceDaily*, *ScienceDaily*. Available at: www.sciencedaily.com/releases/2016/01/160125090756.htm (Accessed: 28 March 2016).
- Corbel, J. (1959) 'Karsts du Yucatan et de la Floride', *Bulletin de l'Association de géographes français*. Persée - Portail des revues scientifiques en SHS, 36(282), pp. 2–14. doi: 10.3406/bagf.1959.7594.
- Covington, M. D., Wicks, C. M. and Saar, M. O. (2009) 'A dimensionless number describing the effects of recharge and geometry on discharge from simple karstic aquifers', *Water Resources Research*, 45(11). doi: 10.1029/2009WR008004.
- Dafny, E., Burg, A. and Gvirtzman, H. (2010) 'Effects of Karst and geological structure on groundwater flow: The case of Yarqon-Tananim Aquifer, Israel', *Journal of Hydrology*, 389(3–4), pp. 260–275. doi: 10.1016/j.jhydrol.2010.05.038.
- Darcy, H. (1856) *Les Fontaines Publiques de la Ville de Dijon*. Edited by V. Dalmont. Paris, France.
- Donald A. Nield, A. B. (2013) *Convection in Porous Media*. Edited by 4. New York: Springer-Verlag New York. doi: 10.1007/978-1-4614-5541-7.
- Durlofsky, L. and Brady, J. F. (1987) 'Analysis of the Brinkman equation as a model for flow in porous media', *Physics of Fluids*, 30(11), pp. 3329–3341. doi: 10.1063/1.866465.
- Ertekin, T., Abou-Kassem, J. H. and King, G. R. (2001) *Basic applied reservoir simulation*. Society of Petroleum Engineers. Available at: <http://store.spe.org/Basic-Applied-Reservoir-Simulation--P12.aspx> (Accessed: 13 September 2017).
- Flügel, E. (2004) *Microfacies of Carbonate Rocks - Analysis, Interpretation and Application*. Berlin: Springer Berlin Heidelberg.
- Ford, D. and Williams, P. (2007) *Karst Hydrogeology and Geomorphology*. West Sussex, England: John Wiley & Sons Ltd., doi: 10.1002/9781118684986.

Gauchet, R. and Corre, B. (1996) 'Rospo Mare Field : A Unique Experience of Heavy Oil Production with Horizontal Wells in a Karst Reservoir in Presence of a Strong Tilted Hydrodynamism', in. Society of Petroleum Engineers. doi: 10.2118/36869-MS.

Göppert, N. and Goldscheider, N. (2007) 'Solute and Colloid Transport in Karst Conduits under Low- and High-Flow Conditions', *Ground Water*, 46(1), pp. 61–68. doi: 10.1111/j.1745-6584.2007.00373.x.

Gulbransen, A., Hauge, V. and Lie, K. (2009) 'A multiscale mixed finite element method for vuggy and naturally fractured reservoirs', in *SPE Reservoir Simulation Symposium, 2-4 February*. The Woodlands, Texas, USA: Society of Petroleum Engineers. Available at: <https://www.onepetro.org/conference-paper/SPE-119104-MS>.

Happel, J. and Brenner, H. (1981) *Low Reynolds number hydrodynamics*. Dordrecht: Springer Netherlands (Mechanics of fluids and transport processes). doi: 10.1007/978-94-009-8352-6.

Hartmann, A., Goldscheider, N., Wagener, T., Lange, J. and Weiler, M. (2014) 'Karst water resources in a changing world: Review of hydrological modeling approaches', *Reviews of Geophysics*, 52(3), pp. 218–242. doi: 10.1002/2013RG000443.

Häuselmann, P., Otz, M. and Jeannin, P. Y. (2003) 'A review of the dye tracing experiments done in the Siebenhengste karst region (Bern, Switzerland)', *Eclogae Geologicae Helveticae*, 96, pp. 23–36. Available at: <http://boris.unibe.ch/86628/> (Accessed: 17 December 2016).

He, J., Killough, J. E., Fadlelmula, F., Mohamed, M. and Frain, M. (2015) 'A Unified Finite Difference Model for The Simulation of Transient Flow in Naturally Fractured Carbonate Karst Reservoirs', *SPE Reservoir Simulation Symposium*.

He, J., Killough, J. E., Fadlelmula F., M. M. and Frain, M. (2015) 'Unified Finite Difference Modeling of Transient Flow in Naturally Fractured Carbonate Karst Reservoirs - A 3D Case Study. Paper SPE-175098-MS', in *SPE Annual Technical Conference and Exhibition*. Houston, Texas: Society of Petroleum Engineers. doi: 10.2118/175098-MS.

Hornberger, G. M. (2014) *Elements of physical hydrology*. Johns Hopkins University Press.

Howells, I. D. (2006) 'Drag due to the motion of a Newtonian fluid through a sparse random array of small fixed rigid objects', *Journal of Fluid Mechanics*. Cambridge University Press, 64(3), p. 449. doi: 10.1017/S0022112074002503.

Hu, Y., Li, D., Shu, S. and Niu, X. (2016) 'Finite-volume method with lattice Boltzmann flux scheme for incompressible porous media flow at the representative-elementary-

volume scale.’, *Physical review. E*. American Physical Society, 93(2–1), p. 23308. doi: 10.1103/PhysRevE.93.023308.

Huang, Z. Q., Yao, J. and Wang, Y. Y. (2013) ‘An efficient numerical model for immiscible two-phase flow in fractured karst reservoirs’, *Communications in Computational Physics*, 13(2), pp. 540–558. doi: 10.4208/cicp.160711.240212a.

Ishii, M. and Hibiki, T. (2011) *Thermo-fluid dynamics of two-phase flow*. Springer.

Jackson, J. A. (1997) *Glossary of Geology*. Virginia, USA: American Geological Institute.

Jobson, H. E. and Harbaugh, A. W. (1999) *Modifications to the diffusion analogy surface-water flow model (DAFLOW) for coupling to the modular finite-difference ground-water flow model (MODFLOW)*, *Open-File Report 99-217*. U.S. Dept. of the Interior. Available at: <https://pubs.er.usgs.gov/publication/ofr99217> (Accessed: 25 May 2017).

Jones, I. P. (1973) ‘Low Reynolds number flow past a porous spherical shell’, *Mathematical Proceedings of the Cambridge Philosophical Society*, 73(1), pp. 231–238. doi: 10.1017/S0305004100047642.

Joodi, A., Sizaret, S., Binet, S., Bruand, A., Alberic, P. and Lepiller, M. (2010) ‘Development of a Darcy-Brinkman model to simulate water flow and tracer transport in a heterogeneous karstic aquifer (Val d’Orléans, France)’, *Hydrogeology Journal*, pp. 295–309. doi: 10.1007/s10040-009-0536-x.

K. Pruess, J.S.Y. Wang, Y. W. T. (1988) *Effective Continuum Approximation for Modeling Fluid and Heat Flow in Fractured Porous Tuff. Report SAND86-7000*. Albuquerque, New Mexico.

Kincaid, T. R., Hazlett, T. J. and Davies, G. J. (2002) ‘Quantitative groundwater tracing and effective numerical modeling in karst : an example from the Woodville Karst Plain of North Florida’, *Ground Water*, (850), pp. 1–8. doi: 10.1061/40796(177)13.

Koplik, J. (1983) ‘Viscosity renormalization in the Brinkman equation’, *Physics of Fluids*. AIP Publishing, 26(10), p. 2864. doi: 10.1063/1.864050.

Kossack, C. A. and Gurbinar, O. (2001) ‘A Methodology for Simulation of Vuggy and Fractured Reservoirs. SPE-66366-MS’, in *SPE Reservoir Simulation Symposium, 11-14 February*. Houston, Texas: Society of Petroleum Engineers. doi: 10.2118/66366-MS.

Krotkiewski, M., Ligaarden, I. S., Lie, K. A. and Schmid, D. W. (2011) ‘On the importance of the stokes-brinkman equations for computing effective permeability in karst reservoirs’, *Communications in Computational Physics*, 10(5), pp. 1315–1332. doi: 10.4208/cicp.290610.020211a.

LaBaugh, J. W. and Rosenberry, D. O. (2008) 'Introduction and Characteristics of Flow', in *Field Techniques for Estimating Water Fluxes Between Surface Water and Ground Water*. U.S. Geological Survey Techniques and Methods 4–D2. Available at: <https://pubs.usgs.gov/tm/04d02/> (Accessed: 25 May 2017).

Li, Y., Hou, J. and Ma, X. (2016) 'Data integration in characterizing a fracture-cavity reservoir, Tahe oilfield, Tarim basin, China', *Arabian Journal of Geosciences*, 9(8). doi: 10.1007/s12517-016-2562-z.

Liao, T. and Stützle, T. (2013) 'Bounding the population size of IPOP-CMA-ES on the noiseless BBOB testbed', in *Proceeding of the fifteenth annual conference companion on Genetic and evolutionary computation conference companion - GECCO '13 Companion*. New York, New York, USA: ACM Press, p. 1161. doi: 10.1145/2464576.2482694.

Licour, L. (2014) 'The geothermal reservoir of Hainaut: the result of thermal convection in a carbonate and sulfate aquifer', *Geologica Belgica*.

Ligaarden, I., Krotkiewski, M., Lie, K. A., Pal, M. and Schmid, D. (2010) 'On the Stokes-Brinkman Equations for Modeling Flow in Carbonate Reservoirs', in *ECMOR XII - Proceedings of the 12th European Conference on the Mathematics of Oil Recovery*. doi: 10.3997/2214-4609.20144924.

Loper, D. E. and Eltayeb, I. (2010) 'A linear model of conduit waves in karstic aquifers', *Geophysical & Astrophysical Fluid Dynamics*. Taylor & Francis Group, 104(4), pp. 309–322. doi: 10.1080/03091921003610152.

Lucia, F. J. (2007) *Carbonate Reservoir Characterization An Integrated Approach*.

Maloszewski, P., Herrmann, A. and Zuber, A. (1999) 'Interpretation of tracer tests performed in fractured rock of the Lange Bramke basin, Germany', *Hydrogeology Journal*, 2(7), pp. 209–218.

Maoshan, C. and Shifan, Z. (2011) 'Detecting Carbonate-karst Reservoirs Using the Directional Amplitude Gradient Difference Technique; Paper SEG-2011-1845', *2011 SEG Annual ...*, pp. 1845–1849. doi: 10.1190/1.3627564.

Milanovic, P. T. (2005) *Water Resources Engineering in Karst*, CRC Press. Florida. doi: 10.1017/CBO9781107415324.004.

Montaron, B. A., Xue, F. J., Tian, W. and Han, P. R. P. S. (2014) 'Cave Geomorphology and its Effects on Oil Recovery Factors in Tarim Karst Reservoirs, West China. Paper IPTC-17722-MS', in Conference, I. P. T. (ed.) *International Petroleum Technology Conference, 10-12 December*. Kuala Lumpur, Malaysia. doi: 10.2523/17722-MS.

Morales-Juberías, T., Olazar, M., Arandes, J. M., Zafra, P., Antigüedad, I. and Basauri, F. (1997) 'Application of a solute transport model under variable velocity conditions in a

conduit flow aquifer: Olalde karst system, Basque Country, Spain’, *Environmental Geology*. Springer-Verlag, 30(3–4), pp. 143–151. doi: 10.1007/s002540050141.

Navier, C. L. (1822) *Memoire Sur les lois du mouvement des fluides*. Edited by M. A. Sci. France.

Neale, G. and Nader, W. (1974) ‘Practical significance of brinkman’s extension of darcy’s law: Coupled parallel flows within a channel and a bounding porous medium’, *The Canadian Journal of Chemical Engineering*, 52(4), pp. 475–478. doi: 10.1002/cjce.5450520407.

Neuman, S. P. (1990) ‘Universal scaling of hydraulic conductivities and dispersivities in geologic media’, *Water Resources Research*, 26(8), pp. 1749–1758. doi: 10.1029/WR026i008p01749.

Nield, D. A. and Bejan, A. (2013) *Convection in Porous Media*. New York, NY: Springer New York. doi: 10.1007/978-1-4614-5541-7.

Odeh, A. S. (1964) ‘Unsteady-State Behavior of Naturally Fractured Reservoirs. SPE-966-PA’, *Society of Petroleum Engineers Journal*. Society of Petroleum Engineers, 5(1), pp. 60–66. doi: 10.2118/966-PA.

Oehlmann, S., Geyer, T., Licha, T. and Sauter, M. (2015) ‘Reducing the ambiguity of karst aquifer models by pattern matching of flow and transport on catchment scale’, *Hydrology and Earth System Sciences*, 19(2), pp. 893–912. doi: 10.5194/hess-19-893-2015.

Peng, X., Du, Z., Liang, B. and Qi, Z. (2009) ‘Darcy-Stokes Streamline Simulation for the Tahe-Fractured Reservoir With Cavities’, *SPE Journal*, 14(September), pp. 543–552. doi: 10.2118/107314-PA.

Popov, P., Efendiev, Y. and Qin, G. (2009) ‘Multiscale modeling and simulations of flows in naturally fractured Karst reservoirs’, *Communications in Computational Physics*, 6(1), pp. 162–184. doi: 10.4208/cicp.2009.v6.p162.

Popov, P., Qin, G., Bi, L. and Efendiev, Y. (2007) ‘Multiphysics and multiscale methods for modeling fluid flow through naturally fractured carbonate karst reservoirs’, in *SPE Middle East Oil & Gas Show and Conference, 11-14 March*. Kingdom of Bahrain: Society of Petroleum Engineers. Available at: <https://www.onepetro.org/journal-paper/SPE-105378-PA>.

Popov, P., Qin, G., Bi, L., Efendiev, Y., Ewing, R., Kang, Z. and Li, J. (2007) ‘Multiscale Methods for Modeling Fluid Flow Through Naturally Fractured Carbonate Karst Reservoirs’, in *SPE Annual Technical Conference and Exhibition, 11 - 14 November*. Anaheim, California, USA: Society of Petroleum Engineers.

Pruess, K. and Narasimhan, T. N. (1985) 'A Practical Method for Modeling Fluid and Heat Flow in Fractured Porous Media. SPE-10509-PA', *Society of Petroleum Engineers Journal*, 25(1), pp. 14–26. doi: 10.2118/10509-PA.

Reimann, T., Geyer, T., Shoemaker, W. B., Liedl, R. and Sauter, M. (2011) 'Effects of dynamically variable saturation and matrix-conduit coupling of flow in karst aquifers', *Water Resources Research*, 47(11). doi: 10.1029/2011WR010446.

Rivard, C. and Delay, F. (2004) 'Simulations of solute transport in fractured porous media using 2D percolation networks with uncorrelated hydraulic conductivity fields', *Hydrogeology Journal*. Springer-Verlag, 12(6), pp. 613–627. doi: 10.1007/s10040-004-0363-z.

Russel, W. and Sangtae, K. (1985) 'Modeling of Porous Media by Renormalization of the Stokes Equations', *Journal of Fluid Mechanics*, 154, pp. 269–286. doi: 10.1017/S0022112085001525.

Saffman, P. G. (1971) 'On the Boundary Condition at the Surface of a Porous Medium', *Studies in Applied Mathematics*, 50(2), pp. 93–101. doi: 10.1002/sapm197150293.

Schlumberger (2008) 'Characterization of Fractured Reservoirs'. Available at: www.slb.com/carbonates.

Singhal, B. B. S. and Gupta, R. P. (2010) *Applied Hydrogeology of Fractured Rocks*. Dordrecht: Springer Netherlands. doi: 10.1007/978-90-481-8799-7.

Smart, C. (1988) 'Artificial Tracer Techniques for the Determination of the Structure of Conduit Aquifers', *Ground Water*, 26(4), pp. 445–453. doi: 10.1111/j.1745-6584.1988.tb00411.x.

Srinivasan, S. and Nakshatrala, K. B. (2012) 'A stabilized mixed formulation for unsteady Brinkman equation based on the method of horizontal lines', *International Journal for Numerical Methods in Fluids*, 68(5), pp. 642–670. doi: 10.1002/flid.2544.

Staut, M. and Auersperger, P. (2006) 'Tracing of the Stream Flowing Through the Cave Ferranova Buža, Central Slovenia', *Acta Carsologica*, 35(2–3). doi: 10.3986/ac.v35i2-3.231.

Storn, R. and Price, K. (1997) 'Differential Evolution – A Simple and Efficient Heuristic for global Optimization over Continuous Spaces', *Journal of Global Optimization*. Kluwer Academic Publishers, 11(4), pp. 341–359. doi: 10.1023/A:1008202821328.

Trice, R. (2005) 'Challenges and Insights in Optimising Oil Production from Middle Eastern Karst Reservoirs. SPE-93679-MS', in *Proceedings of SPE Middle East Oil and Gas Show and Conference, 12-15 March*. Bahrain: Society of Petroleum Engineers. doi: 10.2118/93679-MS.

- Vassilev, D. and Yotov, I. (2009) ‘Coupling Stokes-Darcy Flow with Transport’, *SIAM Journal on Scientific Computing*, 31(5), pp. 3661–3684. doi: 10.1137/080732146.
- Warren, J. E. and Root, P. J. (1962) ‘The Behavior of Naturally Fractured Reservoirs. SPE-426-PA’, *Society of Petroleum Engineers Journal*. Society of Petroleum Engineers, 3(3), pp. 245–255. doi: 10.2118/426-PA.
- Weeks, S. W. and Sposito, G. (1998) ‘Mixing and stretching efficiency in steady and unsteady groundwater flows’, *Water Resources Research*, 34(12), pp. 3315–3322. doi: 10.1029/98WR02535.
- White, K. A., Aley, T. J., Cobb, M. K., Weikel, E. O. and Beeman, S. L. (2013) ‘Tracer Studies Conducted Nearly Two Decades Apart Elucidate Groundwater Movement Through A Karst Aquifer In The Frederick Valley Of Maryland’, pp. 101–112.
- White, W. B. (1977) ‘Role of Solution Kinetics in the Development of Karst Aquifers’, *Karst Hydrogeology*, 12, pp. 503–517.
- Wu, Y.-S. (1999) *On the Effective Continuum Method for Modeling Multiphase Flow, Multicomponent Transport and Heat Transfer in Fractured Rock*. LBNL-42720. Berkeley.
- Wu, Y.-S. and Pruess, K. (1988) ‘A Multiple-Porosity Method for Simulation of Naturally Fractured Petroleum Reservoirs. SPE-15129-PA’, *SPE Reservoir Engineering*, 3(1), pp. 327–336. doi: 10.2118/15129-PA.
- Wu, Y., Qin, G., Ewing, R. and Efendiev, Y. (2006) ‘A multiple-continuum approach for modeling multiphase flow in naturally fractured vuggy petroleum reservoirs’, in *International Oil & Gas Conference and Exhibition in China, 5-7 December*. Beijing, China: Society of Petroleum Engineers. doi: <http://dx.doi.org/10.2118/104173-MS>.
- Y.S. Wu, C. Finsterle, K. P. (1996) ‘Computer Models and their development for the unsaturated zone model at Yucca Mountain’, in G.S. Bodvarsson, M. B. (ed.) *Development and Calibration of the three dimensional site-scale unsaturated-zone model of Yucca Mountain, Nevada*. Berkeley, CA: Lawrence Berkely National Laboratory.
- Yao, J., Huang, Z., Li, Y., Wang, C., Lv, X. and Engineering, P. (2010) ‘Discrete Fracture Vug Network Model for Modeling Fluid Flow in Fractured Vuggy Porous Media; SPE 130287’, *SPE International Oil & Gas Conference and Exhibition*, (2005), pp. 1–14.
- Zemel, B. (1995) *Tracers in the Oil Field*. Amsterdam: Elsevier Science B.V.
- Zhang, C. and Bennett, G. D. (2002) *Applied Contaminant Transport Modeling*. 2nd edn. New York: John Wiley & Sons Inc.

Zhang, L., Bryant, S. L., Jennings, J. W., Arbogast, T. J. and Paruchuri, R. (2004) 'Multiscale Flow and Transport in Highly Heterogeneous Carbonates. Paper SPE-90336-MS', in *SPE Annual Technical Conference and Exhibition, 26-29 September*. Houston, Texas: Society of Petroleum Engineers. doi: <http://dx.doi.org/10.2118/90336-MS>.

Zhu, T., Waluga, C., Wohlmuth, B. and Manhart, M. (2014) 'A Study of the Time Constant in Unsteady Porous Media Flow Using Direct Numerical Simulation', *Transport in Porous Media*, 104(1), pp. 161–179. doi: 10.1007/s11242-014-0326-3.

Zimmerman, R. W. and Bodvarsson, G. S. (1994) *Hydraulic Conductivity of Rock Fractures*. Berkeley, CA. Available at: http://www.iaea.org/inis/collection/NCLCollectionStore/_Public/26/034/26034259.pdf.

Zou, C. (2013) 'Carbonate Fracture-Cavity Reservoir', in *Unconventional Petroleum Geology*. Elsevier, pp. 191–221.

VITAE

Name : Md Sarim Jamal

Nationality : Indian

Date of Birth : 1/5/1989

Email : sarim.jamal@gmail.com

Address : 56, A.N. Path, South P.P. Colony, Patna-13, Bihar, India

Educational Qualification : Ph.D. (Petroleum Engineering), April 2018
King Fahd University of Petroleum & Minerals (KFUPM)
Dhahran, Saudi Arabia

MSc (Petroleum Engineering), August 2012
Heriot-Watt University
Edinburgh, United Kingdom

B.Tech (Petrochemical Engineering), May 2010
Aligarh Muslim University (A.M.U.)
Aligarh, India

Publications:

- ‘Darcy’s Model with Optimized Permeability Distribution (DMOPD) for Efficient Simulation of Fluid Transport in Karst Aquifers’ (*Submitted to **Advances in Water Resources***)
- ‘Full-Field to Sector Modeling for Efficient Simulation of Fluid Flow in Karst Aquifers’, *Journal of Hydrology*, 564, pp. 682-696. DOI: <https://doi.org/10.1016/j.jhydrol.2018.07.028>.
- ‘A Finite Volume Discretization Approach to Solving Groundwater and Tracer Transport in Karst Aquifers’ (*Submitted to **Applied Water Sciences***)
- ‘Unsteady Brinkman’s Model for Flow in Karst Aquifers’ (*Submitted to **Journal of Hydroinformatics***)
- ‘The Importance of Stokes-Brinkman’s Equation in the Simulation of Fluid Flow

in Geothermal Karst Reservoirs' (*Submitted to Computational Geosciences*)

- 'Utilization of the Brinkman's Equation to Model Flow and Tracer Transport within Karst Reservoirs', Conference paper at 80th EAGE Annual Conference, 11-14 June 2018, Copenhagen, Denmark. DOI: 10.3997/2214-4609.201800839
- 'Modeling of Unsteady Flow in Karst Reservoirs using a modified Brinkman's equation', Conference paper at Innovations in Geosciences – Time for Breakthrough, 9 – 12 April 2018, St. Petersburg, Russia. DOI: 10.3997/2214-4609.201800120
- 'Optimal Parameter Selection in a Polymer Alternating Gas (PAG) Process', SPE-182794-MS, SPE Kingdom of Saudi Arabia Annual Technical Symposium and Exhibition, 25-28 April, Dammam, Saudi Arabia. DOI: <https://doi.org/10.2118/182794-MS>
- 'Multi-objective Well Placement Optimization Considering Energy Sustainability Along with Economical Gains', SPE-175842-MS, SPE North Africa Technical Conference and Exhibition, 14-16 September, Cairo, Egypt. DOI: <https://doi.org/10.2118/175842-MS>
- 'A Pareto-based Well Placement Optimization', 76th EAGE Conference & Exhibition, 16-19 June 2014, Amsterdam, Netherlands. DOI: 10.3997/2214-4609.20140947
- 'Effect of Project Life Time on Well Placement Optimization', 76th EAGE Conference & Exhibition, 16-19 June 2014, Amsterdam, Netherlands. DOI: 10.3997/2214-4609.20141519
- 'Effect of DFN upscaling on History Matching and Prediction of Naturally Fractured Reservoirs', SPE-164838-MS, EAGE Annual Conference and Exhibition incorporating SPE Europec, 10-13 June 2013, London, UK. DOI: <http://dx.doi.org/10.2118/164838-MS>